PUNCTURE RESISTANCE OF TURF REINFORCEMENT MATS

A Dissertation
Presented to
The Academic Faculty

by

Yue Xu

In Partial Fulfillment
of the Requirements for the Degree
Doctoral of Philosophy in the
School of Civil & Environmental Engineering

Georgia Institute of Technology
May 2021

PUNCTURE RESISTANCE OF TURF REINFORCEMENT MATS

Approved by:

Dr. J. David Frost, Advisor
School of Civil and Environmental Engineering
Georgia Institute of Technology

Dr. Mahdi Roozbahani
School of Computational Science and Engineering
Georgia Institute of Technology

Dr. Susan E. Burns, Co-advisor
School of Civil and Environmental Engineering
Georgia Institute of Technology

Dr. Glenn J. Rix
Principal
Geosyntec Consultants
Atlanta, Georgia

Dr. Arun M. Gokhale
School of Material Science and Engineering
Georgia Institute of Technology

Date Approved: Jan 18th, 2020

To my parents and my advisors

ACKNOWLEDGEMENTS

I would like to express my earnest gratitude to my dear advisors, Dr. J. David Frost and Dr. Susan E. Burns, who initiated my interest in this research topic and continuously provided me with their guidance and encouragement at all stages of my research work. Since I joined the Geosystems group in 2014, I worked with them as a Master's student. I have always been impressed by their insight, patience, and philosophy of life. I also would like to appreciate my thesis committee members, Dr. Arun Gokhale, Dr. Glenn Rix, and Dr. Mahdi Roozbahani, for their invaluable feedback on my research work.

I would like to offer my heartfelt gratitude to other faculties and staff in the School of Civil &Environmental Engineering, especially Dr. James A. Mulholland, Dr. Donald R. Webster, and Dr. Robert Simon for their support, which kept me on the pathway to the completion of my dream.

I sincerely convey my thanks to my undergraduate advisors from Hohai University for their advice and encouragement throughout the years even after I came to Georgia Tech.

I would like to thank everyone in Dr. Frost and Dr. Burns's group, all Geosystems professors, all students in Geo-group, and my dear friends for their blessings and help. I learned a lot from them and built up myself.

Finally, I offer the deepest gratitude to my dear parents and grandmother for their steadfast love, understanding, and constant encouragement throughout my life.

TABLE OF CONTENTS

LIST OF TABLES

LIST OF FIGURES

SUMMARY

Turf reinforcement mats (TRMs) are a subclass of Rolled Erosion Control Products (RECP) materials, which are designed for long-term performance. Many erosion control technologies are designed to be degradable; however, TRMs are non-degradable and designed to give long-term slope or channel protection before and during the establishment of vegetation. Ever since turf reinforcement mats (TRMs) have been used in erosion control, the question of installation damage is always a key issue that has not been fully explored in previous studies. Most manufacturers are interested in introducing the long service period of their TRM products and rarely mentioned their potential installation damages. As an essential part of the design, mechanical strength such as tensile strength is required to be evaluated and presented in product brochures. However, the strength of TRM products has not been fully exploited without properly considering their weaknesses.

The rapidly growing Rolled Erosion Control Products (RECP) market has led to the development of a wide variety of turf reinforcement mats (TRMs). TRM classification criteria from the Geosynthetic Institute (GSI) and the Erosion Control Technology Council (ECTC) are based on standard index properties, slope, and severity of erosion. Although there are general classification criteria developed by ECTC and GSI, some states provide lists of approved TRM products in the DOT manual using different classification criteria, while some states do not have clear classification criteria in their manual. Additionally, index properties of TRM products mainly come from the manufacturer or distributor, while there is limited data from third-party independent tests. Different turf reinforcement mats can vary significantly in basic laboratory properties and field performance. ASTM and ISO

standards provide instructions on impact and puncture resistance tests for turf reinforcement mat. These tests are necessary because they indicate the endurance of turf reinforcement mats under potential mechanical damage. Individuals determine TRM index properties based on standard testing methods, but there is not adequate study to evaluate the uniformity of current TRM products, which is revealed by statistical analysis of testing results.

The work performed in this thesis will focus on the analysis of puncture resistance as well as other physical and mechanical properties of turf reinforcement mats. Because turf reinforcement can vary significantly in basic geometry, index properties, laboratory, and field performance, this work seeks to identify relationships between the index properties of TRMs and their mechanical properties, which can help designers in product selection. The experimental results show that the static puncture resistance and extension of tested woven turf reinforcement mats increases as mass per unit area increases. The anisotropic stiffnesses of TRM products in the machine and cross-machine directions are observed in the experiments.

This study also investigates the puncture resistance of soil-TRM systems by performing California Bearing Ratio based puncture tests. Experimental results show that turf reinforcement mats can remarkably improve the penetration value of soil-turf reinforcement mat system by up to almost 60% compared to the soil only system. It is also observed that soil benefits more in penetration tests with higher puncture resistance and mass per unit area of the turf reinforcement mat.

The numerical simulation of the puncture test of turf reinforcement mats illustrates their damage characteristics with the change of projectile shape, material density, and material geometry. The results indicate that turf reinforcement with greater density has a higher puncture resistance and reflects a similar trend seen in experimental tests. Further, the modeling results show that a turf reinforcement mat impacted by a projectile with a flat tip presents the greatest puncture resistance compared with those punctured by the projectiles of conical and hemispherical tips. The simulation of the soil-turf reinforcement mat system shows higher soil reinforcement at shallow soil depths.

In engineering practice, turf reinforcement mats are usually applied for soil erosion control together with vegetation reinforcement. A series of experiments were also performed to explore the reinforcement of the plant roots-turf reinforcement mat system, especially for young plants. In this study, Dandelion and Ryegrass were selected as representative of vegetation with taproots and fibrous roots. The experimental results suggest that the pullout resistance of fibrous roots is greater than that of taproots. Although the application of turf reinforcement mats does not have a clear effect on the pullout resistance of plant roots, it improves their initial pullout modulus. In addition, turf reinforcement mat coverage over soil can reduce water evaporation up to 78% thereby retaining soil moisture during seed germination.

This study also investigates the uniformity of TRMs in the market by comparing the standard deviation of measured index properties collected from the NTPEP database. In classifying TRM products, multiple properties should be considered rather than only focusing on vegetated shear stress. Besides, mechanical properties such as puncture resistance and tensile strength should be tested for quality control of TRMs.

CHAPTER 1. INTRODUCTION

1.1 Background

Geosynthetic products are classified into various categories based on their application and type of function. Turf reinforcement mats (TRMs) are a subclass of RECP (Rolled Erosion Control Product) materials, which are long-term erosion control products. Different from other temporary degradable RECPs, TRMs are non-degradable for providing immediate slope or channel protection before and during the establishment of vegetation (ECTC, 2001).

Damage to TRMs is a major concern since they were introduced for civil engineering applications. The types of damage include abrasion, splitting, puncturing, rupture, yarn cutting, and tearing (Watn & Chew, 2002). During the service life of a TRM, installation may represent the greatest opportunity for mechanical impact on it. The characterization of mechanical properties is an important aspect of evaluating TRMs. ECTC provides classification criteria based on multiple index property testing methods defined by ASTM and ISO standards. A static puncture test is a standard test that evaluates a TRMs' capability to withstand severe loads during installation. However, ECTC chooses tensile strength as a criterion in classifying types of TRMs rather than static puncture strength. Other alternative puncture test methods, such as pin puncture and dynamic perforation tests, are also considered suitable to determine the endurance and mechanical property of TRMs. Previous experimental studies indicated inconsistency between these test methods and tried to evaluate the correlation between measured resistance values from different test approaches regardless of manufacturing method or material type. Although a considerable

number of studies have focused on the resistance of reinforcing geosynthetics (e.g., geotextiles and geogrids) to damage during construction, there are minimal studies on the resistance of TRM.

1.2 Research objectives

The thesis is focused on the analysis of puncture resistance and other basic physical properties of turf reinforcement mats, which have been used as erosion control material since the 1970s and have seen a great increase in use within recent decades. Turf reinforcement can vary significantly in basic geometry, index properties, laboratory, and field performance. One objective is to find out how the index properties of TRMs correlate with their mechanical properties, which can help potential users selecting products by knowing the basic index properties of TRMs.

A challenge for this study is that there is limited background research on turf reinforcement mats. The classification of TRM products is different in each state, and some states even do not have clear classification criteria. In addition, physical properties data of TRM products frequently come from manufacturers or distributors while there are few data from a third party field and lab tests. No study identified directly relates erosion control performance explicitly to the physical properties of TRMs. Potential users of TRM thus need a procedure on which they can rely when selecting appropriate products. This thesis seeks to provide some suggestions on general classification criteria and minimum property values of eligible TRM products by reviewing the recent development of TRM products and the different scenarios for TRM applications.

The puncture behavior of woven and nonwoven geotextiles has been studied in previous research primarily by experimental methods such as performing static puncture tests. However, there is limited information on the behavior of these geotextiles when subjected to perpendicular concentrated forces. An objective of this study is to explore the mechanism in puncture deformation of TRMs and soils. The results obtained by the numerical simulation of the puncture process are also compared with the experimental results of CBR based tests.

Considering the function of TRMs in soil reinforcement, the role of grass roots in this vegetation-TRM reinforced soil system cannot be ignored. Besides exploring the puncture loading that is applied downwards on soils, this study also explores the effect of TRMs in protecting young vegetation from pullout by upward forces.

1.3 Thesis Organization

This manuscript is organized into seven chapters. Chapter 1 presents the introduction, problem statement, objectives, and scope of the research study. Chapter 2 synthesizes a literature review and background information on erosion control and the development of turf reinforcement mat. Chapter 3 explains the laboratory physical testing method and results on seven turf reinforcement mats from four different manufacturers. Chapter 4 presents how vegetation interacts with turf reinforcement mats by performing pullout tests with three TRM materials. Chapter 5 presents modified CBR tests on soil and soil-TRM systems. Chapter 6 simulates the puncture process on TRM only as well as the soil-TRM system considering multiple factors. Chapter 7 summarizes salient conclusions from this study and provides recommendations for future work.

CHAPTER 2. LITERATURE REVIEW

As a woven product, TRMs are studied at both macro and micro levels. At a macro level, TRMs are considered as a homogeneous material so the related properties involve conductivity and strength. At a micro level, TRMs are considered as a heterogeneous material so the related properties include fiber tension and matrix stress distribution. Micro-scale geometry is defined through a unit cell. When applied at a macro level, the topology of unit cells is defined by the weaving pattern.

2.1 Turf Reinforcement Mats as an Erosion Control Material

2.1.1 General Definition of Turf Reinforcement Mat

The Erosion Control Technology Council (ECTC) defines a turf reinforcement mat (TRM) as a permanent three-dimensional rolled erosion control product (RECP) to establish permanent reinforcing vegetation in hydraulic infrastructures. The primary difference between TRMs and other RECP materials is that TRMs provide long-term erosion protection during high expected overland flow conditions. Because TRMs also provide interlocking with the soil, they increase resistance to the high shear stress exerted by the water flow. Low cost and allowable infiltration of surface water are the chief advantages of TRMs.

2.1.2 TRM Properties Testing Criteria

TRMs' property testing is separated into laboratory index testing and field performance testing. The Geosynthetic Institute (GSI) specified eight index test properties,

which include mass per unit area, thickness, stiffness, specific gravity, resiliency, tensile strength and elongation, light penetration, and UV resistance. Specific gravity and resiliency are not available in the manufacturer's brochures, but they often provide unvegetated/vegetated shear stress (ASTM D6460) and seedling emergence (ASTM D7322). ASTM standard testing on TRMs, designed to measure material integrity, sufficiency, continuity, and quality under standardized conditions, are summarized in Table 2.1.

Table 2.1. List of ASTM Standard Testing for TRMs

	Index property testing
D 4354	Practice for Sampling of Geosynthetics for Testing
D 4355	Standard Test Method for Deterioration of Geotextiles by Exposure to Light, Moisture and Heat in a Xenon Arc-Type Apparatus
D 5199	Test Method for Measuring the Nominal Thickness of Geosynthetics
D 6241	Standard Test Method for Static Puncture Strength of Geotextiles and Geotextile-Related Products Using a 50-mm Probe
D 6454	Standard Test Method for Determining the Short-Term Compression Behavior of Turf Reinforcement Mats (TRMs)
D 6475	Test Method for Measuring Mass per Unit Area of Erosion Control Blankets
D 6524	Standard Test Method for Measuring the Resiliency of Turf Reinforcement Mats (TRMs)
D 6525	Standard Test Method for Measuring Nominal Thickness of Permanent Rolled Erosion Control Products
D 6566	Standard Test Method for Measuring Mass per Unit Area of Turf Reinforcement Mats

D 6567	Standard Test Method for Measuring the Light Penetration of a Rolled Erosion Control Product (RECP)
D 6575	Standard Test Method for Determining Stiffness of Geosynthetics Used as Turf Reinforcement Mats (TRMs)
D 6818	Standard Test Method for Ultimate Tensile Properties of Rolled Erosion Control Products
D 7238	Standard Test Method for Effect of Exposure of Unreinforced Polyolefin Geomembrane Using Fluorescent UV Condensation Apparatus
D 7748	Standard Test Method for Flexural Rigidity of Geogrids, Geotextiles, and Related Products

Performance testing	
D 4594	Standard Test Method for Effects of Temperature on Stability of Geotextiles
D 6459	Standard Test Method for Determination of Rolled Erosion Control Product (RECP) Performance in Protecting Hillslopes from Rainfall-Induced Erosion
D 6460	Standard Test Method for Determination of Rolled Erosion Control Product (RECP) Performance in Protecting Earthen Channels from Stormwater-Induced Erosion
D 7101	Standard Index Test Method for Determination of Unvegetated Rolled Erosion Control Product (RECP) Ability to Protect Soil from Rain Splash and Associated Runoff Under Bench-Scale Conditions
D 7322	Standard Test Method for Determination of Rolled Erosion Control Product (RECP) Ability to Encourage Seed Germination and Plant Growth under Bench-Scale Conditions
D 8151	Standard Practice for Obtaining Rainfall Runoff from Unvegetated Rolled and Hydraulic Erosion Control Products (RECPs and HECPs) for Acute Ecotoxicity Testing

2.1.3 Categorization of TRMs

The ECTC divides TRMs into two categories: TRM and high-performance TRM (HPTRM), where HPTRM differs from TRM because of higher resistance to shear stress in the vegetated condition, higher tensile strength, and higher UV stability when compared to TRMs (Table 2.2 and Table 2.3). General index value such as material mass per unit area higher than 8.0 oz/yd^2 (271g/m^2), and thickness higher than 0.25 in (6.35mm) for all types of turf reinforcement mats are required. For type 5A to 5E, the TRM products may be supplemented with degradable components such as mulches in the material composition.

Table 2.2. ECTC Classification of TRMs (modified from ECTC specification)

Type	Application and standard specification
5.A	A TRM designed for use on geotechnically stable slopes up to 1:1 (H: V) provides unvegetated shear stress of at least 2.0 lbs/ft^2 (96Pa), and vegetated shear stress of at least 6.0 lbs/ft^2 (287Pa). The tensile strength value at the time of manufacture is at least 150 ×150 lbs/ft (2.2×2.2 kN/m). Minimum UV stability is 80% at 500 hrs.
5.B	A TRM designed for use on geotechnically stable slopes up to 1:1 (H: V) provides unvegetated shear stress of at least 2.0 lbs/ft^2 (96Pa), and vegetated shear stress of at least 8.0 lbs/ft^2 (383Pa). The tensile strength value at the time of manufacture is at least 175 ×175 lbs/ft (2.6×2.6 kN/m). Minimum UV stability is 80% at 500 hrs.
5.C	A TRM designed for use on geotechnically stable slopes up to 0.5:1 (H: V) provides unvegetated shear stress of at least 2.0 lbs/ft^2 (96Pa), and vegetated shear stress of at least 10.0 lbs/ft^2 (479Pa). The tensile strength value at the

time of manufacture is at least 200 ×200 lbs/ft (2.9×2.9 kN/m). Minimum UV stability is 80% at 1000 hrs.

5.D A TRM designed for use on geotechnically stable slopes up to 0.5:1 (H: V) provides unvegetated shear stress of at least 2.0 lbs/ft^2 (96Pa), and vegetated shear stress of at least 12.0 lbs/ft^2 (575Pa). The tensile strength value at the time of manufacture is at least 325 ×225 lbs/ft (4.8×3.3 kN/m). Minimum UV stability is 80% at 1000 hrs.

5.E A TRM designed for use on geotechnically stable slopes up to 0.5:1 (H: V) provides unvegetated shear stress of at least 2.0 lbs/ft^2 (96Pa), and vegetated shear stress of at least 12.0 lbs/ft^2 (575Pa). The tensile strength value at the time of manufacture is at least 1500 ×1500 lbs/ft (21.9×21.9 kN/m). Minimum UV stability is 90% at 1000 hrs.

5.F A high-performance TRM designed for use on slopes up to 0.5:1 (H: V) provides unvegetated shear stress of at least 2.0 lbs/ft^2 (96Pa), and vegetated shear stress of at least 14.0 lbs/ft^2 (670Pa). The tensile strength value at the time of manufacture is at least 3000 ×3000 lbs/ft (43.8×43.8 kN/m). Minimum UV stability is 80% at 3000 hrs.

Table 2.3. GSI Specified Values for TRMs (modified from GSI Specification)

Properties	Class "1/A" Most severe	Class "2/B" Medium severe	Class "3/C" Least severe
Mass per unit area (D6566)	12 oz/yd^2 (400 g/m^2)	10 oz/yd^2 (340 g/m^2)	8 oz/yd^2 (270 g/m^2)
Thickness (D6525)	3.3 mm	3.3 mm	3.3 mm
Stiffness (D7748)	300 g-cm	300 g-cm	300 g-cm
Specific gravity (D792)	0.9 g/cc	0.9 g/cc	0.9 g/cc
Resiliency (D6524)	70%	70%	70%
Tensile strength (D6818)	150 lb/ft (2.2kN/m)	125 lb/ft (1.8kN/m)	100 lb/ft (1.5kN/m)
Tensile elongation (D6818)	10%	10%	10%
Light penetration (D6567)	60%	60%	60%
UV resistance (D7238)	80% @3000hrs	80% @3000hrs	80% @3000hrs

Both GSI and ECTC classify TRMs based on the application and severity of erosion. Compared with the ECTC classification method, the minimum tensile strength of TRMs required in GSI is lower than that required in ECTC (Table 2.4). ECTC provides a more detailed specification requiring minimum tensile strength, vegetated shear stress, and UV stability for five types of TRMs. For engineering safety consideration, this work will follow ECTC's standard specification because it requires higher tensile strength and vegetated shear stress. GSI has a more strict requirement on UV resistance to ensure the long-term stability of TRM materials. However, each state provides a list of approved TRM products based on different physical properties specifications, which can make it difficult to determine if a TRM product meets the product qualifications. Note that classes 1~3 are for slope erosion control TRMs and classes A~C are for ditch and channel erosion control TRMs.

Table 2.4. GSI Specification Requirements.

Classes	Description
1	1:1 (H: V) slope
2	1:1 to 3:1 (H: V) slope
3	3:1 (H: V) slope
A	Max Allowable shear stress >10 lb/ft^2(>480 Pa)
B	Max Allowable shear stress =6~10 lb/ft^2(290~480 Pa)
C	Max Allowable shear stress<6 lb/ft^2(<290 Pa)

In each state, the Department of Transportation (DOT) will provide the classification of TRMs using required parameters such as allowable shear stress and thickness (Table 2.5), but they are variable from state to state. For example, Nebraska DOT requires the minimum thickness of TRM as 0.25~0.5 inches and minimum light penetration

of 20%. Louisiana DOT requires physical properties such as maximum light penetration of 45% without requiring allowable shear stress. Alabama DOT classifies TRM using almost the same specification as ECTC standard but without requiring tensile strength and UV resistance. In order to achieve optimum field performance, it is necessary to provide a consistent list of specified index properties of TRM products under the guidance of the ECTC standard.

Table 2.5. Classification of TRMs by Allowable Shear Stress.

Type	Allowable shear stress (Modified from GDOT report by Burns, 2011)	Allowable shear stress (Modified from MoDOT report by Cox, 2016)	Allowable shear stress (Modified from NDOT, 2018)
1	0~2 psf	3.5~6 psf	6.0 psf
2	0~4 psf	6.1~8 psf	8.0 psf
3	0~6 psf	8.1~10 psf	10.0 psf
4	0~8 psf	10.1 psf or greater	-
5	0~10 psf	-	-
6	0~12 psf	-	-

2.1.4 Selecting TRMs

The selection of proper TRMs for erosion control needs to consider design conditions, such as slope erosion protection and channel scour resistance. The selection of materials needs to comply with erosion and sediment control regulations, in order to limit the transport of solids to receiving streams. The Revised Universal Soil Loss Equation (McCool, 2017) estimates soil loss from a slope considering runoff, slope erosion, slope steepness, and cover factors, and FHWA's Hydraulic Engineering Circular (2016) instructs

how to calculate the maximum permissible shear stress of a channel considering water flow velocity, Manning's coefficient, channel liner safety factor, and soil safety factor. Among the considered factors, both the cover factor (Equation 1) and the channel liner factor (normally between 1.0 and 1.5 determined by Reynolds Number, calculated using Equation 2) are related to erosion control materials. For any geosynthetic materials, characterization is based on physical, chemical, mechanical, hydraulic, endurance, and degradation properties (Table 2.6).

$$C_{f,TRM} = 1 - \left(\frac{\tau_{p,VEG-test}}{\tau_{p,TRM-test}}\right)(1 - C_{f,VEG}) \quad (1)$$

where

$\tau_{p,VEG-test}$ = permissible shear stress on the vegetative lining, N/m^2 (lb/ft^2) as reported by manufacturer's testing;

$\tau_{p,TRM-test}$= permissible shear stress on the turf-reinforced vegetative lining, N/m^2 (lb/ft^2) as reported by manufacturer's testing;

$C_{f,VEG}$= grass cover factor (empirical values determined by cover density and grass growth form);

$C_{f,TRM}$ = TRM cover factor.

Reynolds number is calculated as below:

$$R_e = \frac{V_s D_{50}}{\nu} = \frac{\sqrt{gdS}D_{50}}{\nu} \quad (2)$$

where

R_e = Reynolds number;

V_s = shear velocity (ft/s);

ν = kinematic viscosity, 1.217×10^{-5} ft^2/s at 60℉;

g = gravitational acceleration, 32.2 ft/s^2;

S = channel slope (ft/ft).

Table 2.6 – Characterization Properties for Evaluating Geosynthetics

Properties	Parameters
Physical	Thickness, specific gravity, mass per unit area, porosity, apparent opening size.
Chemical	Polymer type, filler material, carbon black percentage, plasticizer and additive details, the manufacturing process for fiber, and geosynthetics.
Mechanical	Tensile strength, compressibility, elongation, tear/impact/ puncture resistance, burst strength, seam strength, fatigue resistance, interface friction with soil, anchorage in soil.
Hydraulic	Permittivity (cross-plane permeability), transmissivity (in-plane permeability), clogging potential.
Endurance	Installation damage potential - tear/impact/puncture resistance, abrasion resistance, and creep.
Degradation	Resistance to ultra-violet radiation, temperature, oxidation, aging, chemical, and biological reactions

2.1.5 Utilization and Ecological Evaluation

From an ecosystem health standpoint, there is some controversy regarding the use of RECPs in erosion control on steep slopes and channels. One of the problems discovered from Carolina bay wetlands and horticultural settings in Wisconsin indicates that an RECP is a potential hazard to snakes and other wildlife because they can trap wildlife in the plastic mesh (Barton, 2005, Kapfer and Paloski, 2011). However, this concern has less influence

on the use of TRMs because their mesh size is small enough to avoid entangling large climbing species such as snakes.

The aging effect is another consideration when RECPs are applied in channel/slope erosion control. A study of the aging effects of RECPs indicated that polypropylene materials had less strength loss compared with natural materials (Khanna, 2005) after three years of usage. Factors that cause aging of a geosynthetic include the inherent structure of high molecular weight composites, degradation due to ultra-violet radiation, degradation due to temperature, and degradation due to water. Ultra-violet radiation can lead to the decomposition of the polymer and then decrease the strength and elongation of the material. TRMs are mostly made of polypropylene with a sacrificial additive to ensure long-term strength and performance. The additive in polypropylene is 0.2%~2% black carbon, which reacts with ultraviolet rays and ensures material with more than 10 years of UV resistance. For some light-color TRMs, 10% of zinc oxide can be added to increase performance, which yields more than 8 years of UV resistance.

2.2 A Bioengineering Approach for Slope Stabilization and Erosion Control

To limit the transport of soil solids, more attention has been given in recent decades to slope protection, especially during the construction of highways, bridges, and other human activities. The main approaches to prevent slope erosion are divide into conventional and bioengineering techniques. The conventional techniques for slope stabilization include grouting, masonry stone, retaining wall, and anti-sliding piles (Wang et al., 2015). Bioengineering techniques consist of techniques such as combining the establishment of vegetation with branching layering, fascines live crib walls, with synthetic

products like geogrids, and geonets (Morgan and Rickson, 2003). Table 2.7 compares the advantage and disadvantages of conventional and bioengineering methods in slope erosion control.

Table 2.7. Comparison of Conventional and Bioengineering Approaches in Slope Stabilization and Erosion Control (After Capilleri et al., 2016; Evette et al., 2009; Gray&Sotir, 1996)

	Pros	Cons
Conventional approach	Effective in early slope stabilization.	Poor sustainability; High maintenance cost.
Bioengineering approach	1. Working as anchorage (deep roots) and reinforcement (shallow roots); 2. Reduction of soil pore water pressure by transpiration; 3. Air cleaning and aesthetic effects; 4. Low maintenance cost in long term.	1.Not effective in early vegetation establishment; 2. Limited root depth in shallow soil surface; 3. Resulting in cracks of soil by growing root.

2.2.1 Role of TRMs in Erosion Control

There is very limited research on TRMs in erosion control and their performance is not well studied. Previous studies about alternative material for the establishment of vegetation for soil erosion control have focused primarily on mulches and geotextiles. The role of mulches and geotextiles in controlling soil erosion comes through reducing rainfall impact and runoff velocity (Niziolomski, 2014; Fletcher, 2012; Rickson, 1990), and improving soil structure and porosity through promoting biological activity in the soil (Kader et al., 2017).

Rickson studied soil loss at different rainfall intensities and geotextile material coverage. One of his experimental results indicated that the surface geotextile had better

performance in controlling soil loss than the buried geotextile. This is because the buried geotextile sieves the topsoil and separates soil aggregation leaving loose unpacked soil above the geotextile, which is vulnerable to rainfall impact (Rickson 1988).

The inclusion of tensile strength of erosion control products as an indicator of performance can be misleading, due to the impact of tensile strength on the erosion process (Morgan and Rickson, 2003). While it is not indicative of erosion control potential, tensile strength is useful to estimate the possibility of damage to these geosynthetics during installation and lifetime usage. Consequently, it is necessary to test these strength properties (tensile strength, static puncture strength, and dynamic strength).

There is research that indicates that the effects of geotextiles on surficial microclimate are considerable. Geotextiles separate soil from the change of air temperature (Reynolds, 1976) and protect soil from moisture evaporation loss (Morgan and Rickson, 2003; Dudeck et al, 1970). TRMs with dark colors can absorb heat thus increase soil temperature. Thicker geotextiles are more effective in maintaining soil moisture. Light penetration on covered soil is affected by geotextile pore size and color of geotextile. In some cases, light penetration may influence seedling germination and make vegetation turn pale (Morgan and Rickson, 2003).

2.2.2 Role of Vegetation in Erosion Control

Vegetation reduces the risk of water erosion of soil through leaves and stems, partially dissipating the work of water flow or raindrops, resulting in reduced energy impacting the soil. Dense spatially uniform vegetation cover can reduce flow velocity significantly compared with very open, clustered vegetation cover (Morgan and Rickson,

2003). Gyssels et al. (2003) stated that plant cover is the only parameter that influences soil loss in splash erosion, while both plant roots and cover must be considered in gully erosion. Fibrous root vegetation systems are more effective in soil erosion control than taproot vegetation system (Reubens et al., 2007; De Baets et al., 2008; Stokes et al., 2009, Vannoppen et al., 2015) because their larger root-soil contact area enables the formation of water-stable sediments (Jastrow et al., 1998, Zhou and Shangguan, 2005; De Baets et al., 2007).

Vegetation also improves slope stability through binding soil particles and anchorage from their roots. Vegetation helps to reduce erodibility by transferring shear stress in soil to tensile resistance of roots and restraining soil movement (Wu et al., 1979). Tall growth of trees adds a surcharge to the slope and increases normal and down-slope force components by their weight (Coppin and Richards, 1990). Also, foliage evaporation and interception restrain the build-up of pore water pressure in soil (Clark and Wynn, 2007). In this thesis, the work will mainly discuss the influence of grass in combination with turf reinforcement mats. The network of grass fibers forms a tensile mat effect that restrains the underlying soil.

2.2.3 Role of TRM and Vegetation System in Erosion Control

TRMs provide three main positive effects: soil retention, early growth, and fully established vegetation. In the unvegetated condition, TRMs improve seed germination and development by retaining soil moisture and temperature. At the early growth of vegetation, TRMs reduce shallow slippage of newly germinated seedlings, and when vegetation grows to a mature state, TRMs provides reinforced ground cover (Theisen and Carroll, 1990).

Because TRMs and vegetation both contribute to soil erosion control, it is necessary to study the combined effect of the TRM-soil system in erosion resistance. Previous research indicates natural vegetation and surficial soil particles are easily removed by water flow but TRMs improve lateral continuity of the soil-vegetation systems (Zhong et al., 2007).

Surface roughness, which is quantified using Manning's coefficient, controls the velocity of runoff and is influenced by soil particle size, surface topography, and vegetation (Morgan and Rickson, 2003). Figure 2-1 illustrates how Manning's coefficient changes as a function of vegetation condition and turf reinforcement mat covering. In the unvegetated condition, Manning's coefficient is between 0.035 and 0.037 for ECP-3 covering while Manning's coefficient is over 0.04 for a TRM product called T-RECS. For the same water depth, vegetated TRM covering increases Manning's coefficient by 0.008 compared with unvegetated TRM covering. Also, Manning's coefficient for vegetation covering over 52 weeks is higher than that for vegetation covering after about 6 weeks. Thus, TRM covering and a longer vegetation growth period contribute to improving soil surface roughness.

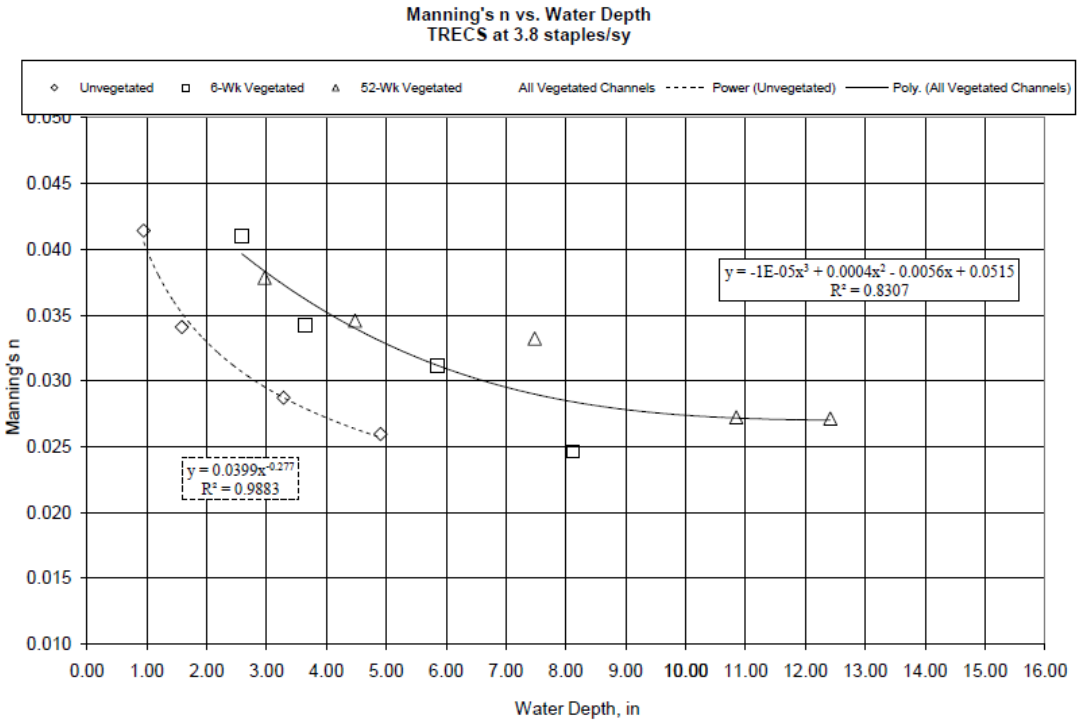

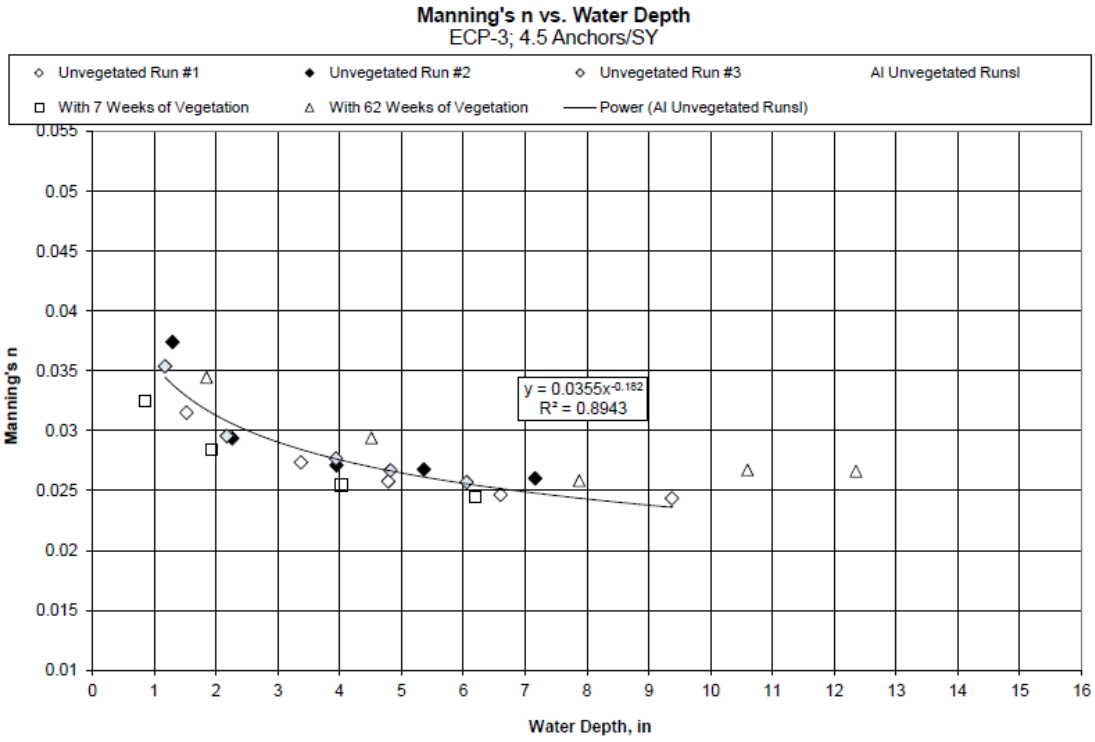

Figure 2-1. Manning's coefficient versus water depth (from NTPEP report).

2.3 Summary of TRMs listed in AASHTO NTPEP

NTPEP (National Transportation Product Evaluation Program) Datamine is an online resource that provides data and audit reports for current and past NTPEP evaluations of products and processes in traffic safety, construction, and maintenance under the management of the AASHTO (American Association of State Highway Transportation Officials). Based on information collected from NTPEP, none of these products is certified; however, some of them have been put into use by the DOTs (Department of Transportation) in most states (Table 2.8). The type and category of approved products are different from ECTC classification in each state as explained in 2.1.3. This discrepancy of categorization in different states brings difficulties in the selection of TRMs. Also, there is a discrepancy in defining HPTRM and TRM products between the NTPEP and manufacturer's brochures.

Table 2.8 – List of TRM Products in NTPEP Reports

Product name	Manufacturer	Suggested ECTC classification	Composition
SC 250	Western Excelsior	Type 5C TRM	70% straw, 30% coconut
P550	Western Excelsior	Type 5C TRM	100% polypropylene
Excel PP5-10	Western Excelsior	Type 5C TRM	100% Synthetic
US-2P10	U.S. Erosion Control Products	Type 5C TRM	100% Polymer
Recyclex TRM - V	American Excelsior	Type 5B TRM	100% Recycled Post Consumer Polyester
TriNet Recyclex	American Excelsior	Type 5C TRM	100% polypropylene
TriNet Coconut	American Excelsior	Type 5C TRM	Coconut Fibers/ Polypropylene Nets

TriNet Curlex	American Excelsior	Type 5C TRM	Excelsior Fibers/ Polypropylene Nets
TriNet Straw/Coconut	American Excelsior	Type 5C TRM	Straw coconut Fibers/ Polypropylene Nets
Enviroscape ECM	Enviroscape ECM	Type 5A TRM	100% Polypropylene
ECP-3	East Coast Erosion Blanket	Type 5C TRM	100% polypropylene
ECSC-3	East Coast Erosion Blanket	Type 5C TRM	70% straw, 30% coconut fiber
ECP-2 10	East Coast Erosion Blanket	Type 5C TRM	100% polypropylene
T-RECS	East Coast Erosion Blanket	Type 5C TRM	100% polypropylene
PC42	East Coast Erosion Blanket	Type 5B TRM	70% polypropylene / 30% coconut
PS42	East Coast Erosion Blanket	Type 5B TRM	67% Polymer, 33% Agricultural straw
P42	East Coast Erosion Blanket	Type 5B TRM	100% polypropylene
PP5-Xtreme	East Coast Erosion Blanket	Type 5C TRM	100% polypropylene
ECC-3	East Coast Erosion Blanket	Type 5C TRM	100 % Coconut
ECP-2	East Coast Erosion Blanket	Type 5C TRM	100 % polypropylene
Landlok 435	Propex Operating Company	Type 5B TRM	100 % polypropylene
Landlok 450	Propex Operating Company	Type 5C TRM	100 % polypropylene

Pyramat 25	Propex Operating Company	Type 5C TRM	100 % polypropylene
Pyramat 50	Propex Operating Company	Type 5C TRM	100 % polypropylene
Pyramat 75	Propex Operating Company	Type 5C TRM	100 % polypropylene
ETPP-10	Erosion Tech	Type 5C TRM	100% Crimped Polypropylene Fibers
C350	North American Green, Inc.	Type 5C TRM	100 % Coconut
P300	North American Green, Inc.	Type 5C TRM	100% Polypropylene

2.4 Anisotropy of Fabric Mechanical Properties

TRMs are classified as woven fabrics, which are commonly highly anisotropic in measured mechanical properties in the warp (machine) and weft (cross-machine) directions. The earliest study on the anisotropy of bending rigidity (stiffness) and tensile modulus was conducted by Peirce (1930), who proposed an equation to calculate bending rigidity in any direction of fabric based on tested rigidity in warp and weft directions. The lab testing method he used was also implemented in ASTM standard D1388, D6575, and D7748. Go et al. (1958), Chapman et al. (1972), and Shinohara et al. (1980) proposed mathematical models to estimate fabric bending rigidity in various directions (Table 2.9). Quantitative experimental studies provided measured values of fabric mechanical properties for different woven materials. Cooper (1960) produced a bending stiffness diagram in various directions. Meanwhile, some publications discussed anisotropy-influenced fabric failure mechanisms in tensile and shear tests. The earliest study on

anisotropic tensile properties of woven fabric was conducted by Kilby (1963). He assumed fabrics were anisotropic materials and displayed Poisson's effect by considering symmetry at different plane angles. Lo Wing Man (2001) did a comprehensive study on fabric anisotropy which focused on the anisotropy of hysteresis in mechanical properties by comparing the experimental and numerically simulated results. Yokozeki et al. (2006) evaluated the anisotropic characteristics of corrugated composites where the transverse direction was more flexible in deformation and extension. Zheng et al. (2008) found that non-orthogonal yarns of twill fabrics that affected their anisotropic distributions through a novel multiaxial tensile test approach. Pan et al. (2015) concluded that friction between the machine and cross-machine directions of a plain-weave fabric influenced connectivity and mobility of the fabric network thus both the anisotropy before and after yarn realignment affected the fabric ultimate tensile strength. Zouari et al. (2016) studied global and local anisotropic behaviors through tensile testing of twill, plain, and satin weave textiles and concluded that fabric structure anisotropy resulted in anisotropy in tensile properties. Kamali (2017) proposed a semi-empirical model to estimate tensile behavior and fabric structure under stresses in an arbitrary direction. Zhang et al. (2017) found that anisotropic tensile behaviors of PTFE coated glass fibers accounted for by the fiber crimp degree. They also proposed a constitutive model to analyze cyclic tensile behaviors and creep properties in an arbitrary direction. Cappello et al. (2018) indicated that increasing mechanical anisotropy of knit and woven textiles could improve the motion range and output force of an actuator. Semeraro et al. (2020) developed a new approach to predict the local orientation of woven materials to compute anisotropic mechanical properties. Table 2.10 summarizes the ultimate tensile strength/strain collected from NTPEP reports.

Table 2.9 – Mathematical Models to Estimate Anisotropic Fabric Bending Property.

Equations	Remarks	Reference
$B_\theta = \left[\frac{cos^2\theta}{\sqrt{B_1}} + \frac{sin^2\theta}{\sqrt{B_1}}\right]^{-2}$	Applicable for homogenous elastic materials	Peirce, 1930
$B_\theta = \left[\sqrt{B_1}cos^2\theta + \sqrt{B_2}sin^2\theta\right]^2$	Isotropic and circular polar diagrams	Shinohara et al, 1980
$B_\theta = B_1cos^4\theta + B_2sin^4\theta$	Useful to describe the behavior of small restrictive and open fabrics	Go et al, 1958
$B_{mean} = \frac{3}{8}(B_1 + B_2)$	Only applicable to balanced plain weaves	Go et al, 1958
$B_\theta = B_1cos^4\theta + B_2sin^4\theta + (J_1+J_2)cos^2\theta sin^2\theta$	Considered twisting effect	Cooper, 1960
$B_\theta = B_1cos^4\theta + B_2sin^4\theta + (4B_{45} - B_1 - B_2)cos^2\theta sin^2\theta$		Chapman et al, 1972

where B_θ, B_1, B_2, and B_{45} are bending rigidities in θ, warp, weft, and ±45 directions.

Table 2.10 – Anisotropic Tensile Properties of TRMs

Product name	Ultimate tensile Strength MD/TD (kN/m)	Ultimate tensile Strain MD/TD (%)
SC 250	11.86/9.32	28.9/20.3
P550	13.68/13.45	18.9/17.6
Excel PP5-10	5.5/2.73	24.9/34.5
PP5-Xtreme	67.45/55.73	27.6/22.8
US-2P10	6.83/3.59	26.7/23
Recyclex TRM - V	4.41/2.47	29.6/32.1
TriNet Recyclex	11.74/12.32	16.3/16.1
TriNet Coconut	11.55/10.21	19.2/16.8
TriNet Curlex	11.76/11.04	15.1/15.5
TriNet Straw/Coconut	9.97/6.39	18.8/14.9
ECP-3	12.89/12.49	17/15.3

ECSC-3	13.68/13.46	19.8/18.7
ECP-2 10	6.76/3.54	25.5/24.1
T-RECS	57.59/58.43	22.3/16.5
PC42	6.53/3.38	28.5/30.7
PS42	5.61/3.24	29.3/31.3
P42	6.08/3.15	25.2/30.6
ECC-3	11.25/10.37	16.5/18.7
ECP-2	6.27/4.06	28.5/28.8
Landlok 435	7.34/4.83	24.1/22.9
Landlok 450	8.02/4.89	22.7/21.9
Pyramat 25	48.55/38.4	28.6/25.1
Pyramat 50	67.89/51.32	48.3/35.9
Pyramat 75	72.9/53.75	45/33.2
ETPP-10	7.48/4.68	23/22
C350	13.23/12.63	25/19.9
P300	6.14/4.27	24.9/26.4

2.5 Fabric Bending Rigidity Measurement Approaches

Fabric bending rigidity, which is also called stiffness or flexural rigidity, is a property that expresses the resistance of a fabric to bending, and its impact on fabric drape ability and final geometry of composites (Lammens et al., 2014). In the mechanics of material, bending rigidity is defined as the first derivative of the moment-curvature curve. Several testing methods exist to measure fabric bending rigidity including the cantilever method, loop method, and quasi-three-point bending test.

2.5.1 Cantilever test

The most widely used method is the cantilever method (ASTM D1388 and D7748) which was developed by Peirce (1930). The cantilever method was originally designed

with a flexometer (Figure 2-2) by fixing one end of a fabric strip and allowing the other side of fabric bending under its weight (Sun 2008; Peirce, 1930). The bending rigidity is calculated by Equation 3 (Sun, 2008; Ghosh and Zhou, 2003; Clapp et al,1990):

$$G = \frac{wl^3 \cos\left(\frac{\theta}{2}\right)}{8 \tan\theta} \tag{3}$$

where w = weight per unit area;

l = overhang length of the fabric strip;

θ = deflection angle of the fabric strip from the horizontal direction.

The simplified equation for bending rigidity is expressed in Equation 4:

$$G=wc^3 \tag{4}$$

where the bending length c is

$$c = \sqrt[3]{\frac{G}{w}} = l \cdot \sqrt[3]{\frac{\cos\left(\frac{\theta}{2}\right)}{8\tan\theta}}$$

Pierce's equation is derived from a simple beam deflection equation (Equation 5)

$$y = \frac{Wx^4}{8EI} \tag{5}$$

Thus, bending rigidity is (Equation 6)

$$B = \frac{EI}{b} = \frac{Wx^4}{8yb} = \frac{Wx^3}{8b\frac{y}{x}} \tag{6}$$

where *W* is the weight per unit length (*N/m*), *x* is the horizontal distance between the two ends of the beam, *y* is the deflection of the flexible beam end, *b* is the width of the beam, E is the modulus of elasticity (N/m^2) and *I* is the moment of inertia (m^4).

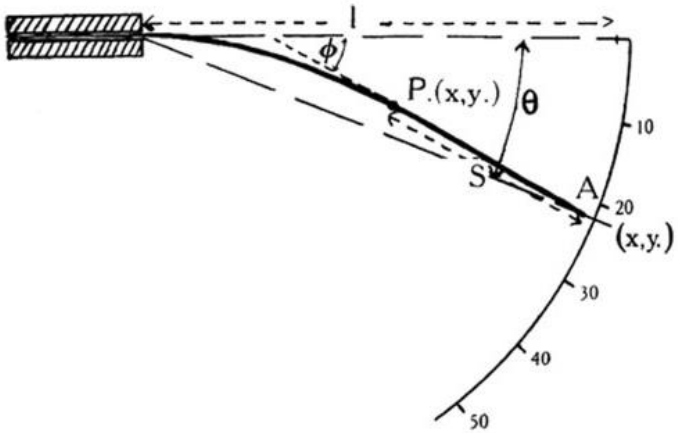

Figure 2-2. Peirce cantilever test configuration (after Peirce, 1930)

ASTM standard specifies the inclined surface angle as 41.5°, thus $\sqrt[3]{\frac{\cos\left(\frac{\theta}{2}\right)}{8\tan\theta}}$ is approximately equals to 0.5. Lammens et al. (2014) demonstrated the inaccuracy in measuring stiffness using ASTM D1388 because the equation in the standard neglects the higher-order effects of the differential equation to describe simple beam bending. They suggested that Peirce's equation is more applicable for fabrics with a small specific weight.

2.5.2 Loop test

Different from the cantilever test, the loop method refers to hanging down a strip by self-weight in the form of a loop with fixed ends. The bending rigidity is a function of loop height. Peirce did heart, ring, and pear loop tests. Takatera and Shinohara (1996) conducted a heart loop test on nylon and polyester/cotton twill strips. Santillan et al. (2006; 2005) performed hanging pear loop and standing wrinkle tests on polycarbonate strip. Plaut and Virgin (2014) used a polycarbonate strip to conduct the standing ring test. Mahadevan and Mahadevan & Keller (1999) compared bending lengths between paper and plastic strips with a free fold test. Figure 2-3 depicts the loop test configurations mentioned above.

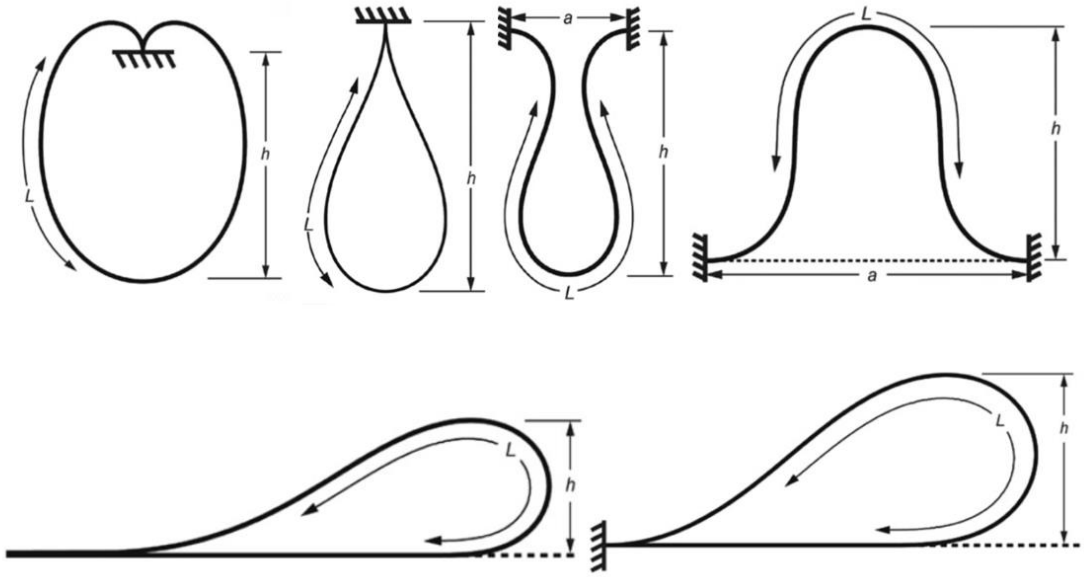

Figure 2-3. From left to right: heart loop test, hanging pear loop test, hanging wrinkle test, standing wrinkle test, free fold test, clamped fold test (after Plaut, 2015)

Plaut (2015) developed dimensionless parameters to estimate the bending rigidity of a fabric strip, which include dimensionless weight $\hat{w}$, dimensionless height $\hat{h}$ and dimensionless distance $\hat{a}$.

$$\hat{w} = \frac{wL^3}{Bb}, \qquad \hat{h} = \frac{h}{L}, \qquad \hat{a} = \frac{a}{L}$$

where *w*, *B*, *b* are defined as the same parameters in previous equations, *L* is the total length of the loop between two ends, *h* is the height of the loop and *a* is the separation distance between clamped ends of the strip in hanging wrinkle test and standing wrinkle test. Then Plaut applied elastic analysis in developing a polynomial relationship between $\hat{w}$ and $\hat{h}$. Plaut's study provided an alternative formula to estimate the bending rigidity of fabrics without performing laboratory tests. Table 2.11 summarizes the formula for different loop tests.

Table 2.11 – Loop Test Formula Represented by Dimensionless Parameters (after Plaut, 2015)

Types of loop test	Equations	Range
Cantilever test	$\hat{w}$=-0.025948+10.2934$\hat{h}$-288072$\hat{h}^2$ +134.383$\hat{h}^3$ -236.785$\hat{h}^4$+164.894$\hat{h}^5$	0≤$\hat{h}$≤0.8 0≤$\hat{w}$≤16
Heart loop test	$\hat{w}$=930-21280$\hat{h}$-166985$\hat{h}^2$-535406$\hat{h}^3$ +668737$\hat{h}^4$	0.13386≤$\hat{h}$≤0.349 0≤$\hat{w}$≤1000
Hanging pear loop test	$\hat{w}$=-0.025948+10.2934$\hat{h}$-288072$\hat{h}^2$ +134.383$\hat{h}^3$ -236.785$\hat{h}^4$+164.894$\hat{h}^5$	0.424308≤$\hat{h}$≤0.466 0≤$\hat{w}$≤2500
Hanging wrinkle test	$\hat{w}$=3.127798×10^7-3.011912×$10^8\hat{h}$+1.087908×$10^9\hat{h}^2$ -17470668×$10^9\hat{h}^3$ +1.0525584×$10^9\hat{h}^4$	0.403132≤$\hat{h}$≤0.444 0≤$\hat{w}$≤2200
Standing wrinkle test	$\hat{w}$=1.226765×10^6-1.92634×$10^7\hat{h}$+1.2118318×$10^8\hat{h}^2$ -3.813567×$10^8\hat{h}^3$ +6.00006×$10^8\hat{h}^4$-3.77459×$10^8\hat{h}^5$	0≤$\hat{w}$≤500
Free fold test	$\hat{w}$=0.74515/$\hat{h}^3$	0≤$\hat{w}$≤2000
Clamped fold test	$\hat{w}$=2963-35969$\hat{h}$-149972$\hat{h}^2$-219888$\hat{h}^3$	0.424308≤$\hat{h}$≤0.466 0≤$\hat{w}$≤368

2.6 Quasi-static and Dynamic Penetration of Fabrics

Experimental and numerical studies of quasi-static and dynamic penetration of fabrics focused on analyzing damage of fabrics due to long-term heavy masses and dynamic impacts on fabric surfaces.

Standard quasi-static puncture testing of geotextiles can be traced back to ASTM D751-79 for testing coated fabrics. Current standards include ASTM D4833 for pin testing,

D5495 for pyramid puncture testing, and D6241 for CBR testing. Only the CBR puncture test has an equivalent test method in ISO12236. Methods of ASTM D4833 and D6241 are similar except the differences of probe diameter, compression speed, and specimen size. Atmatzidis and Chrysikos (2002) investigated correlations between static puncture strength and tensile strength of nonwoven PP (polypropylene) geotextiles and determined a linear relationship between puncture resistance and wide-with tensile strength as well as mass per unit area. Hsieh and Wang (2008) found puncture resistance values tested by ASTM D6241 were higher than those obtained by ASTM D4833. Van Dyke (2014) studied linear correlations between CBR and pin puncture strengths for woven polypropylene geotextiles. Koerner and Koerner (2011) compared three standard puncture tests as summarized in Table 2.12. They also performed three tests on PP and PET (polyester) needle punched non-woven geotextile and concluded that both pyramid and CBR puncture resistance are greater than pin puncture test results. The results also indicated that the puncture resistance of geotextiles is linearly related to fabric mass per unit area. However, Jones et al. (2000) concluded that CBR puncture resistance was in a nonlinear relationship with mass per unit area of needle-punched non-woven geotextiles, but linearly related with tensile strength in cross-machine direction by conducting CBR testing. Jones et al. (2000) also stated that CBR puncture resistance provided "a better indication of protection performance" compared with other index testing such as tensile strength and drop cone tests. The static puncture failure curve is composed of fiber rearrangement, fiber tension, and monofilament rupture (Van Dyke, 2014, Askari, et al., 2012). Inter-fiber friction should be considered during the puncture test (Van Dyke, 2014; Jones, et al., 2000). Typical failure stages of fabric are depicted in Figure 2-4.

Table 2.12 Comparison of ASTM D4833, D5494 and D6241 test methods (after G.R. Koerner and R.M. Koerner, 2011)

	D4833	D5494	D6241
Shape of probe	8.0 mm in diameter	pyramid shape	50 mm in diameter
Specimen size	50 mm in diameter	150 mm in diameter	150 mm in diameter
Rate of penetration	300±10 mm/min	1 mm/min	50 mm/min
No. of specimen	15	10	10
Lab temperature	21±2°C	21±2°C	21±2°C
Relative humidity	65±5%	50~70%	50~70%
Reported data	Max resistance at break	Max resistance at break	Max resistance at break

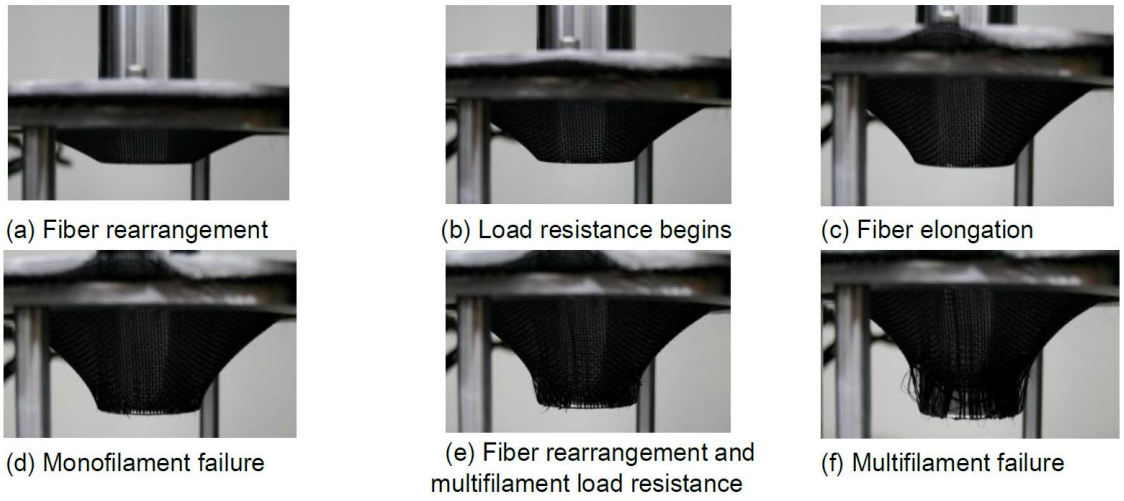

Figure 2-4. Failure stages of a woven geotextile under CBR test (after Van Dyke et al., 2016)

There are additional tests to measure puncture resistance of fabrics. For example, Wang et al. (2011) performed a quasi-static puncture test on woven fabric samples using a probe with a flattened end show as Figure 2-5. Cheah et al. (2015) conducted a drop rock test on non-woven geotextiles and measured retained static puncture resistance after drop rock test. They concluded that the retained puncture resistance after drop rock test "could decrease as much as 26%". Baucom and Zikry (2003) discussed failure modes of quasi-

static perforation on GFRP (Glass-fiber-reinforced plastic), such as the evolution of rupture, fiber fracture, matrix cracking, and delamination. After comparing the test results of 3D and 2D woven systems, they concluded that 3D woven systems are better than 2D systems because the interaction between surface weft leads to energy dissipation in a larger area.

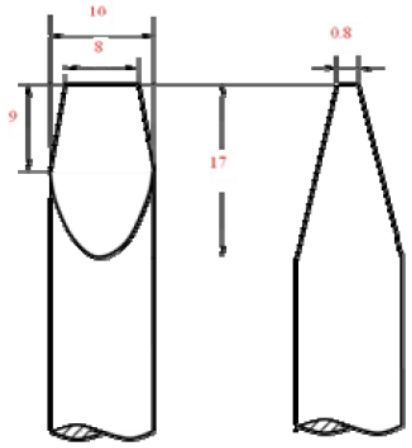

Figure 2-5. The shape and size of the projectile in a quasi-static puncture test where the unit of the length is mm (Wang et al., 2011).

There are also some previous studies on static puncture mechanisms. Termonia (2006) devised a comprehensive model for deformation and damage of woven fabrics under small projectile impacts, which provides a deeper understanding of the stages of puncture failure. Termonia summarized the four steps of puncture failure as (1) the initial steady increase in force with penetration of tip due to contact pressure between the tip and fiber strand; (2) a sudden drop of force due to slippage of cylinder behind the tip into inter-fiber space; (3) another increase in force due to friction of cylinder against fabric; and (4) a steady decrease in force due to further penetration of cylinder behind the tip (Figure 2-6). The advantage of the model is that it accounts for yarn slippage effects within clamps.

Before this, Termonia (2004) proposed another model to simulate yarn fracture with an impact rate of a spherical projectile. Yahya et al. (2012) performed a FE analysis of impactor shapes influences on plain weave fabrics and concluded that fabric puncture was dominated by crimp interaction and yarn extension.

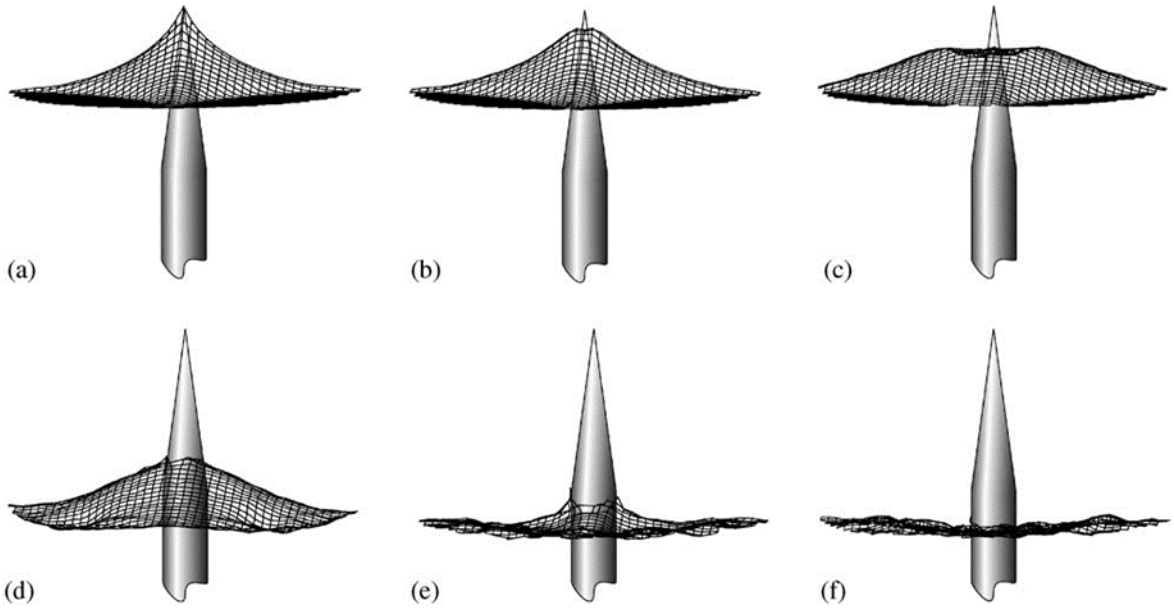

Figure 2-6. Deformation of fabric during penetration of a needle projectile (Termonia, 2006)

Lee et al. (2001) performed experimental and numerical studies on the ballistic impact of FRP (fiber-reinforced composites). They found that FRP composites absorbed more energy than dry reinforcing fabrics because resin matrix constrains yarn mobility in a composite, which means that "fiber straining is responsible for most energy absorption" in penetration. Tan et al. (2005) observed very high-level tension of fabric and slippage of clamped edges when performing a ballistic test on a woven fabric. They also concluded that fabric absorbed energy transfer to strain energy by elongation of yarns and kinetic energy by moving fibers closer to the impact point, which were observed as deformation into a pyramid with a rhombic base at the location of impact. Jia et al. (2012) indicated that

the ballistic impact caused the same deformation in machine and cross-machine directions using a FEA fabric model in Abaqus.

The dynamic perforation test (ISO13433, 2006) can be thought of as a modified type of ballistic impact even though the shape of the projectile and the acceleration and velocity when the projectile drops on fabric is not as fast as a real ballistic test. The failure mode from the previous study on the ballistic impact tests can be compared with a dynamic perforation test since both of the tests simulate the dynamic impact on fabrics. Compared with the dynamic perforation test, performing a static puncture test makes it easier to monitor deformation of the fabric at different stages.

CHAPTER 3. PHYSICAL BEHAVIORS OF TRMS

This chapter will provide physical property testing of seven turf reinforcement mats. The tests were performed using the American Society for Testing and Materials (ASTM) Standards and Erosion Control Technology Council (ECTC) test methods. A detailed description of TRMs selected, the test method used, and the results will be presented in this chapter.

3.1 Introduction

3.1.1 Background

The rapidly growing RECP (Rolled Erosion Control Products) market has led to the development of a wide variety of turf reinforcement mats (TRMs). TRMs are made from synthetic fibers such as polypropylene (PP) and combinations of different natural or synthetic fibers. People use TRM in practice but there are limited studies to evaluate the performance of the TRM materials. For example, the National Transportation Product Evaluation Program (NTPEP) provides a laboratory evaluation summary of erosion control products in 2016. Table 3.1 showed the mass per unit area of TRMs from the NTPEP report. For materials with similar woven structure, Pyramat 25, 50, and 75 are woven polypropylene TRMs without fill material. Their mass per unit area is dependent on the density of woven structures which was evidenced by light penetration values. We can also observe triple-netted synthetic TRMs such as PP5 and ECP-3 have higher mass per unit area compared with double-netted synthetic TRMs such as P300 and US-2P10. Triple-netted synthetic TRMs with fill material of coconut and straw such as ECC-3 and ECSC-3

have medium mass per unit area but relatively low light penetration. Thus, mass per unit area of TRMs is influenced by woven or netting structure and fill material. Netting structures with a higher density of weave yarns and fill material will lead to greater mass per unit area.

Table 3.1 – Mass per unit area and light penetration data of TRMs from NTPEP

Manufacturer	Product	Mass/Area (g/m^2)	Light penetration (%)
North American	P300	436.0	25.5
	C350	508.2	10.9
	P550	783.6	8.9
Propex	Pyramat 75	442.1	7.7
	Pyramat 50	424.5	10.0
	Pyramat 25	259.7	21.9
Western Excelsior	PP5-10	353.6	24.0
East Coast Erosion Blankets	ECP-2	465.2	15.1
	ECP-3	683.9	10.5
	ECP-2 10	312.3	26.3
	ECC-3	436.4	8.8
	ECSC-3	454.7	6.2
Environscape ECM	P5000	331.6	23.3
US Erosion Control Products	US-2P10	389.9	14.0

3.1.2 Motivation

Despite the widespread use of turf reinforcement mats, engineers are often given little guidance on the design and selection of TRMs beyond maximum allowable slopes and shear stresses. Many different types of TRMs often meet the requirements for a particular set of site conditions. For example, for one horizontal to half vertical (1H:0.5V) slope, different kinds of TRMs with different polymer and natural fiber nettings and matrices can meet the design requirements for the site. Different TRMs, however, can vary

significantly in basic index properties, laboratory performance, and overall field performance. In this research, the relationship between basic index properties and product performance in both laboratory and field conditions will be investigated while summarizing typical indices that can distinguish HPTRMs from TRMs or other RECPs.

3.1.3 Research questions

A variety of standardized testing can be conducted to evaluate and classify turf reinforcement mats. The objective of this chapter is to test several turf reinforcement mats using ASTM standard methods and evaluate which TRM material has good performance. Besides, this chapter will investigate if these physical properties affect a TRM's performance. This chapter will also investigate the relationship between index properties and performance: such as the relationship between mass per unit area and tensile strength, relationship thickness and seedling emergence, and the relationship between mass per unit area and shear force. The scope of this chapter is limited to standard index tests.

3.2 Materials and Methods

3.2.1 Seven turf reinforcement materials

The seven materials tested in the thesis are provided from four different manufacturers, Propex, East Coast Erosion Control, Western Excelsior, and North American Green. Figure 3.1 shows the photos of the seven turf reinforcement mats tested in this chapter. The manufacturer's brochure defines Landlok 300 as TRM while the others are listed as HPTRMs. However, based on NTPEP reports and the ECTC standards, only VMax W3000 is HPTRM while the other six are TRMs.

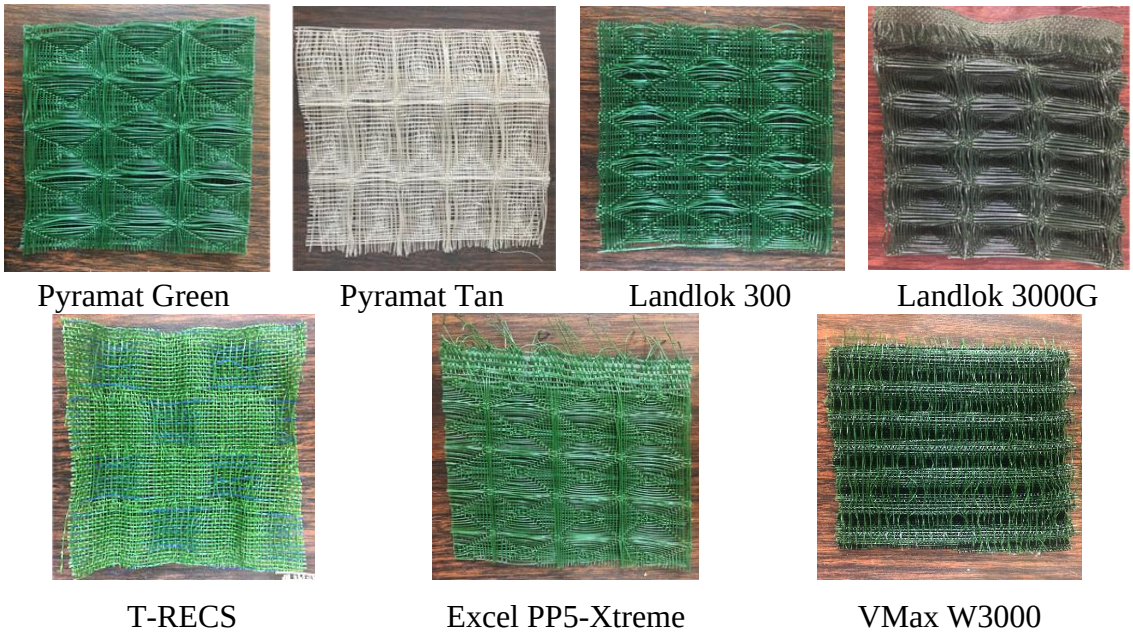

Figure 3-1. Photographs of the TRMs used in this study (12 cm×12 cm specimens).

For Landlok 300, Pyramat Green, and Tan with lattice structure, the lattice size is 2.7 cm (21 yarns) × 4.1 cm (27 yarns). For Landlok 3000G, the lattice size is 2.0 cm (27 yarns) × 3.7 cm (33 yarns). The lattice size of Excel PP5-Xtreme is 2.4 cm (23 yarns) × 3.8 cm (27 yarns). Yarns of TRMs except Excel PP5-Xtreme have an "X3 fiber technology" in the cross-section areas which provide greater surface area. Although they have similar lattice structure, their yarn densities (number of yarns within a specific length) are different. Vmax W3000 has a special multi-layered woven structure with a corrugated middle layer "interlaced into the woven top and bottom layers" while T-RECS has a unique dome shape structure.

As a permanent solution for erosion control in high flow channels and on critical slopes, all seven turf reinforcement mats are manufactured by synthetically made polymers called polypropylenes (PP), which have very high chemical resistance, low moisture

absorption, and UV resistance. With different weaving, thickness, mass, and bond type, TRMs have a range of characteristics. Thus, determining the physical, mechanical, and hydraulic properties of TRMs becomes a crucial step in the proper selection of TRMs. Basic index properties of the seven TRMs and relative performance properties provided by manufacturers are summarized in Table 3.2 and 3.3.

Table 3.2. Material Index Properties Provided by the Manufacturers.

TRMs	Mass/Area (g/m^2) ASTM D6475	Thickness (mm) ASTM D6525	Light Penetration (%) ASTM D6567	Tensile Strength* MD×TD (kN/m) ASTM D6818
Pyramat(Green), Propex	457.7	10.2	15%	58.4 × 43.8
Pyramat(Tan), Propex	457.7	10.2	15%	58.4 × 43.8
Landlok 300, Propex	281	7.6	50%	35.0 × 29.2
Landlok 3000G, Propex	-	-	-	-
T-RECS, East Coast Erosion Control	288.2	11.4	34%	44× 44
Excel PP5-Xtreme, Western Excelsior	312	8	30%	59 × 44
VMax W3000, North American Green	495	10.2	12%	52.6 × 55.5

*Tensile strength is the maximum stress a TRM can experience while being pulled before failure.

Table 3.3. Material Performance Provided by the Manufacturers.

TRM	Tensile elongation[1] ASTM D6818	UV stability[2] ASTM D4355	Seedling emergence ECTC Method 4	Fully vegetated shear stress and velocity ASTM D6460
Pyramat(Green), Propex	40×35%	90% @6000 hours	296%	766 N/m^2 6.1 m/s

Pyramat(Tan), Propex	40×35%	90% @6000 hours	296%	766 N/m^2 6.1 m/s
Landlok 300, Propex	50%	90% @3000 hours	296%	576 N/m^2 6.1 m/s
Landlok 3000G, Propex	-	-	-	-
T-RECS, East Coast Erosion Control	17%	91% @6000 hours	636%	718 N/m^2 7.6 m/s
Excel PP5-Xtreme, Western Excelsior	25×20%	90% @6000 hours	552%	814 N/m^2 7.6 m/s
VMax W3000, North American Green	35×20%	80% @ 3000 hours	-	766 N/m^2 7.6 m/s

[1]Tensile elongation is the ratio of the length of a TRM at failure relative to its original length.

[2]UV stability is a measure of how a geotextile will deteriorate due to exposure to ultraviolet light.

3.2.2 Test Method and Sample Preparations

Mass per unit area was measured in accordance with ASTM D5261, the Standard Test Method for Measuring Mass per Unit Area of Geotextiles. Other test methods such as ASTM D6475, Standard Test Method for Measuring Mass per Unit Area of Erosion Control Blankets, and ASTM D6566, the Standard Test Method for Measuring Mass Per Unit Area of Turf Reinforcement Mats can also be used to estimate mass per area of TRMs.

The main differences between these standards are specimen size and conditioning. The following table summarizes the test condition between the test methods.

Table 3.4. Requirements for ASTM Standard Mass per Unit Area Testing method

	ASTM D5261	ASTM D6475	ASTM D6566
Number of specimens	Minimum of 5	Minimum of 5	Minimum of 5
Specimen size (Combined total)	≥10000 mm^2 (≥100,000 mm^2)	≥1000 cm^2 (≥5,000 cm^2)	≥23,000 mm^2 (≥230,000 mm^2)
Temperature	21 ± 2 °C	Room temperature	21 ± 2 °C
Relative humidity	65 ± 5 %	None	60 ± 10 %
Dry oven	None	50 ± 5 °C	None

ASTM D6566 also suggests considering conducting comparative tests to determine statistical bias between different laboratories. Since there is a limitation of the information from manufacturers and other research institutes, all measured results in this thesis only represent data obtained in Sustainable Geotechnical Systems Laboratory at Georgia Tech.

Each specimen coupon is cut to 15 cm by 15cm for testing. During the process, no specimen fibers are lost during the weighing and moving of specimens to ensure the integrity of the specimens. Five specimens for each type of TRM were placed on a scale and weighed to the accuracy of 0.01g. Mass per unit area was calculated as the ratio of the mass to the area of the specimens (Equation 7):

$$m = \frac{M}{A} \tag{7}$$

where m = mass per unit area;

M = total mass of five specimens;

A = total area of five specimens.

Stiffness testing was performed according to ASTM D6575-16, the Standard Test Method for Determining Stiffness of Geosynthetics Used as Turf Reinforcement Mats, and ASTM D7748, the Standard Test Method for Flexural Rigidity of Geogrids, Geotextiles and Related Products.

Eight rectangular specimens (101.6 by 457.2 mm) were cut from for each type of TRM, with four of the specimens cut with the long dimension parallel to the machine direction and four of the specimens cut with the long dimension parallel to the cross-machine direction (Figure 3-2). Specimens were brought to temperature and moisture equilibrium in the test condition. The test was performed by sliding the specimen off the overhang using a slow and steady movement. The length of the overhang was measured when the tip of the test specimen was depressed under its own weight made an angle of 41.5 degrees with the horizontal (Figure 3-3). Four readings were taken from each specimen with each side up, first at one end and then the other.

Figure 3-2. Machine direction and cross-machine direction of seven materials.

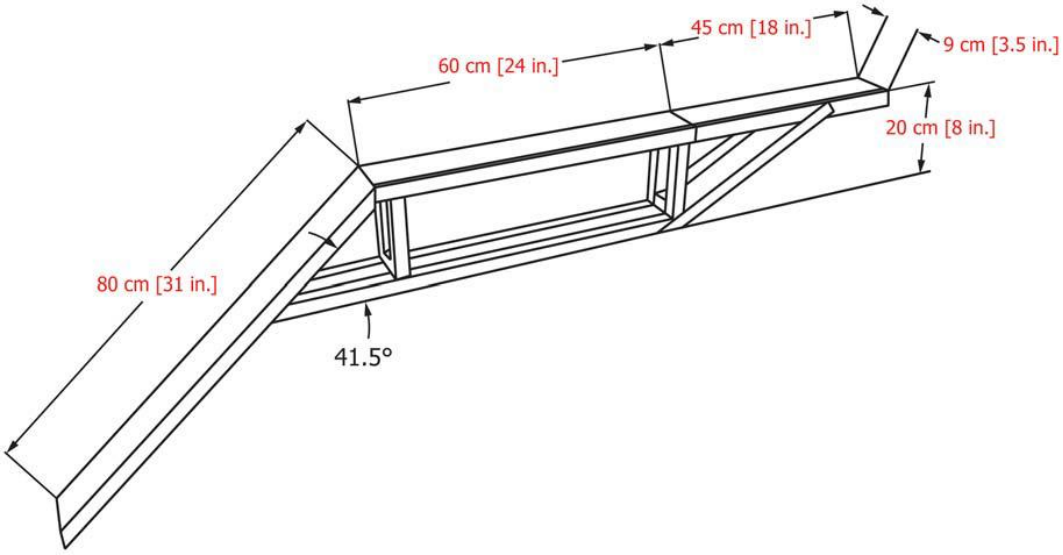

Figure 3-3. ASTM Standard D7748 test configuration.

Table 3.5 compares the requirements for ASTM Standard stiffness testing method from ASTM D 6575 and ASTM D7748. Despite the differences in specimen size and number of specimens, the measurement method and configuration are the same in both standards.

Table 3.5. Requirements for each ASTM Standard Stiffness Testing method.

	ASTM D6575	ASTM D7748
Number of specimens	4+4	5+5
Specimen size	≥101.6 × 457.2 mm	≥5× 90 cm
Temperature	21 ± 2 °C	21 ± 2 °C
Relative humidity	60 ± 10 %	50~70%

The flexural rigidity of the specimens was determined in accordance to (Equation 8):

$$G = W \times (\frac{L_o}{2})^3 \quad (8)$$

where L_o = length of overhang, cm

W = mass per unit area, mg/cm^2

G = flexural rigidity, mg-cm

The overall flexural rigidity is the geometric mean of the flexural rigidity as determined in the machine and cross-machine direction (Equation 9):

$$G_o = (G_{MD} G_{CD})^{1/2} \quad (9)$$

where G_o = overall flexural rigidity, mg-cm

G_{MD} = machine direction flexural rigidity, mg-cm

G_{CD}=cross-machine flexural rigidity, mg-cm

Static puncture testing was performed in accordance with ASTM D6241-14, the Standard Test Method for Static Puncture Strength of Geotextiles and Geotextile-Related Products Using a 50-mm Probe. The recorded puncture strength is the maximum force required to rupture a geotextile.

All TRM materials were prepared as 30cm × 30 cm coupons with a border length greater than the outer diameter of the clamping ring. The test specimen was clamped without tension between circular plates (Figure 3-4), and secured in a load testing frame. The load was then applied to the center of the unsupported portion of the test specimen by a steel plunger attached to a load indicator. The specimen was then loaded at a speed of 50 mm/min until failure occurred. Load-displacement data were recorded every two seconds during loading, and the puncture strength was read directly from the load-displacement curve. Tests were performed in triplicate on each specimen.

Figure 3-4. Test configuration for ASTM D6241 standard test.

The ***dynamic perforation test*** which is also called cone drop test, was performed in accordance with ISO 13433(2006), Geosynthetics-Dynamic perforation test (Figure 3-5). This test method measures the resistance of geosynthetics to penetration by a steel cone, of 45° tip angle, dropped from a fixed height (50 cm). The degree of penetration simulates the behavior of the geosynthetic when penetrated by sharp objects. The diameter of the punctured hole in combination with the drop height gives a measure of impact resistance (strength); that is, the smaller the diameter of the hole, the greater the impact resistance of the geosynthetic to damage during installation. In all tests, the fibers remained intact after penetration by the cone; however, the width of the penetration was highly dependent on the location of the drop. All TRM materials were prepared as 30 cm × 30 cm coupons which are suitable for the standard apparatus used in this study. Reference names of test locations are shown in Figure 3-6 and 3-7.

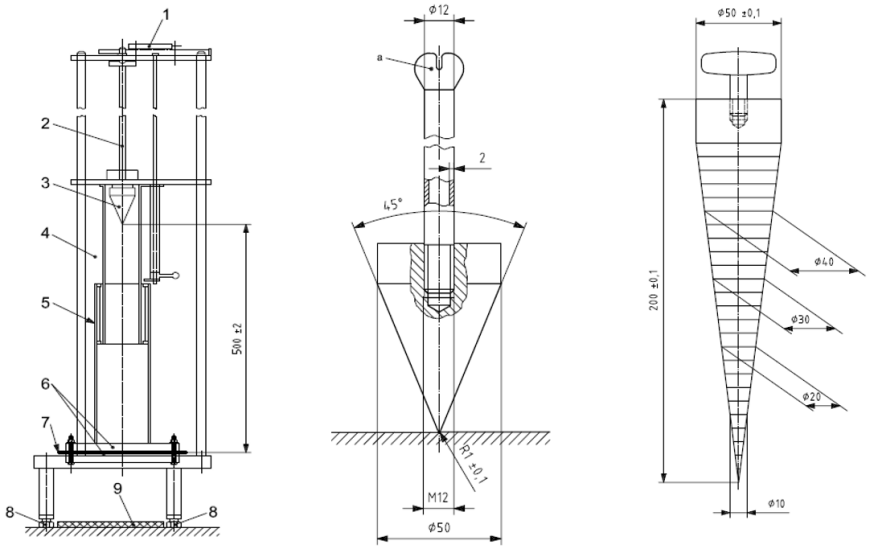

Figure 3-5 (a). Test configuration for ISO13433 dynamic perforation test

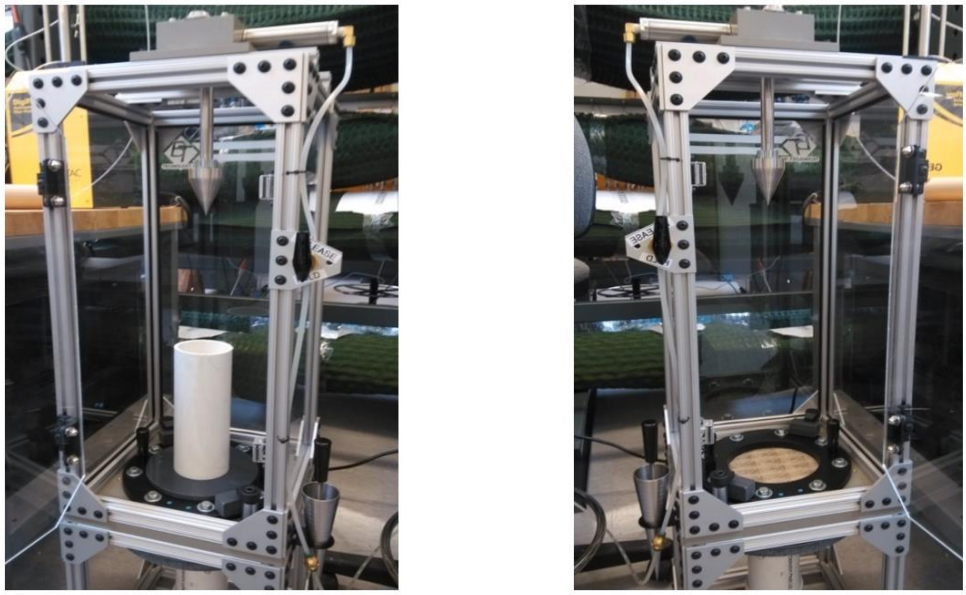

Figure 3-5 (b). Laboratory setup for dynamic perforation.

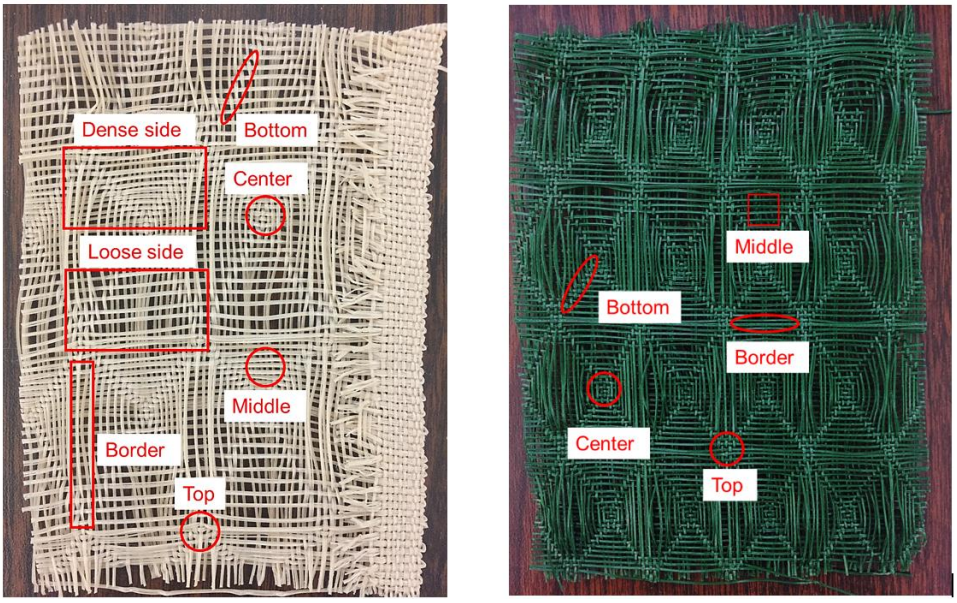

Figure 3-6. Test locations for Pyramat Tan and Pyramat Green; same test locations can also be applied to Landlok 300, Landlok 3000G, and Excel PP5-Xtreme as Pyramat Green.

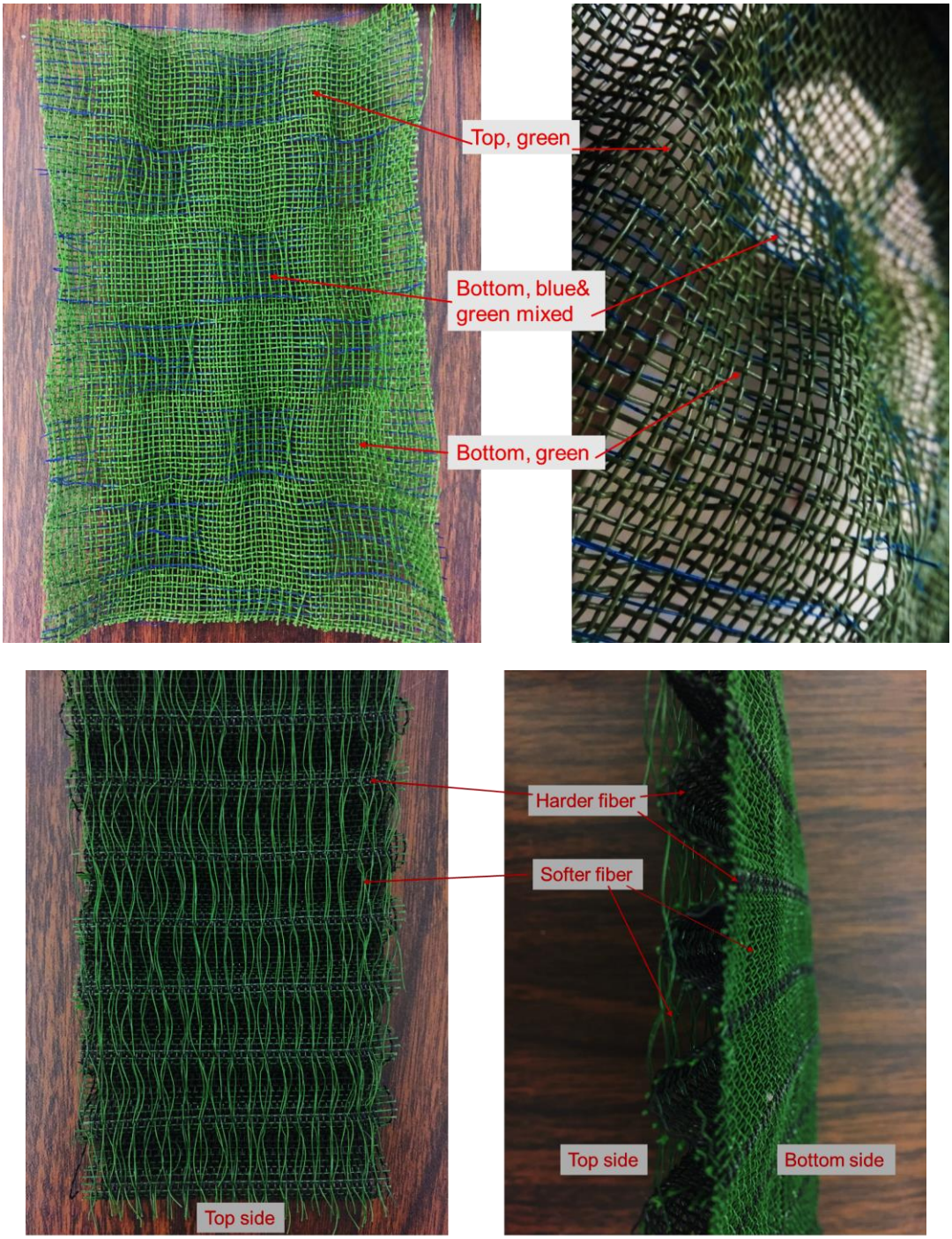

Figure 3-7. Test locations for T-RECS and VMax W3000.

Hydraulic conductivity ratio test to measure long-term properties of the soil-TRM system was performed following ASTM D5567. Flexible wall permeameter tests were performed to measure the hydraulic conductivity of a soil-HPTRM system (note that

ASTM D 5567 was used due to the low conductivity of the soil-HPTRM system). The HPTRM was placed on top of a layer of coarse filter soil and below a 2-inches thick layer of overburden soil (graded sand, F75 sand, or Piedmont soil). The grain size distribution curves of the three soils are displayed in Figure D-1 in APPENDIX. The system was placed in a latex membrane and was then encased in a fluid-filled cell that allowed the application of confining stress on the soil/HPTRM system. The saturated hydraulic conductivity of the soil/HPTRM system was then measured as a function of time until the flow stabilized.

3.3 Results

3.3.1 Mass per unit area

Mass per unit area testing was conducted to provide information on the mass per unit area and uniformity of the TRMs. Five specimens were tested for each TRM. Average mass per unit area results are given for each TRM in Figure 3-8. A comparison between lab measured mass per unit area results and manufacturer-provided values is shown in Table 3.6.

Table 3.6. Measured Mass per Unit Area of Seven Turf Reinforcement Mats Compared with Manufacturer's Value.

Sample Name	GT Measured Value (g/m^2)	Manufacturer's value (g/m^2)
Pyramat Green	455.8	457.7
Pyramat Tan	277.0	N/A
Landlok300	253.1	254.3
Landlok 3000G	355.4	N/A
T-RECS	289.2	288.2
Excel PP5-Xtreme	313.0	312
VMax W3000	493.1	495

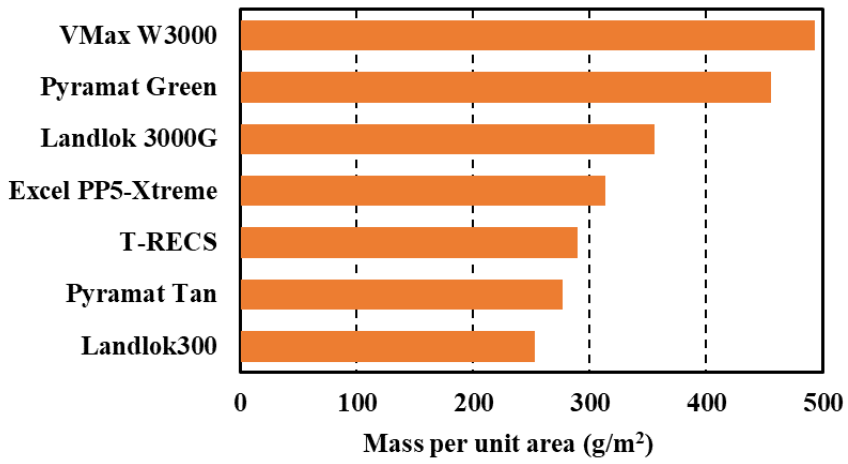

Figure 3-8. Mass per unit area of seven turf reinforcement mats.

As shown in Figure 3-8, VMax W3000 shows the greatest mass per unit area amongst the seven TRMs tested. With the exception of Landlok 300, the others are high-performance TRMs, as defined by manufacturers. Compared with the mass per unit area of other TRMs (Table 3.1) obtained from literature, the range of the mass per unit area is between 253.1 and 783.6 g/m^2 for TRMs while the range of the mass per unit area is between 277 and 493.1 g/m^2 for high-performance TRMs (HPTRM). Therefore, the mass per unit area alone is not enough to distinguish TRMs. Other index properties such as tensile strength and vegetated shear stress should be considered.

3.3.2 Stiffness

Stiffness testing was conducted to provide information on the stiffness of the TRMs to evaluate their ability to achieve intimate contact with the underlying soil surface and to analyze any trends with mass per unit area. Stiffness in the machine direction, cross-machine direction, and overall stiffness results for each TRM are presented in Table 3.7.

Table 3.7. Measured Stiffness Values of Seven Turf Reinforcement Mats.

Sample Name	Machine Direction (mg-cm)	Cross-Machine Direction (mg-cm)	Overall (mg-cm)
Pyramat Green	228,448	614,124	374,560
Pyramat Tan	198,703	243,602	220,010
Landlok300	166,340	216,881	189,937
Landlok 3000G	205,604	346,225	266,806
T-RECS	233,122	1,642,962	618,878
Excel PP5-Xtreme	230,436	862,625	445,847
VMax W3000	249,523	2,246,451	748,693

Stiffness has a direct influence on soil-TRM interaction. As a basic index property, stiffness does not directly determine the protection against erosion; however, higher stiffness indicates that a rigid TRM promotes runoff below it because the rigid material will not follow an uneven surface (Olschewski, et al., 2012).

A comparison of stiffness results between machine and cross-machine directions obtained from testing is shown in Figure 3-9. Tested TRMs show similar stiffness in machine direction but a broader range of stiffness in cross-machine direction thus influencing the range of overall stiffness. The bigger variation in cross-machine direction is a result of different weave methods and microstructures. Also, each TRM is found to have higher stiffness in the cross-machine direction compared with that of the machine direction, which means TRMs are more rigid in the cross-machine direction. TRMs with a similar structure such as Pyramat Green and Landlok 300 have greater fiber density in the cross-machine direction thus leading to greater stiffness in the cross-machine direction. TRMs with a corrugated structure such as T-RECS and Vmax W3000 have a higher order of magnitude of stiffness in the cross-machine direction because it is more difficult to bend

in the direction perpendicular to corrugated direction. Figure 3-9 shows that VMax W3000 has the highest stiffness value in both machine and cross-machine directions since it has a triple-layer structure. Five TRMs which have similar lattice structure have lower stiffness in both machine and cross-machine directions compared with T-RECS and Vmax W3000 because fibers of T-RECS and Vmax W3000 are stiffer than those of five TRMs with similar woven structures. The stiffer fibers of T-RECS and Vmax W3000 may be attributed to different manufacturing methods and shapes of cross section since fibers of both products have a round shape of cross section while fibers of TRMs such as Pyramat Green have an "X3" shape of cross section.

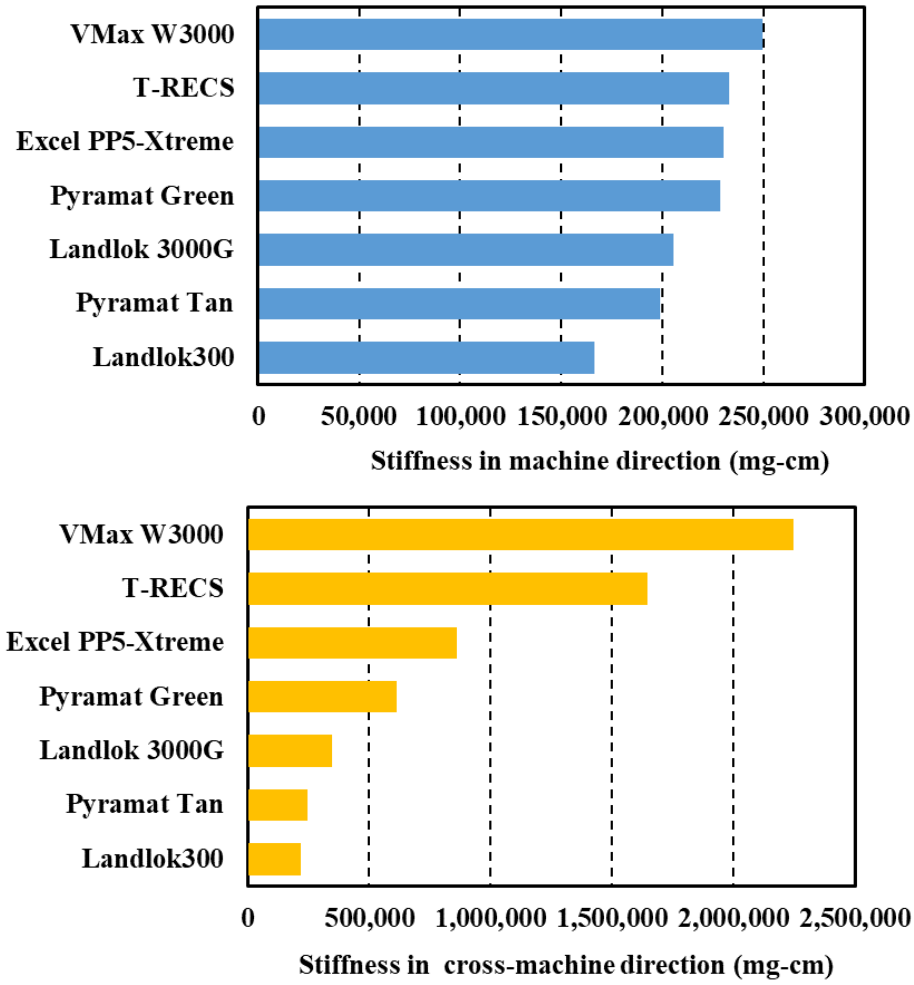

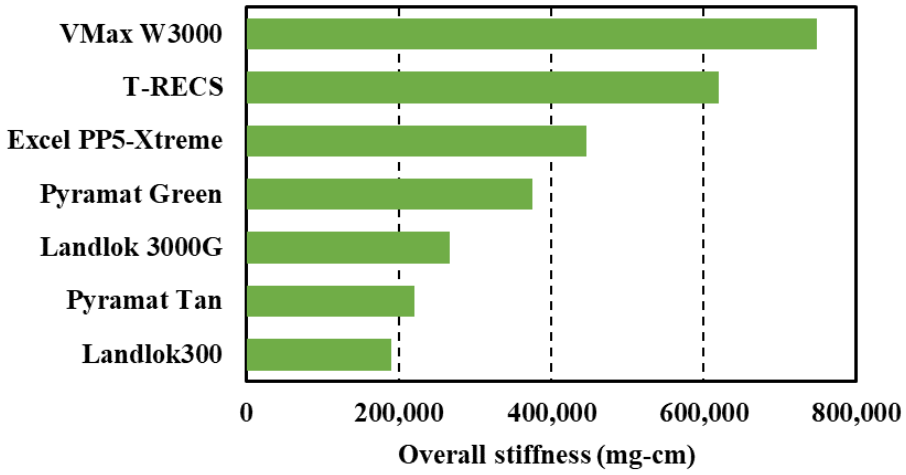

Figure 3-9. Stiffness (flexural rigidity) of the seven turf reinforcement mats.

3.3.3 Behavior of seven TRM under CBR puncture failure load

Table 3.8 shows the maximum force and fiber extension at failure from static puncture tests. A comparison of the average static puncture strength results of the seven TRMs is shown in Figure 3-10. Among the seven TRMs tested, Pyramat Green has the largest puncture strength at failure. VMax W3000 has the longest extension while Excel PP5-Xtreme has the shortest extension. The plots of load versus displacement for each TRM are presented in Figure 3-11~3-17. Table B.2 in the appendix shows photos of specimens after failure. Although these TRM specimens are made of 100% polypropylene, they have different manufacturing methods and material density which can also be represented by measured mass per unit area. TRMs with greater yarn density have more yarns participating in load sharing and energy absorption during the static puncture tests, thus leading to higher puncture resistance.

Table 3.8. Measured Puncture Strength of Seven Turf Reinforcement Mats.

Sample Name	Force (N)	Extension at Failure (mm)
Pyramat Green	6,825	70-80
Pyramat Tan	4,121	50-60
Landlok300	3,620	45-50
Landlok 3000G	4,943	40-55
T-RECS	3,415	35-40
Excel PP5-Xtreme	4,775	33-38
VMax W3000	4,941	105-130

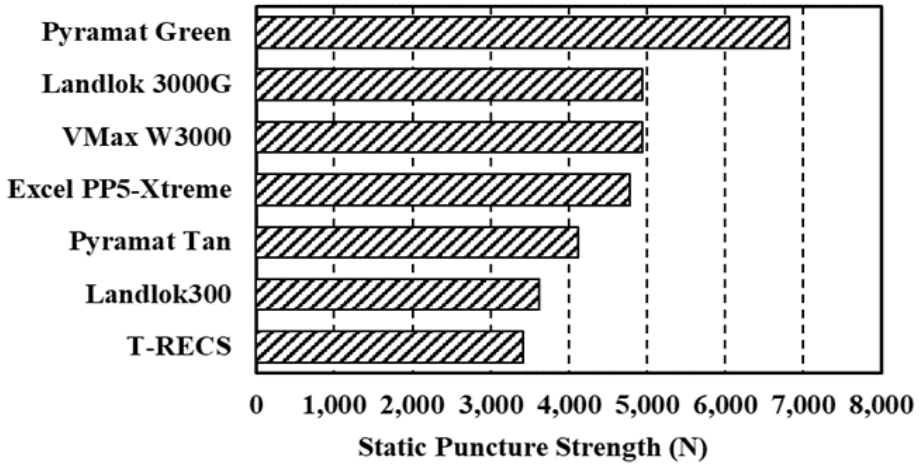

Figure 3-10. Static puncture strength of seven turf reinforcement mats.

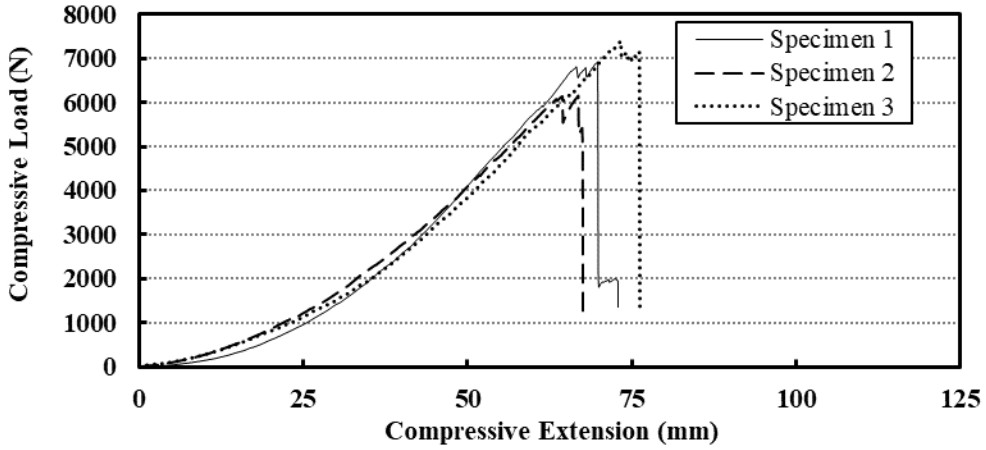

Figure 3-11. Plot of load versus displacement for Pyramat (Green).

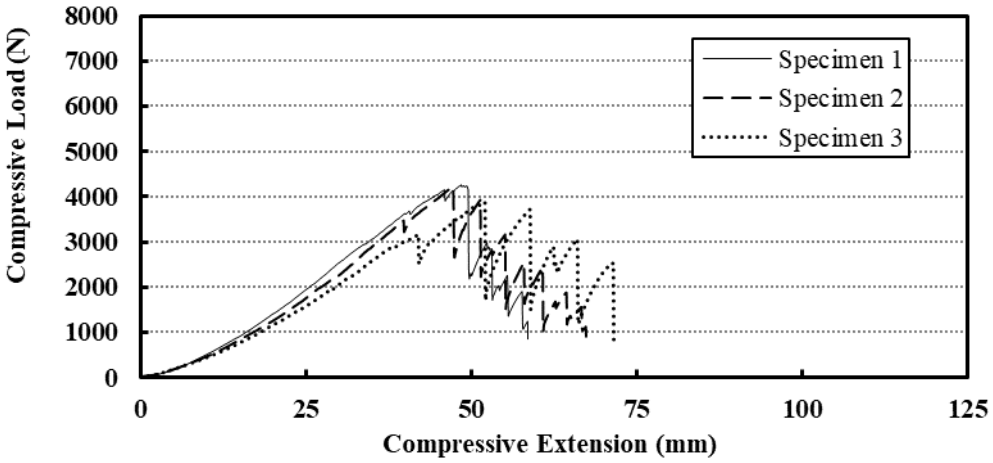

Figure 3-12. Plot of load versus displacement for Pyramat (Tan)

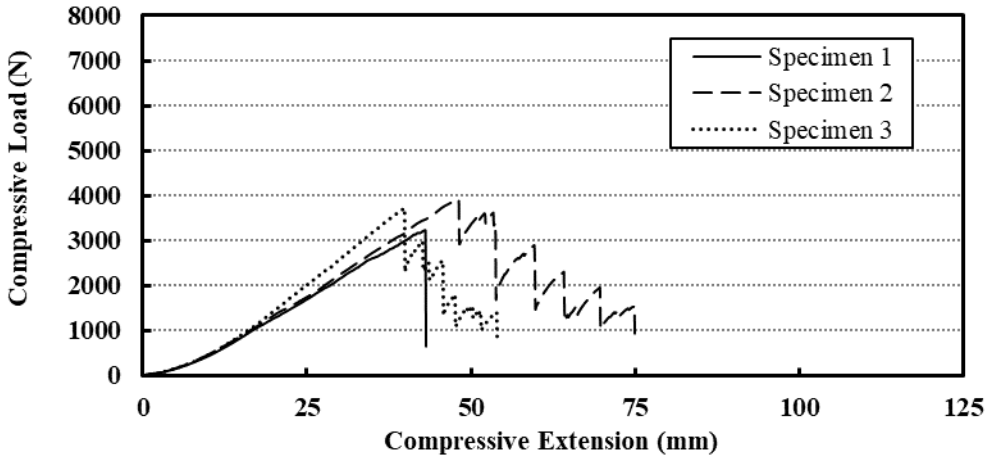

Figure 3-13. Plot of load versus displacement for LANDLOK 300.

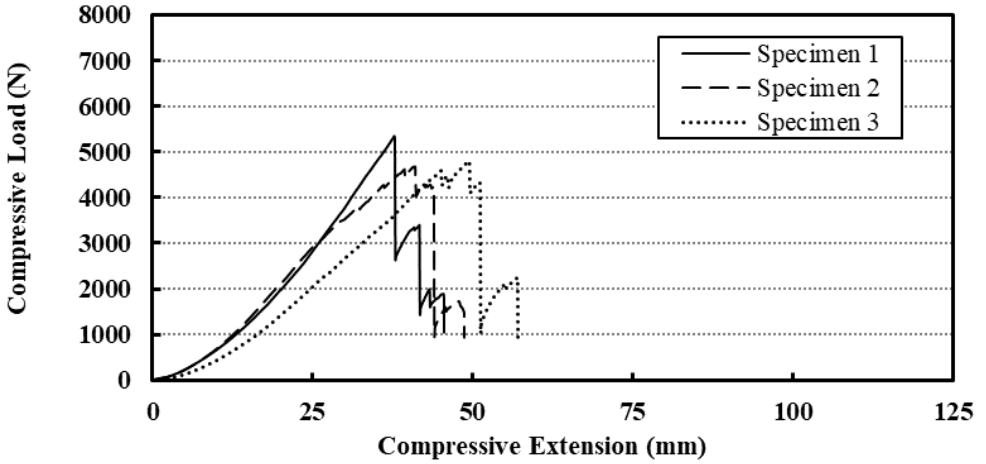

Figure 3-14. Plot of load versus displacement for LANDLOK 3000G.

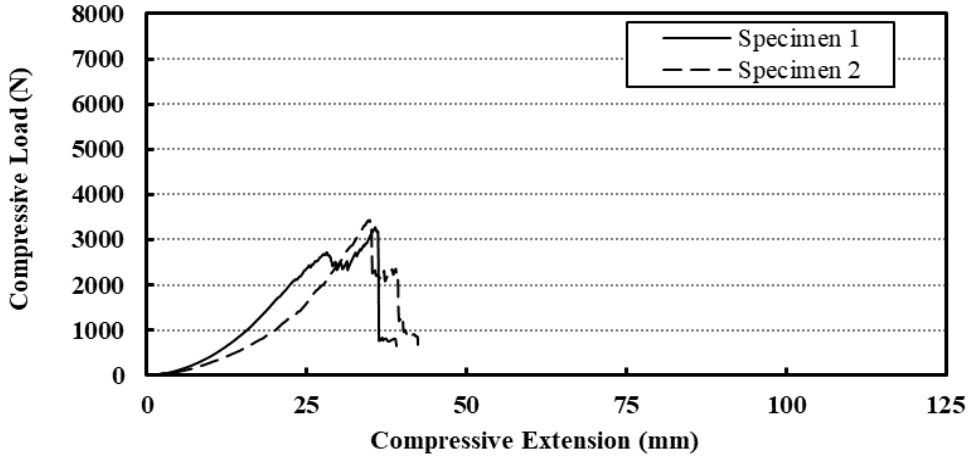

Figure 3-15. Plot of load versus displacement for T-RECS.

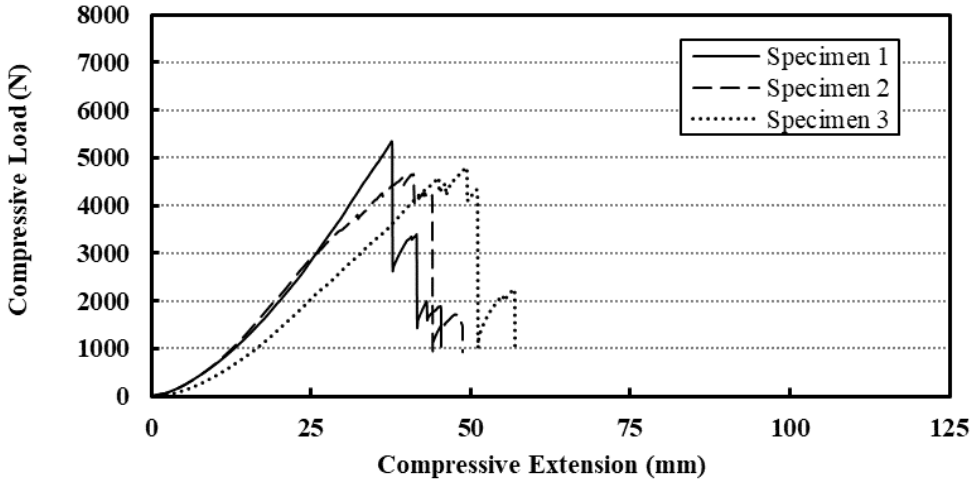

Figure 3-16. Plot of load versus displacement for Excel PP5-Xtreme.

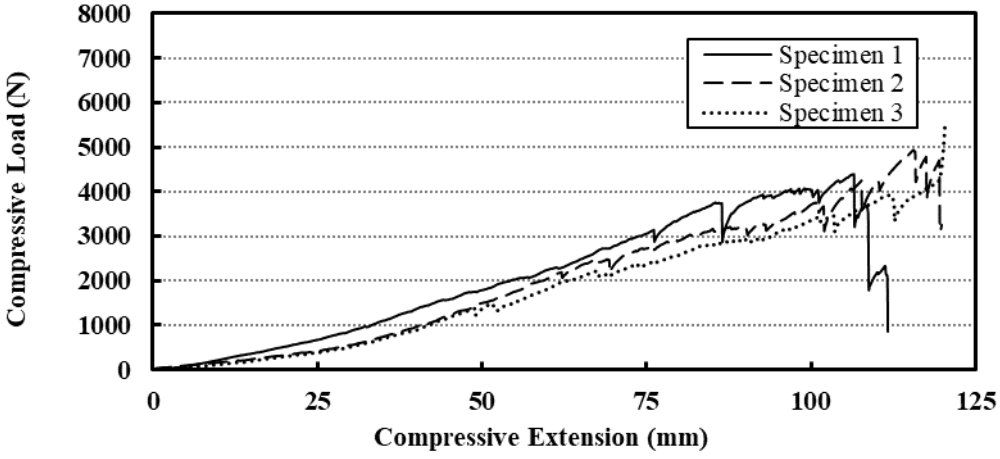

Figure 3-17. Plot of load versus displacement for VMax W3000.

3.3.4 Behavior of seven TRMs under dynamic perforation

Dynamic perforation testing was conducted to provide information on the resistance of the TRMs to penetration by a stainless-steel cone dropped from a fixed height. The degree of penetration is an indication of the behavior of the geosynthetic when sharp objects are dropped on its surface. Figure 3-18 shows specimens after cone penetration.

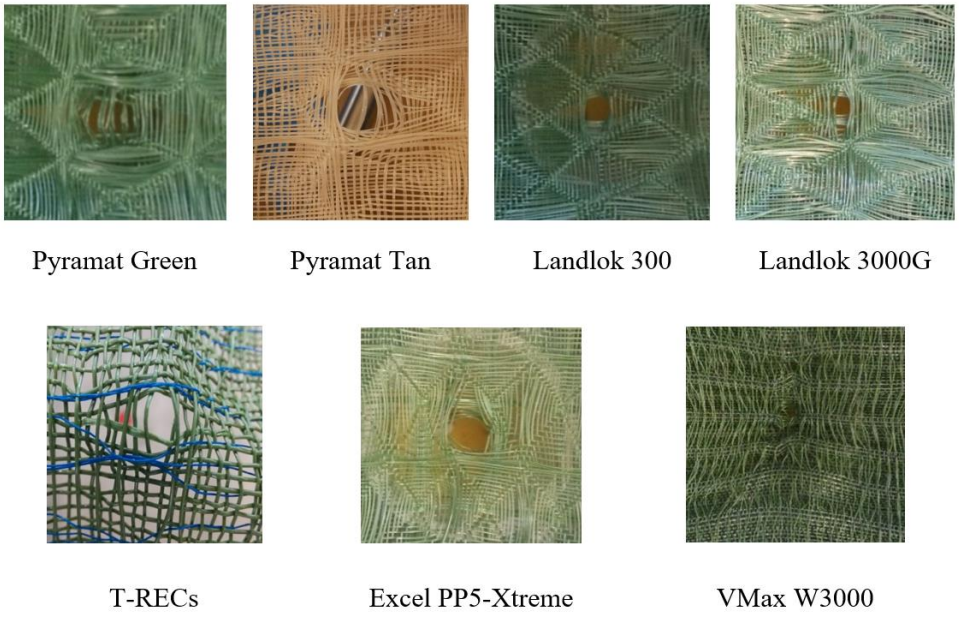

Figure 3-18. Photos of specimens after perforation testing.

Testing results at different locations are summarized in Table 3.9. Five repeated tests were conducted on each location and their values were recorded in Appendix (Table C.1~C.7). Measured hole diameter at each location in Table 3.9 is an average value of the five test results in each case.

Table 3.9. Measured Diameters of Holes Produced by Cone Penetration.

Sample	Location	Measured diameter (mm)
Pyramat Green	Center	9.5
	Middle	12.1
	Bottom	10.5
	Border	9.8
	Top	5.9
	Mean hole diameter	9.5
	Standard deviation	2.0
	COV(%)	21.5
Pyramat Tan	Center	18.3
	Middle, dense side	8.1
	Middle, loose side	15.3
	Bottom, dense side	12.0
	Bottom, loose side	13.6
	Border	13.8
	Top	11.3
	Mean hole diameter	13.2
	Standard deviation	3.0
	COV(%)	22.4
Landlok300	Center	20.5
	Middle	14.8
	Bottom	19.1
	Border	15.3
	Top	10.2
	Mean hole diameter	16.0
	Standard deviation	3.6
	COV(%)	22.6
Landlok 3000G	Center	9.9
	Middle	10.8
	Bottom	13.6
	Border	13.3
	Top	6.5
	Mean hole diameter	10.8
	Standard deviation	2.6
	COV(%)	14.0
T-RECS	Bottom-green	4.0
	Bottom-green&blue mix	7.0
	Top	6.9
	Mean hole diameter	6.0
	Standard deviation	1.4
	COV(%)	22.8
	Center	13.9

Excel PP5-Xtreme	Middle	12.7
	Bottom	13.6
	Border	9.9
	Top	10.1
	Mean hole diameter	12.1
	Standard deviation	1.7
	COV(%)	14.1
VMax W3000	Harder fiber, top side	5.9
	Harder fiber, bottom side	9.0
	Softer fiber, top side	4.1
	Softer fiber, bottom side	8.0
	Mean hole diameter	6.7
	Standard deviation	1.9
	COV(%)	28.1

Figure 3-19 is a comparison of maximum hole size obtained from testing. Landlok 300 has the largest hole diameter, which means it is the weakest material to cone penetration amongst the seven TRMs. Figure 3-20 summarizes hole diameter for five TRMs with similar lattice structure after perforation at different locations. The center is the weakest part for both Pyramat Tan and Landlok300 while the edge of the lattice structure is the strongest part for them. This phenomenon is opposite to expectations prior to the test because it is the densest part of the lattice. It can be explained by the vaulted structure which has a higher bearing capacity than the flat or concave structure. However, this explanation does not seem consistent for VMax W3000, where the average diameter of the hole on the black line is larger than that in the middle location. When comparing the fabrics from the top and bottom side, the fabric from the top side is more elastic than that from the bottom side. So the kinetic energy of the fall cone is absorbed by the top side material when the fabric stretches. Thus, to some extent, the elasticity of material can be more important than fabric structure when designing geosynthetics. Materials possessing higher stiffness

have lower dynamic perforation strengths. Excel PP5-Xtreme is an exception in this analysis but it does not deviate too much in this trend.

Figure 3-22 shows that VMax W3000 has larger deformation than the other six materials. The deformation recovery after failure can be observed by measuring the depth of displacement with time. Landlok300 is the fastest to recover back to as flat as original (in 12 hours) while VMax W3000 is the slowest one (more than 24 hours). This is likely the effect of their elasticity.

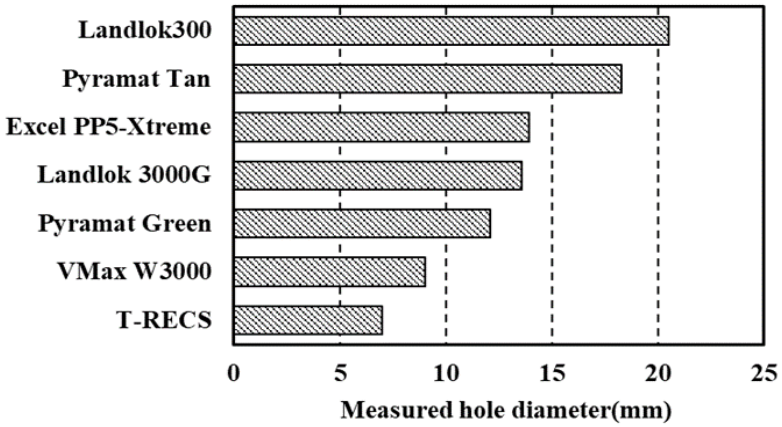

Figure 3-19. Maximum hole diameters for tested specimens.

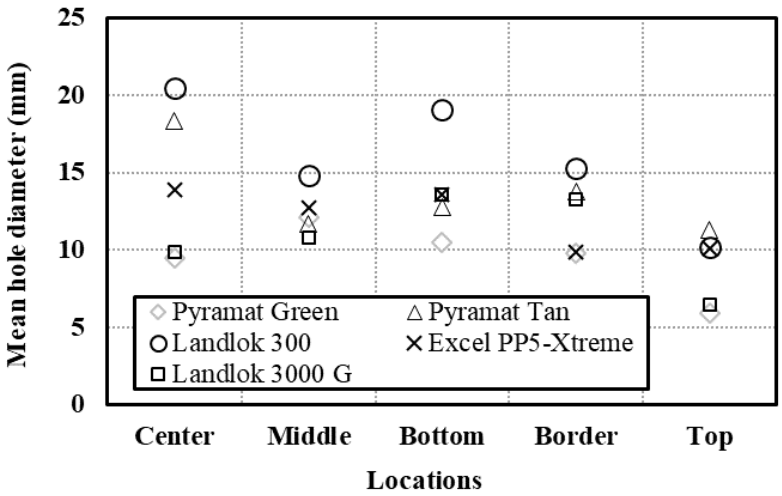

Figure 3-20. Hole size for the five TRMs with lattice structure at different locations.

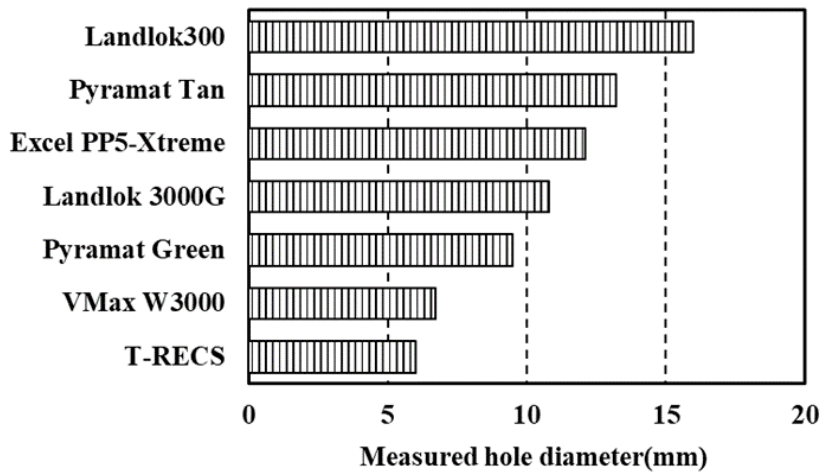

Figure 3-21. Average hole size for the seven TRMs.

Figure 3-22. Deformation of VMax W3000 and Landlok 300 after dynamic penetration.

3.3.5 Long-term flow properties

The magnitude of the measured hydraulic conductivity is a function of the soil type, with the TRMs tested in combination with F75 showing a hydraulic conductivity that is consistent with time at ~$1x10^{-3}$ cm/s. The tests with the Piedmont soil were consistent as a function of time and in the range of 0.5 x 10^{-4} cm/s to $0.5x10^{-5}$ cm/s (shown in Figure 3-23). In six of the seven TRMs tested, the graded sand showed at least one order of magnitude decrease in hydraulic conductivity. Initial hydraulic conductivity values were ~$1x10^{-3}$ cm/s but decreased to ~$1x10^{-5}$ cm/s throughout the duration of testing. The only exception to this was the Excel PP5-Xtreme, which remained constant at ~$1x10^{-3}$ cm/s for the testing duration. These results indicate that for six of the seven TRMs tested, movement of soil particles into the TRM was occurring, and the hydraulic conductivity decreased as the movement of soil particles resulted in a layer with a lower void ratio (or void space). A similar phenomenon was also observed in testing results by Abbaspour et al., 2018. The fluctuation of hydraulic conductivity of flow in graded sands as a function of time is attributed to a clogging and then break-through process. Based on particle size distribution data in APPENDIX D, the particle size of graded sands is greater than that of F75 sand thus it is easier for the graded sand to clog the openings of a TRM compared with F75 sand and Piedmont soil which have finer particle sizes.

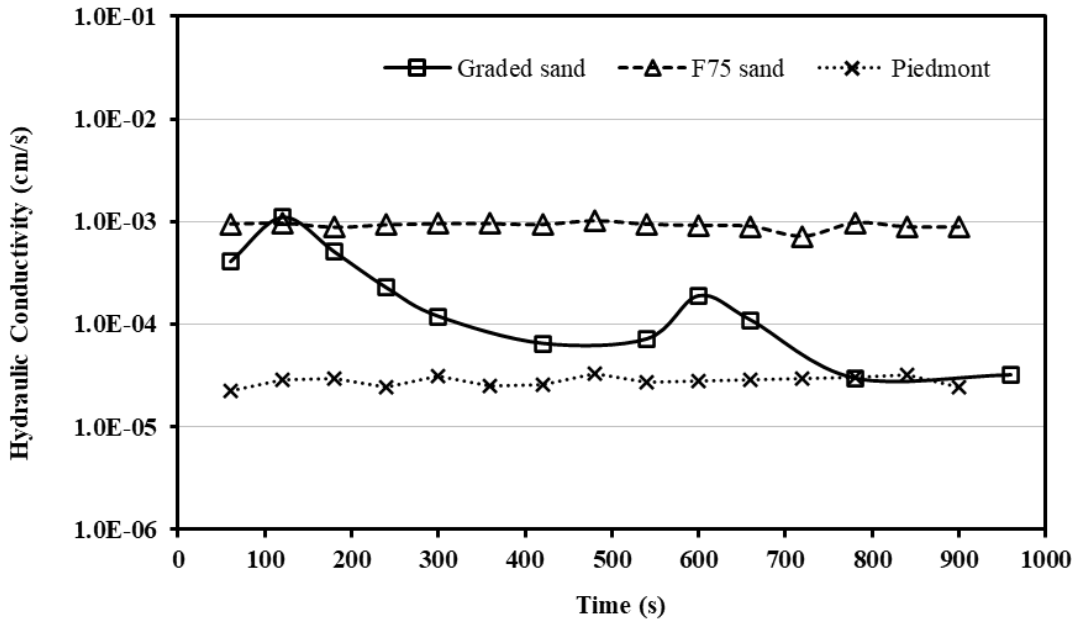

Figure 3-23. Hydraulic conductivity of Pyramat Green in contact with three test soils.

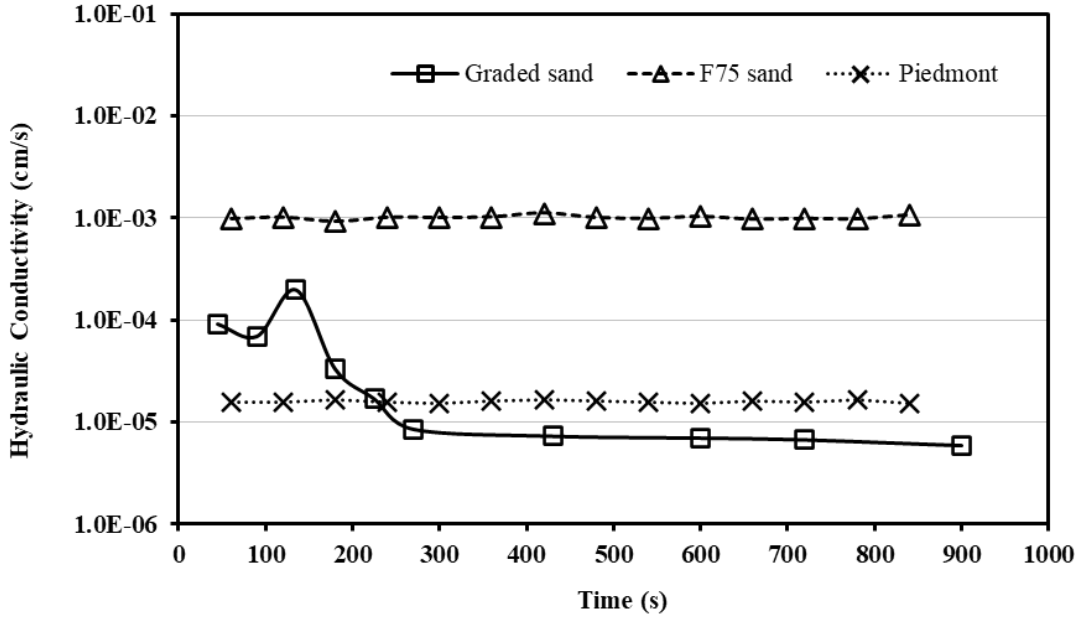

Figure 3-24. Hydraulic conductivity of Pyramat Tan in contact with three test soils.

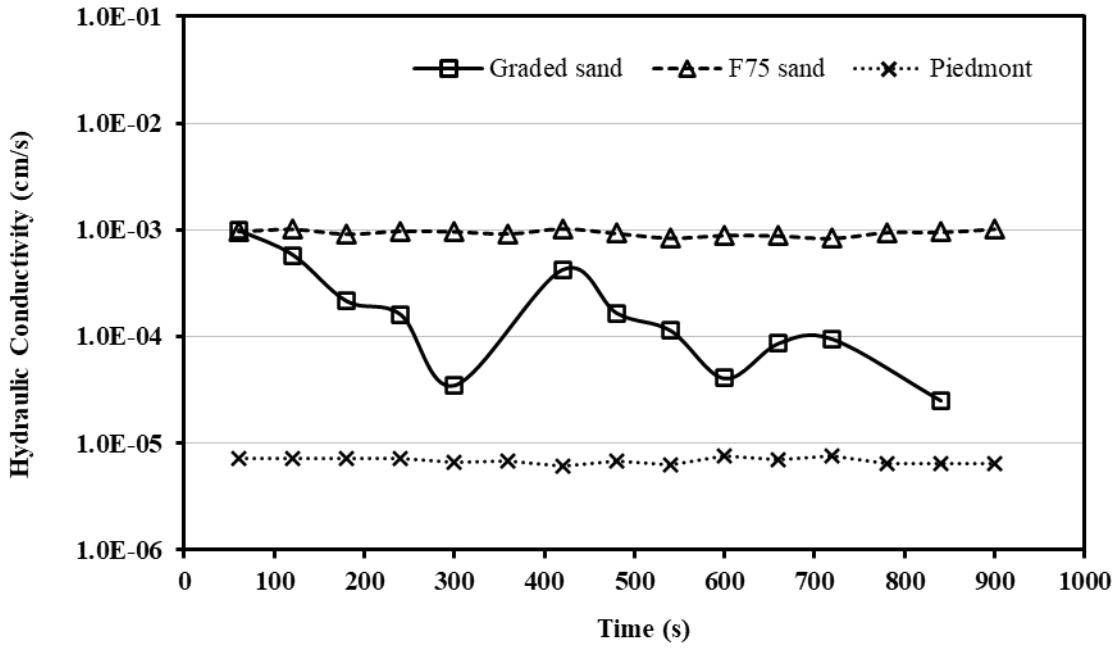

Figure 3-25. Hydraulic conductivity of Landlok 300 in contact with three test soils.

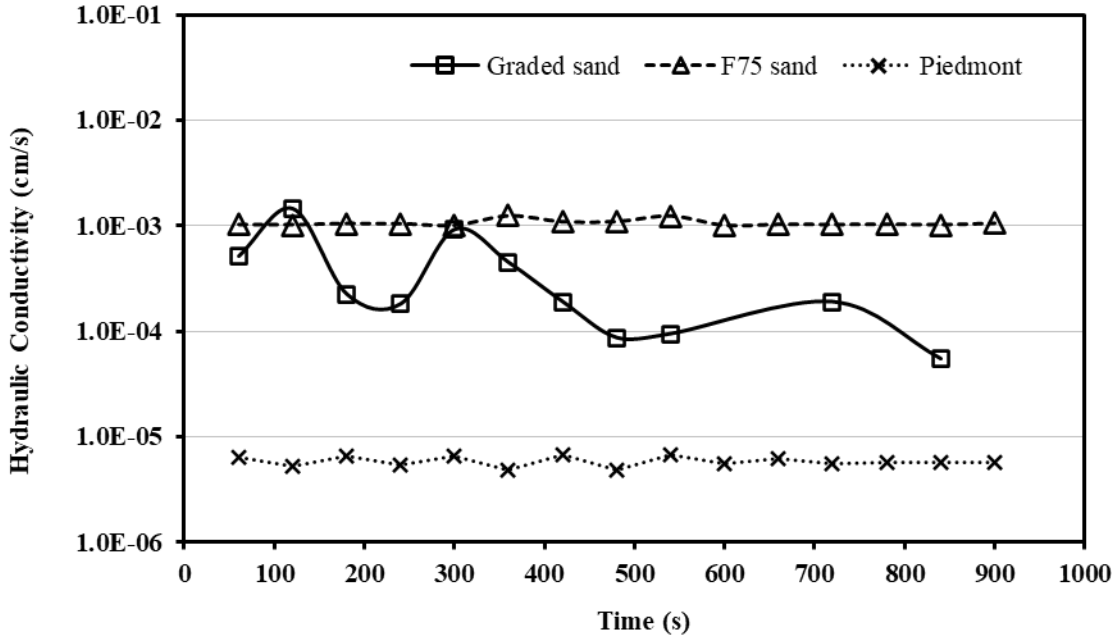

Figure 3-26. Hydraulic conductivity of Landlok 3000G in contact with three test soils.

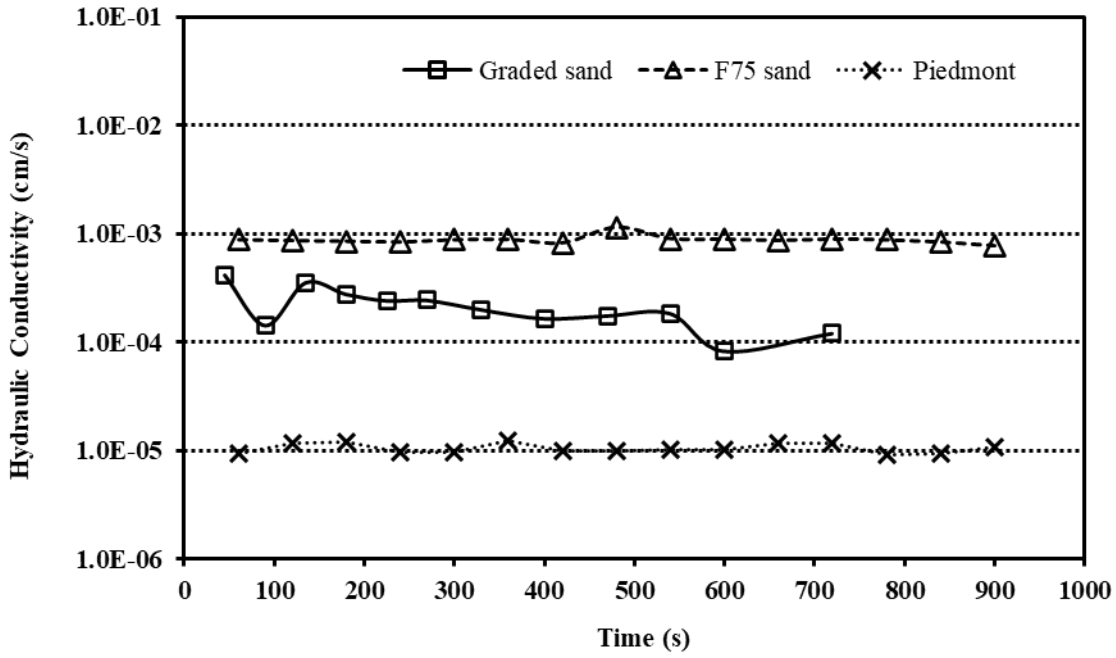

Figure 3-27. Hydraulic conductivity of T-RECS in contact with three test soils.

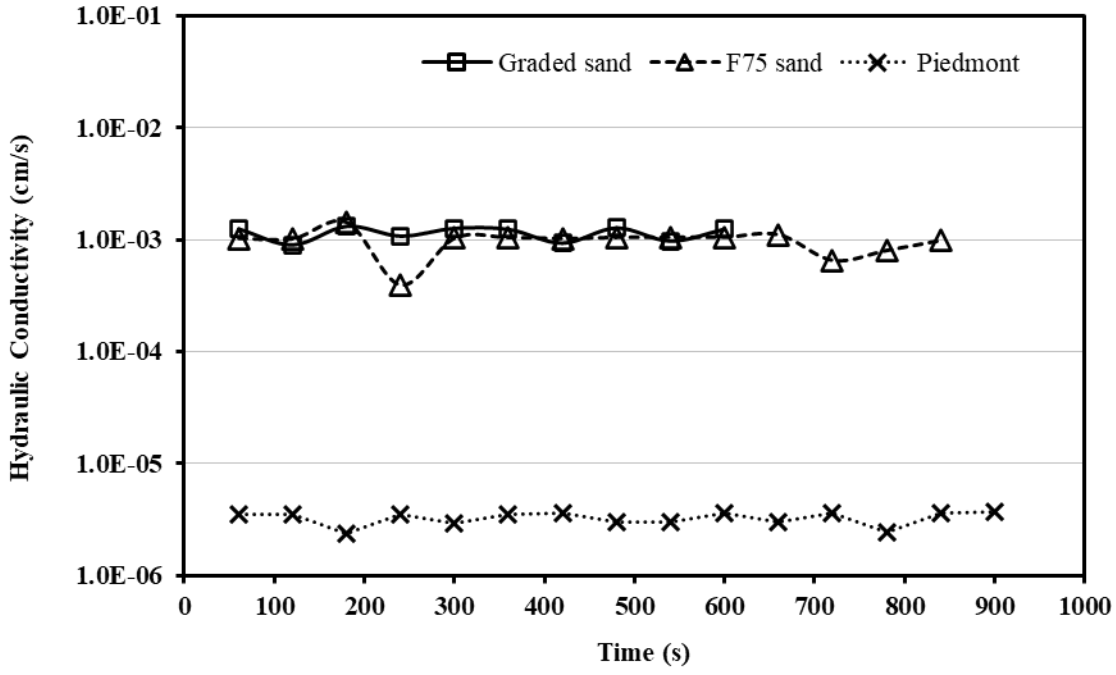

Figure 3-28. Hydraulic conductivity of Excel PP5-Xtreme in contact with three test soils.

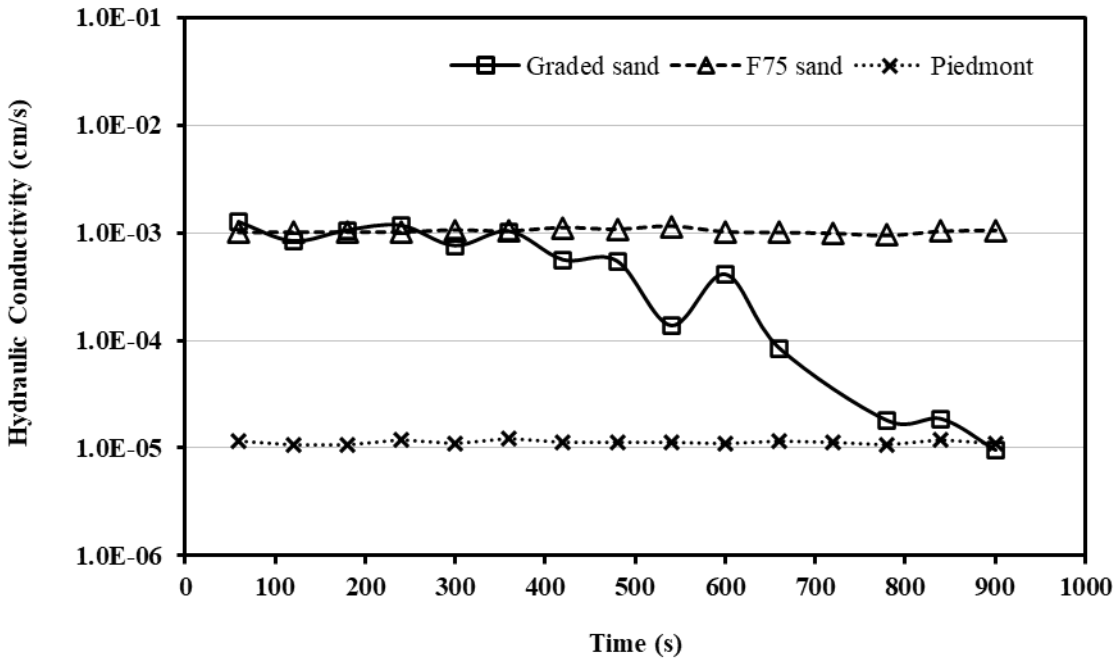

Figure 3-29. Hydraulic conductivity of VMax 3000 in contact with three test soils.

The comparison of measured hydraulic conductivities is shown in Figure 3-30. The hydraulic conductivity is dominated by the type of soil used in the experiment, thus there's no obvious influence of TRMs on hydraulic conductivity.

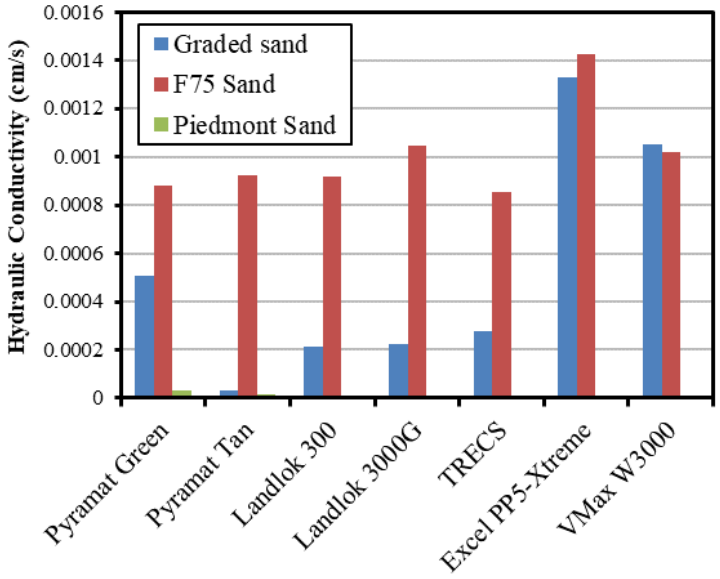

Figure 3-30. Hydraulic conductivities of seven TRMs in contact with three test soils.

It is observed in Figure 3-30 that graded soil specimen with Pyramat Tan have a lower hydraulic conductivity. This may be attributed to the nonuniform opening size of Pyramat Tan. The Pyramat Tan specimen prepared for hydraulic conductivity testing have a smaller opening size and greater yarn density.

3.4 Analysis

Murphy and Koerner (1988) illustrated a linear relationship between tensile strength and puncture force. Subsequently, Nguyen and Vu-Khanh (2004) pointed out that the linear relationship was only applicable to linear elastic deformation. The plots of load versus displacement in Figure 3-11~3-17 display that the TRMs do not deform linearly, thus Murphy and Koerner's conclusion is not applicable based on this study.

The static puncture test uses the same equipment as the CBR test. However, the puncture resistance is a form of tension test to simulate how objects such as sticks or stones can penetrate through a geosynthetic. Figure 3-31 shows that the displacements at puncture failure are related to mass per unit area. As explained in the ASTM Standard D6241, the results indicate the capability of a geosynthetic to resist slow puncture damage during installation and service life. Woven TRMs with greater mass per unit area reflect more yarns within a specific area if it is assumed the material density is the same for a single yarn. The static puncture damage will compress the fabric layer and then shear damage occurs to the yarns of the top surface of fabric while the yarns in the middle and bottom surface extend. TRMs will greater mass per unit area will have more yarns extending before shear damages happen thus leading to greater puncture displacement values.

Figure 3-32 plots the relationship between overall stiffness and mean hole diameter from the dynamic perforation tests. Stiffness decreases when hole diameter increases for all seven TRM materials. Larger hole diameters indicate the material is more vulnerable in dynamic perforation. The plot illustrates that the strength of dynamic perforation is related to the overall stiffness of the TRM. During dynamic perforation, the fibers in the TRM with greater stiffness absorb more energy from the dropped cone and distribute the stresses in the TRM to provide the resistance.

Figure 3-33 compares the stiffness in machine and cross-machine directions. The stiffness value in the cross-machine direction is larger than the value in the machine direction in geometric series, which indicates that TRMs are anisotropic materials. The regression of correlation between stiffnesses in machine and cross-machine directions reflects the different yarn density of TRM in both directions.

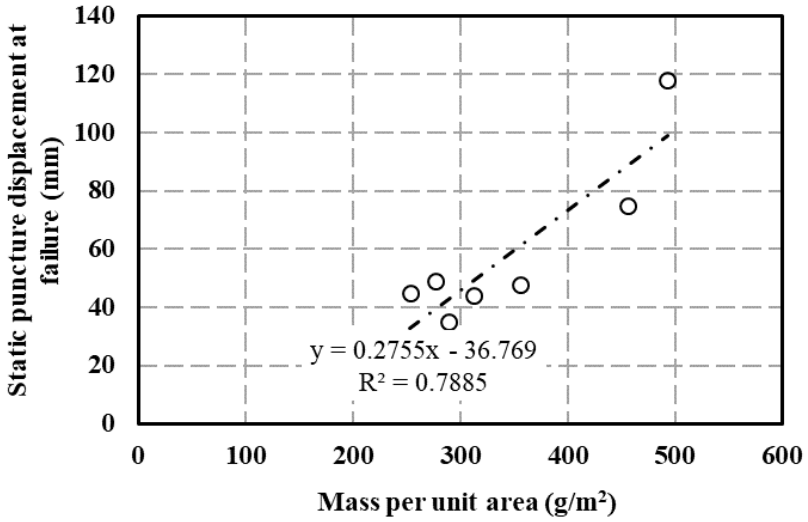

Figure 3-31. Correlation of displacement at failure and mass per unit area.

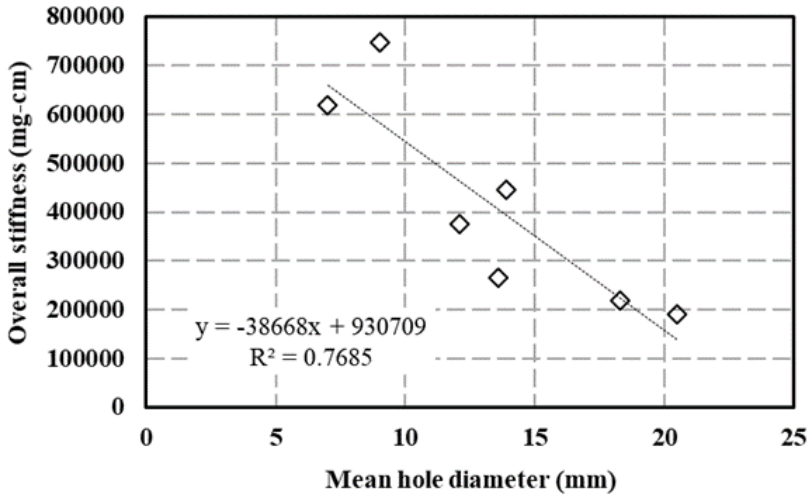

Figure 3-32. Stiffness and mean hole diameter of dynamic perforation.

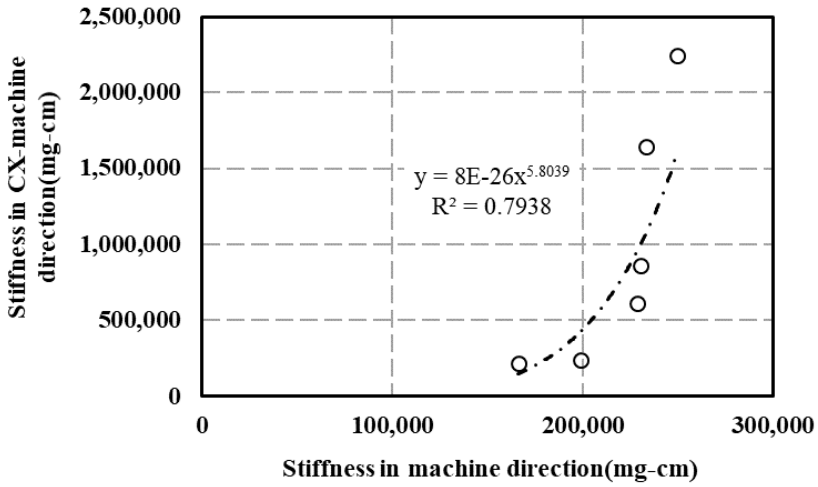

Figure 3-33. Comparison of stiffness in cross-machine and machine directions.

Figure 3-34 and 3-35 illustrates the two factors influence the static puncture strength in woven and non-woven fabrics. Both figures indicate that static puncture strength increases with increased mass per unit area and tensile strength. Other factors such as elasticity of yarn and stiffness can also be related to static puncture strength. However, among the mentioned factors, how much each of them dominates the static puncture has not been discussed in previous studies and challenges exist due to limited testing. Figure

3-36 indicates a positive correlation between tensile strength and mass per unit area for both TRMs and HPTRMs.

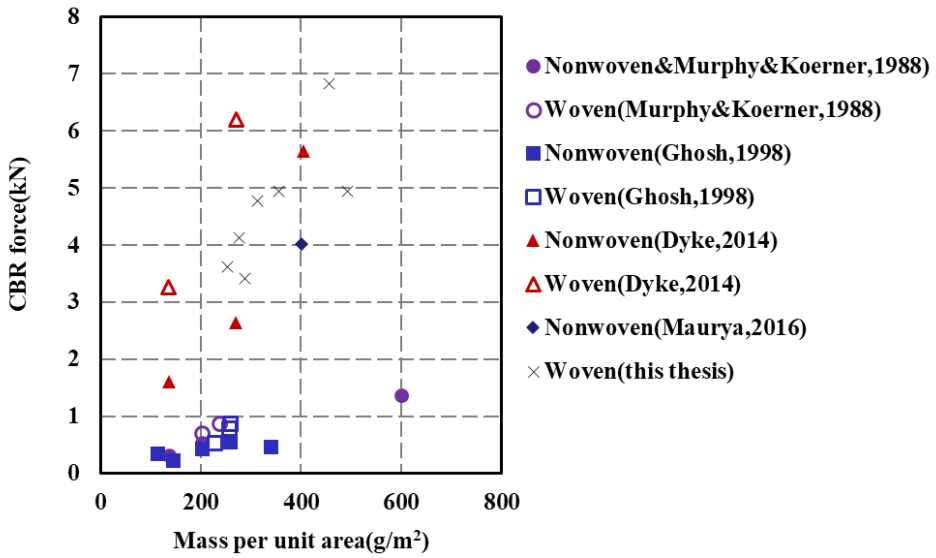

Figure 3-34. Correlation between static puncture force and mass per unit area.

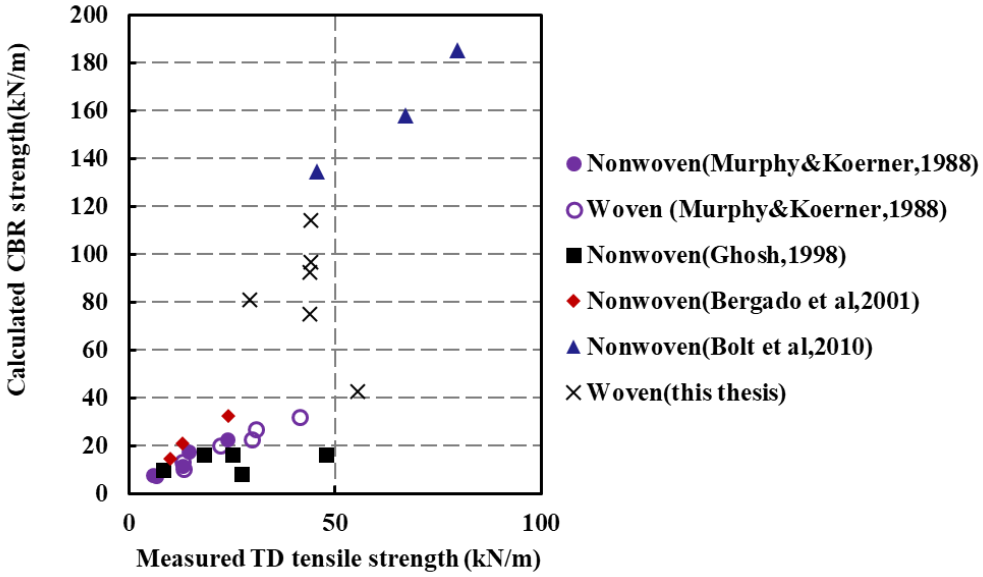

Figure 3-35. Correlation between static puncture strength and tensile strength in the cross-machine direction.

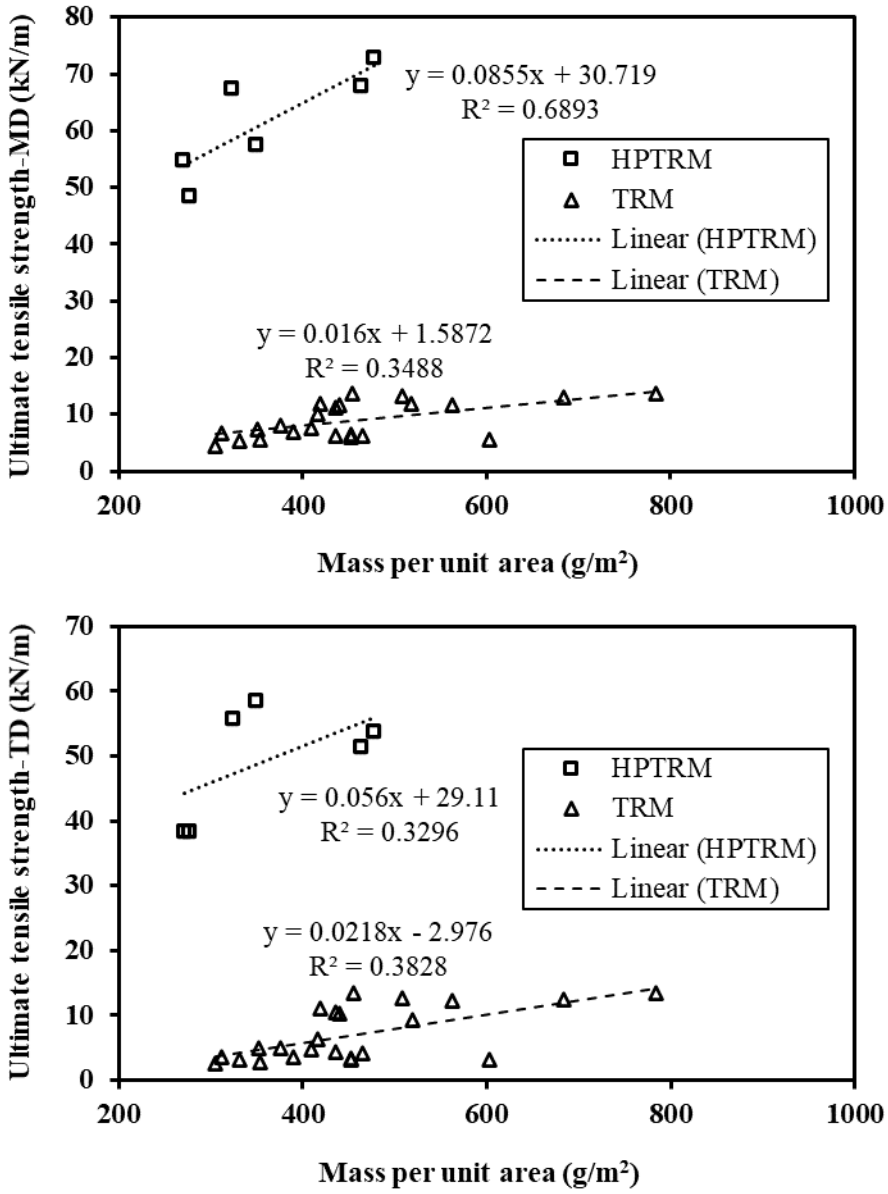

Figure 3-36. Correlation between tensile strengths in the machine and cross-machine directions and mass per unit area (data collected from NTPEP).

Figure 3-37 shows a linear relationship between tensile strengths in the machine and cross-machine directions. This is reasonable because tensile strength is dependent on the number of yarns in the machine and cross-machine directions. There is no clear relationship between puncture resistance and stiffnesses as shown in Figure 3-38. Stiffness is a function of two parameters: mass per unit area and length of overhang as indicated in

Equation 8. Figure 3-38 actually plots the correlation between puncture resistance and cubic length of the overhang since the gap of mass per unit area of TRMs is not obvious. Also, puncture strength reflects the tensile strength of fabric in all directions while the measurement of stiffness is only in a single direction of a fabric.

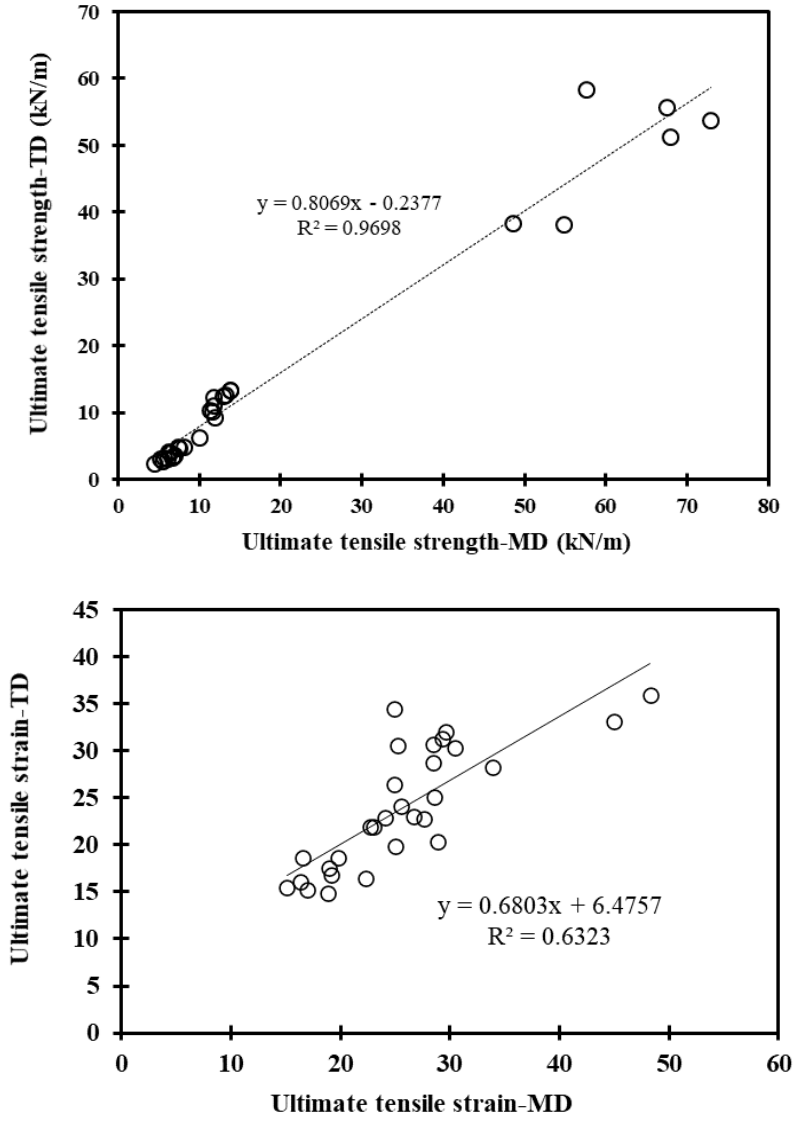

Figure 3-37. Correlation between tensile strength/strain in the machine and cross-machine direction. All tensile strength data collected from NTPEP.

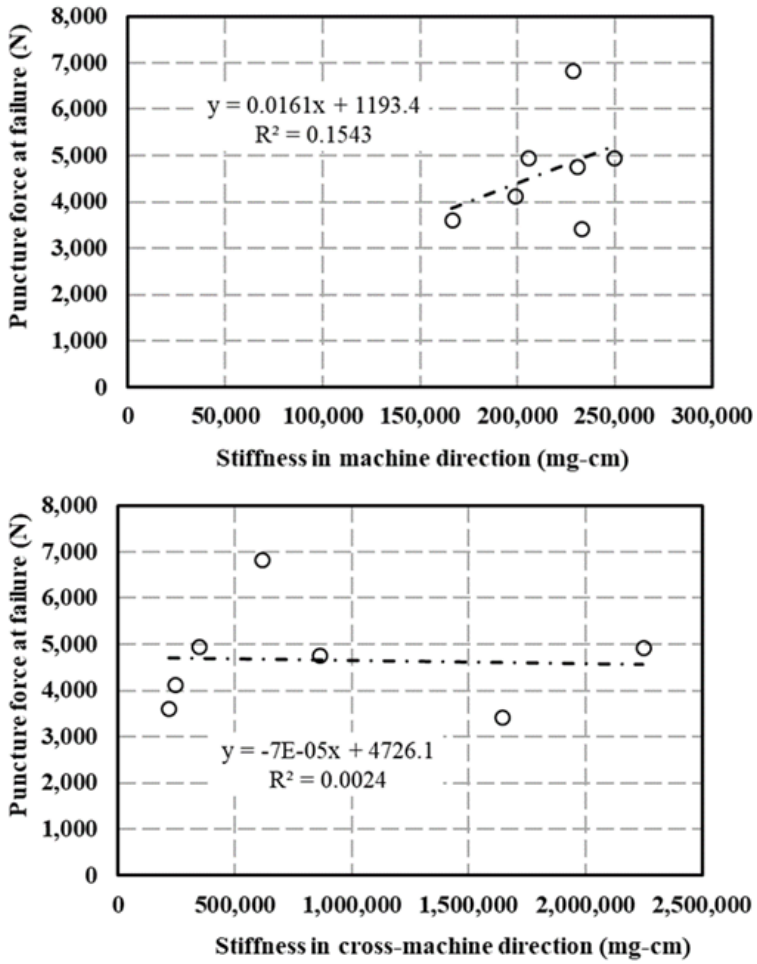

Figure 3-38. Correlation between static puncture force at failure and stiffness in the machine and cross-machine directions.

3.5 Conclusions

The current increasing use of (high performance) turf reinforcement mats stimulates the study of their performance. This chapter has evaluated the physical and mechanical performance of seven turf reinforcement mats (TRMs). The objective of this research was to correlate the index properties and static/dynamic puncture strength. The following conclusions are made:

1. Static puncture strength and tensile strength are linearly correlated with mass per unit area of both woven and nonwoven geosynthetics.

2. However, static puncture strength has no clear correlation with stiffness in both machine and cross-machine direction for seven HPTRMs.

3. Woven TRMs showed anisotropy of stiffness in the machine and cross-machine direction but there's no clear anisotropy of tensile strength.

4. The tensile strength of high-performance turf reinforcement mats (HPTRMs) is between 45~65 kN/m while the tensile strength of turf reinforcement mats (TRMs) is between 0~20 kN/m.

5. It is not clear how factors such as stiffness, the elasticity of yarn, thickness, woven types, and interlacement pattern influence the puncture strength of woven fabrics.

6. HPTRMs differ from TRMs mainly in tensile strength and shear resistances to flow erosion. Other properties such as mass per unit area, thickness, light penetration, and UV resistance are not ideal indices to distinguish HPTRMs and TRMs, or other RECPs.

CHAPTER 4. ROOT INTERACTION WITH TRM MATERIALS

4.1 Introduction

Conventional soil loss treatment can yield a significant improvement in the primitive stage while also causing negative effects such as preventing water transition in soil and recovery of original natural vegetation. Using vegetation to treat soil erosion problem has been widely demonstrated in many case histories. Root systems of vegetation play an important role in soil erosion control because they modify the physical properties of soil around the roots, which include infiltration capacity, aggregate stability, soil bulk density, texture, and chemical contents (Gyssels et al., 2005).

4.1.1 Tensile and Pullout Characteristics of Plant Roots

Vegetation plays an essential role in erosion control because it reduces the risk of slope failure and channel erosion (Morgan and Rickson, 2003). Factors that influence erosion control effects of plant roots include the amount of roots within the soil matrix, root architecture, root diameter, tensile strength, and root depth (Vannoppen et al., 2015). Thus, it is important to consider plants, soil, and other covering products as an integral system to provide the function of slope stability and erosion control.

Plant roots mechanically improve soil aggregate stability by rearranging finer soil particles into larger aggregates with root secretions (Amezketa, 1999). Also, plant roots push aside soil particles adjacent and penetrate pore space of soil, which potentially improve soil infiltration capacity and hydraulic conductivity by decreasing the soil density and increasing soil porosity (Glinski, 2018; Gyssels et al., 2005).

Multiple studies on soil reinforcement by plant roots can be categorized into root fiber mechanics and integral performance of organisms between soil and roots (Cheng et al., 2003). Research on root mechanics such as tensile and shear resistance of root-soil system is more prevalent. When plant roots are pulled out, they need to overcome the friction between root surface and soil particles. If the ultimate tensile force of roots is greater than friction between root surface and soil particles, roots will be pulled out, otherwise, roots will break.

Tensile failure modes of grass roots during pull-out testing can be divided as (1) both main root and lateral roots are pulled out; (2) main root is pulled out but lateral roots are broken; (3) main root is broken but lateral roots are pulled out; (4) both main root and lateral roots are broken. In mode 1, stresses in main root and lateral roots are less than ultimate tensile strengths. In mode 2, the stress in main root is less than ultimate tensile strength while stresses in lateral roots reach their ultimate tensile strengths. In mode 3, stress in main root reaches its ultimate tensile strength while stresses in the lateral roots have not reached their ultimate tensile strength. In mode 4, stresses in main root and lateral roots reach their ultimate tensile strengths.

Compared with roots of shrubs and trees, grasses have much thinner root diameters, which are normally less than 1*mm* (Wang, 2010). Root tensile resistance of grasses is weak for a single root; however, total grass root resistance more relies on the root network rather than the strength of a single root. Table 4.1 summarizes laboratory tested root tensile strength of different grass species. Figure 4-1 and Figure 4-2 plots the tensile force and tensile strength with corresponding root diameter. The figure indicates that larger forces are needed to break roots with a larger diameter, however, roots with larger diameter show

decreasing tensile strengths. Similar traits are also presented for tree and shrub roots (Tosi, 2007; Genet et al., 2005). Some researchers also studied how root moisture content affected root tensile strength and concluded that root tensile strength decreased linearly with increasing root moisture content (Zhang et al., 2019). Other researchers work on explaining why finer roots have higher tensile strength than thicker roots. The primary conclusion identifies that the amount of lignin and cellulose as well as plant age influences the mechanical properties of roots (Loades et al., 2015; Zhang et al., 2014). Meanwhile, root reinforcement models and algorithms developed to predict the soil shear strength improvement by roots are also studied. Wu and Waldron Model (Waldron and Dakessian, 1981; Wu et al., 1979, Waldron, 1977) and the fiber bundle model (Pollen and Simon, 2005) are two widely used models (Ji et al., 2020). Both models considered root quality, which is normally represented by root tensile strength, and quantity, which is expressed by root area ratio (RAR) (Waldron 1977; Wu 1976).

Table 4.1. Laboratory tensile testing on single grass roots.

Grass species	Root diameter, D (mm)	Ultimate tensile force, T_u(N)	References
Vetiver grass	0.25~2.9	2.3~33.8	Teerawattanasuk, Chairat, et al., 2014
	0.2~1.7	6~53	Cheng et al., 2003
Ruzi grass	0.3~0.7	2.0~7.2	Teerawattanasuk, Chairat, et al., 2014
Phleum pratense	0.17~0.83	0.5~8.3	Rauchecker et al., 2019
Heteropappus altaicus	0.15~2.19	1~76	Zhang et al., 2019
Poa sphondylodes	0.06~0.22	0.6~3,1	Zhang et al.., 2019
Ryegrass	0.18~0.5	2.99~9.01	Wang, 2010
Tall fascue	0.16~0.46	2.26~10.51	Wang, 2010
Poa	0.14~0.41	1.63~7.51	Wang, 2010
Bermuda grass	0.78~1.21	7.8~18.1	Cheng et al., 2003

	0.14~0.41	0.15~1.63	Wang, 2010
Manila grass	0.65~0.9	6.9~10.8	Cheng et al., 2003
Dallis grass	0.8~1.05	12.3~13.2	Cheng et al., 2003
White clover	0.8~1.2	13.7~20.6	Cheng et al., 2003
Bahia grass	0.6~0.84	6.9~12.0	Cheng et al., 2003
Centipedegrass	0.6~0.75	7.8~11.8	Cheng et al., 2003
Late Juncellus	0.29~0.43	1.5~3.1	Cheng et al., 2003

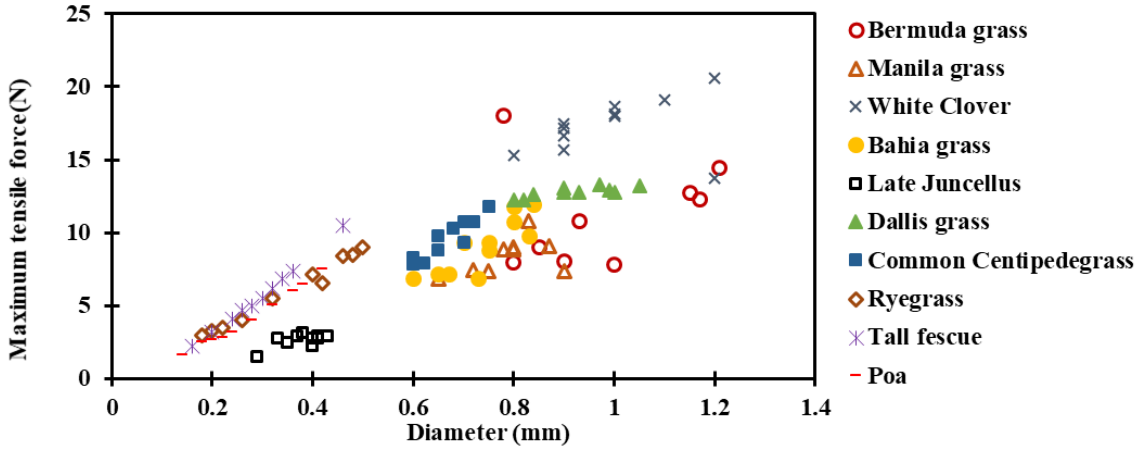

Figure 4-1. Measured maximum tensile force with corresponding root diameter (Wang, 2010; Cheng et al., 2003)

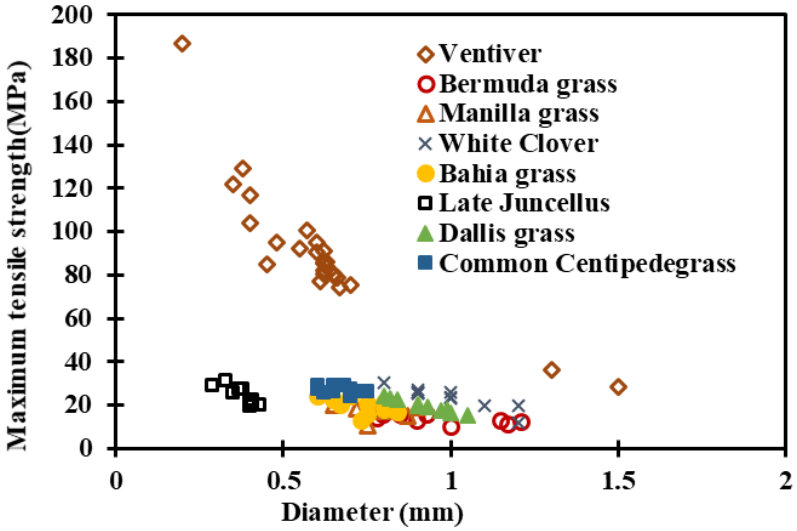

Figure 4-2. Measured maximum tensile strength with corresponding root diameter (Cheng et al., 2003)

Wang's research investigated the relationship between soil water content and shear strength, the tensile force of a single root fiber, and pull-out resistance of a single plant. Wang (2010) indicated that the pullout resistance of a single plant increased with an increasing number of roots (Figure 4-3). He also concluded that pull-out resistance of individual plant roots was not clearly related to the height of the plant while the maximum tensile force of a single root fiber represented an exponential relationship with root diameter and a linear duality relationship with root depth. However, after replotting Wang (2010) and Cheng et al (2005), a power-law function represents a better fitting than an exponential function in estimating the relationship between the maximum tensile force of a single root fiber with root diameter for Bermuda grass (Figure 4-4). Although the specific equation was not proposed, many scholars preferred to express the tensile force-diameter relationship by means of power law (Vergani et al, 2012; Genet et al, 2011; Hales et al, 2009; Tosi, 2007; Norris, 2005, Schmidt et al, 2001).

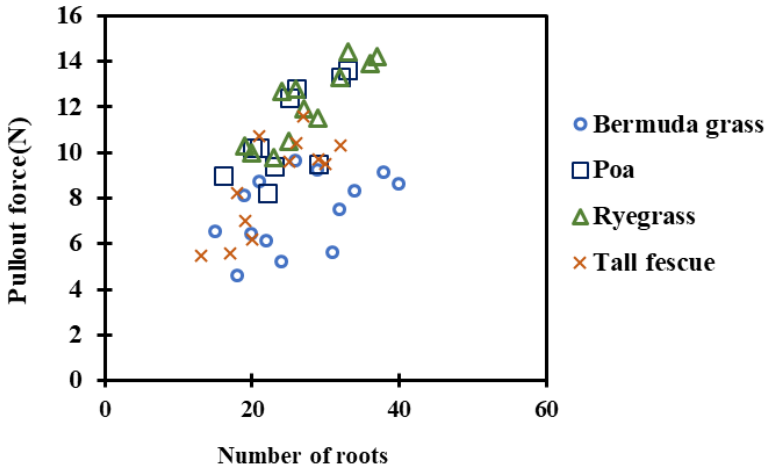

Figure 4-3. Measured pullout force with a corresponding number of roots (after Wang, 2010)

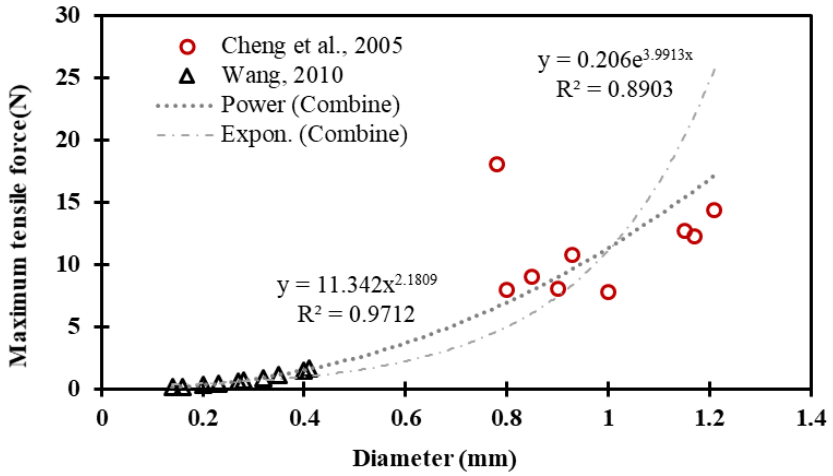

Figure 4-4. Relationship between measured maximum tensile force and root diameter for Bermuda grass (Cynodon Dactylon).

Since directly measuring the tensile strength or force of a single root fiber estimates the breaking failure of root, monitoring root pullout force is a method to evaluate the bonding strength of root and soil systems. Early studies on pullout forces of individual leek roots were performed by Ennos (1990). Ennos concluded that pullout resistance of a plant is influenced by the spatial distribution of its root system, the amount of root fibers of the plant, and the ultimate tensile strength of a single root. Ennos also proposed an equation for pullout forces, which is expressed as

$$F_P = S \cdot L \cdot 2\pi r \tag{10}$$

where F_P is the pullout force (N) of a root, S is soil shear strength (kPa), r is the radius of the root (m) and L is the length of the root (m).

4.1.2 Research problems

Previous studies mainly focused on how vegetation roots or geosynthetics, such as Geogrids and Geocell (Figure 4-5), prevent soil loss in water and wind erosion, however,

limited studies have been conducted on how root interacting with geosynthetics to improve soil reinforcement and erosion control. Also, there is limited research of pull-out tests on grass roots compared with research on tree roots. This study will discuss pull-out resistance of grass roots by conducting pull-out test on plant roots with turf reinforcement mats coverage.

Geogrid wrapped slope surface | **Geocell wrapped slope surface** | **TRM protected slope surface**

Figure 4-5. Soil surface protection using geosynthetics (after Han et al., 2015; NTPEP report of ECP-2, 2016)

4.2 Root Interaction with TRM Materials

4.2.1 Plant selection

In this study, Dandelion (*Taraxacum Officinale*) and Ryegrass (*Lolium perenne L.*) were selected for growth and pullout testing because they have different root types: Dandelion has taproots while Ryegrass has a fibrous root. By definition, a fibrous root plant has many fine equivalent roots while a tap root plant has a main central root with a limited numbers of lateral roots (Cannon, 1949; Langer, 1990). Also, ease of growth and the existence of published pullout data were also considered when selecting plant species for pullout experiments.

"Dandelion is widely grown in moderate regions around the world with moist soils. It grows from generally unbranched taproots and produces one to more than ten stems that are typically 5–40 cm (2.0–15.7 in) tall" (USDA, 2015). Studies on germination indicate that seeds of Dandelion do not have a dormant period in their life cycle and they generally germinate when the temperature is 15~20°C (Hoya et al., 2004). They also mentioned that light intensity does not have an obvious influence on seed germination, however, soil thickness of 5~10 mm above seeds promotes the growth of Dandelion seedling (Ye et al., 2013; Ning et al., 2013).

Ryegrass a most common weed, which possesses a reddish base and narrow, hairless leaves (Golzarian and Frick, 2011). The temperature has an identical influence on leaf growth and the general time length from germination to reproduction is 96 days in the field (Lan et al., 2003). Figure 4-6 shows a lab-grown ryegrass and dandelion.

All plants were grown in transparent soil containers which have a diameter of 9 cm and a depth of 12.5 cm within the Sustainable Geotechnical Systems Laboratory. Transparent soil containers were used for storing Ottawa F75 sand. Considering poor light conditions in the lab, the total growth period of most Dandelion and Ryegrass was within one month before pullout test on young plants.

The tested cases include single and multi-plants that have grown with coverage of Excel PP5-Xtreme, T-RECS, VMax W3000 on the soil surface, and a comparison specimen without TRM coverage. For each case, two repeated specimens were also prepared.

Figure 4-6. Photo of lab-grown ryegrass and dandelion.

4.2.2 Plant growth with TRM coverage

Due to the limitation of time and lab conditions, pull-out tests were performed after one month's growth of both plants.

Before starting the pull-out tests, the evaporation rates of F-75 sand with the cover of the six materials on the top of the soil were measured, and the relationship between evaporation rate and light penetration is plotted in Figure 4-7. Light penetration with seed germination performance (ASTM D 7322) of TRMs was also plotted (Figure 4-8). There is no clear relationship between seed germination enhancement and light penetration.

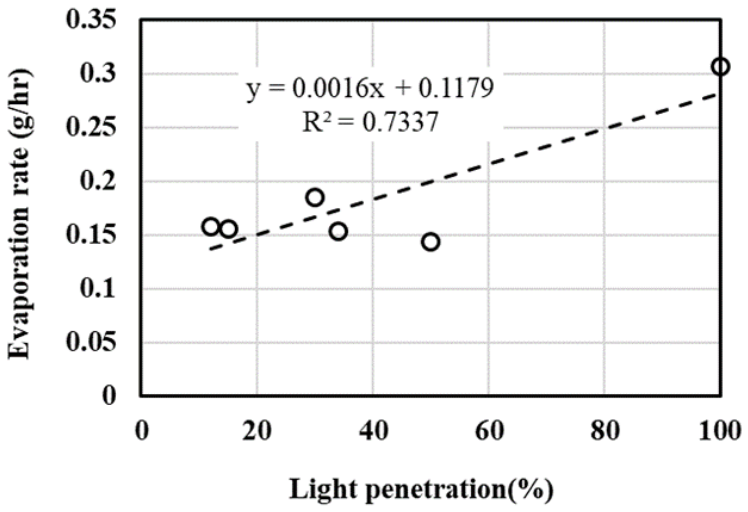

Figure 4-7. Relationship between evaporation rate and light penetration value of six TRMs (Pyramat Green is disregarded because of the lack of data, light penetration data is obtained from NTPEP report).

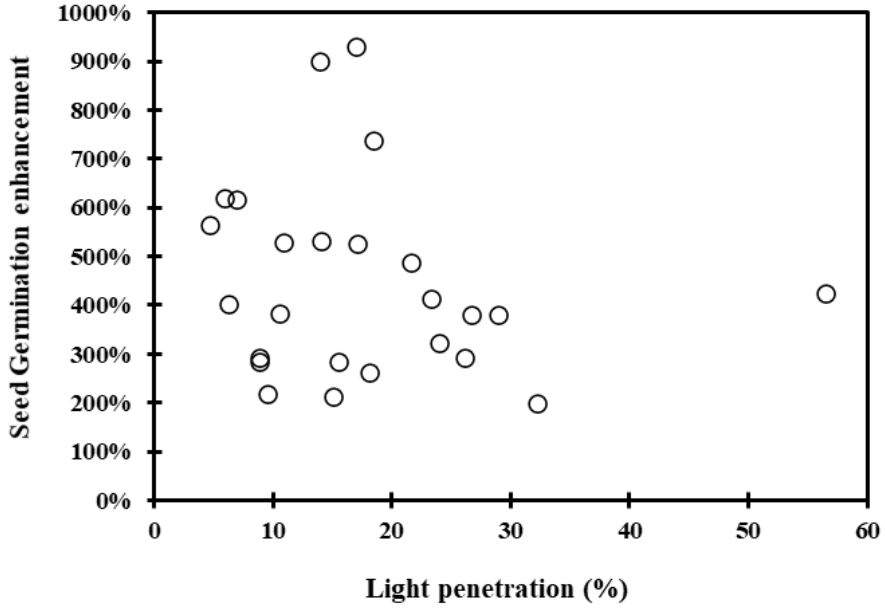

Figure 4-8. Plot of Seed germination enhancement and light penetration of TRMs (data obtained from NTPEP report).

The evaporation rate with and without coverage of the TRM materials is measured and presented in Figure 4-9. At the beginning of the test, seven empty containers were prepared and the same amount of water was added. TRMs were placed on top of six of the

containers and the remaining one container without coverage of TRMs was used as a blank-control specimen. During the test, the loss of water with time was monitored and recorded. The evaporation was calculated by loss of water weight with time.

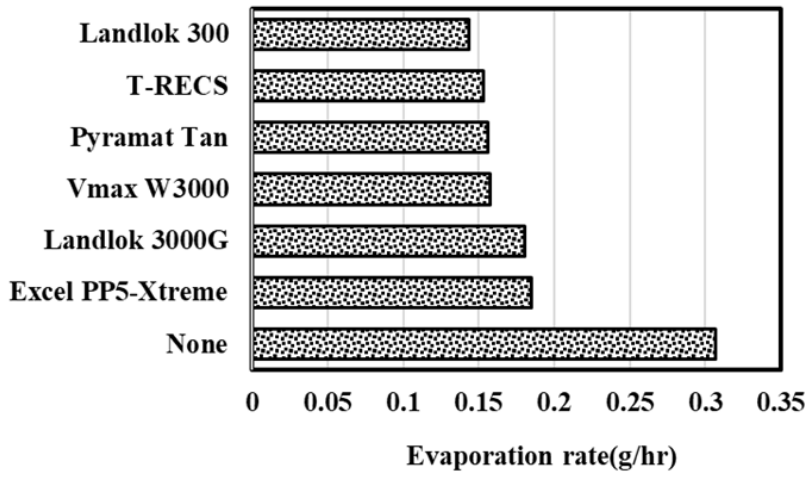

Figure 4-9. Water evaporation rate measurements.

The evaporation of water is dependent on flow-velocity, temperature, humidity, and water surface area (Hisatake et al., 1993). The evaporation test operated in this laboratory study was not aimed to measure the absolute evaporation value. Because all these tests were performed in the same lab, the same airflow velocity, temperature (22.1°C), humidity, and water surface area was maintained for all evaporation rate measurement tests. The only variable was the turf reinforcement mat covering the top of the vessels. The test results in Figure 4-9 show that TRM coverage can reduce water evaporation by 39.8~53.2%, which is significant for soil water conservation projects. However, there is not too much difference in water evaporation among the six types of TRMs. Evaporation from drying soil with three types of TRMs was also measured. The three types of TRMs were selected due to their weave structure. Excel PP5-Xtreme is similar to the other four TRMs such as Pyramat Green, Pyramat Tan, Landlok 300 and Landlok 3000G. The results are plotted in

Figure 4-10. Even though the test results illustrate different water evaporation rates measured through pure water and soil moisture with three TRM coverages, they still indicate that TRM coverage can reduce water evaporation by 40.3~78.0% compared with that without TRM coverage.

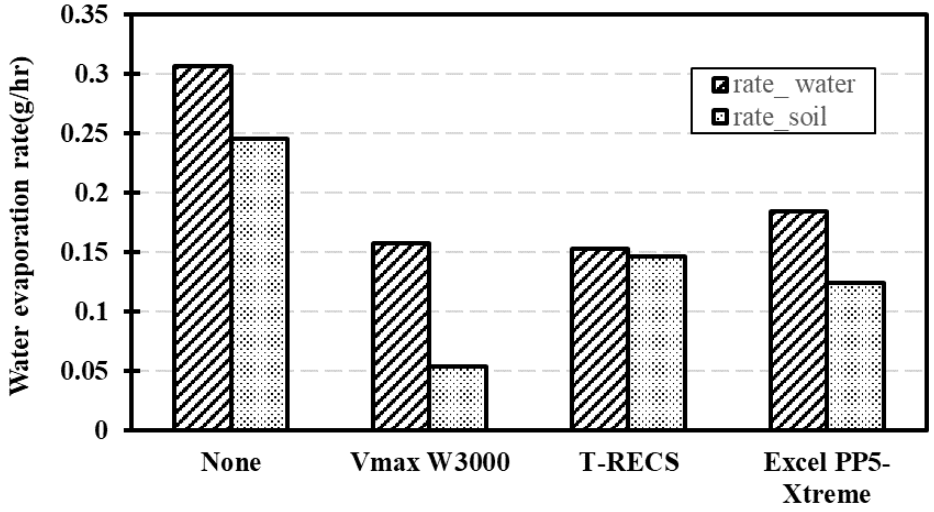

Figure 4-10. Comparison of water evaporation rate in soil and container with and without covering selected three high-performance turf reinforcement mats.

4.2.3 Pull-out test procedure

Before testing, specimen containers were filled with water 5 mm above the soil surface and allowed to stand for 48 hours to let water saturate the soil. The saturation not only reduces the friction between F75 sands and root fibers but also contributes to reducing the source of error in pullout testing by saturating the roots (Zhang et al., 2019). Then the plants were placed on a platform of a reaction frame. The experimental device setup included an LVDT, which was used to monitor the displacement of the plants, a three-jaw chuck installed on the load cell, which provided a record of pullout force on plants, a 30V power supply, and a data acquisition system as shown in Figure 4-11.

During the experiment, the rate of lowering the container was set as 5mm/min while the pulling force and displacement were recorded every 0.5 seconds. The testing process was terminated after the plant was pulled out of the soil surface and TRM covering and the pulling force had dropped to a constant low value (Figure 4-12). After the pullout testing was terminated, the plant was removed from the jaw chuck and measured the length of leaves and root system, the number of leaves and roots, and the diameter of the stem. Additional pullout tests were performed on plants that had been growing for more than four months in soil alone for comparison purposes. The data acquisition system captured force-displacement by transferring voltage data to length (mm) and force (N).

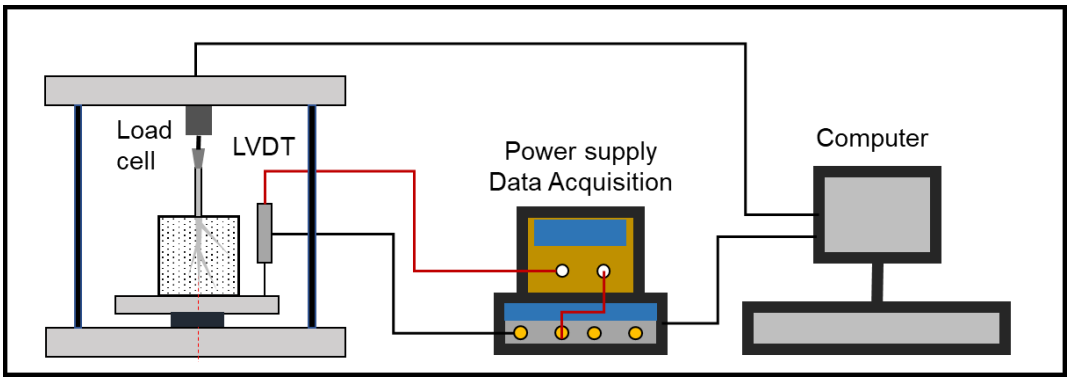

Figure 4-11. Experimental configuration of the pullout test.

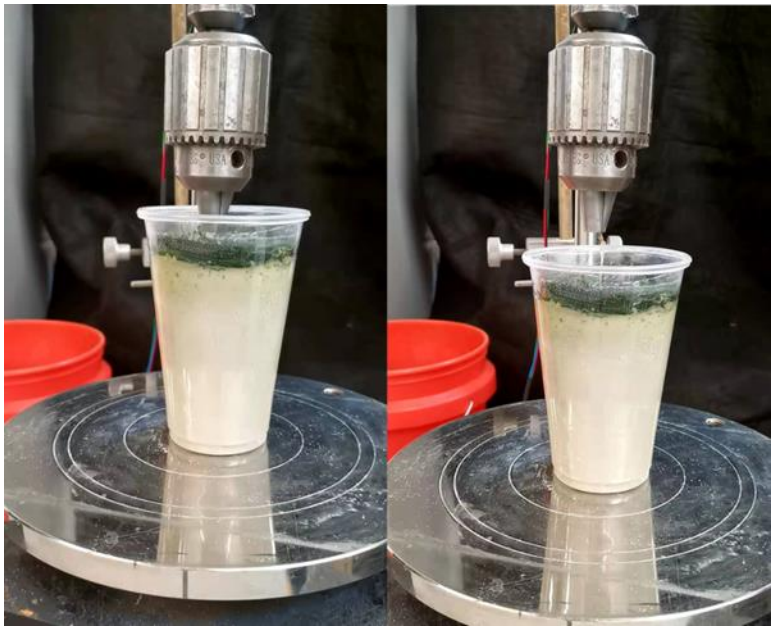

Figure 4-12. Before and after pullout test of Dandelions with TRM coverage.

4.3 Results

Figure 4-13 and Figure 4-14 show force-displacement curves recorded from the pullout test of grassroot-TRM systems. Initially, force increased rapidly within a short distance. Then it increased more slowly as the pullout process continued. There were some drops during the process due to broken roots. After reaching the maximum resistance, the force gradually decreased as roots were pulled out. Fluctuation in the force-displacement curve is reasonable. The slope of the initial force-displacement curve is defined as the initial pull-out modulus. Under the same watering amount and frequency applied in each container, the results indicate that: (1) plants with fibrous roots have higher initial pull-out modulus than plants with taproots at the same growth age; and (2) fibrous roots with TRM coverage are more difficult to pull out compared to fibrous roots without TRM coverage at a young age. Amongst the three selected TRMs, ryegrass with coverage of Vmax W3000 presented a higher pullout resistance (Figure 4-13). This may be attributed to the

interlocking between fibrous roots of ryegrass and the triple-layer matrix structure of Vmax W3000. There is no obvious difference among pullout resistances of Dandelion-TRM systems in Figure 4-14. Dandelions without coverage of TRM show a shorter root length compared with those with coverage of TRMs.

Based on testing results in Figure 4-13 and Figure 4-14, it is recommended to select VMax W3000 and plants with fibrous roots such as ryegrass in soil reinforcement and erosion control during the early stage of vegetation establishment. The triple-layered VMax W3000 with a corrugated middle layer provides separate strata zones for both root and stem reinforcement and retains seeds and soil within it.

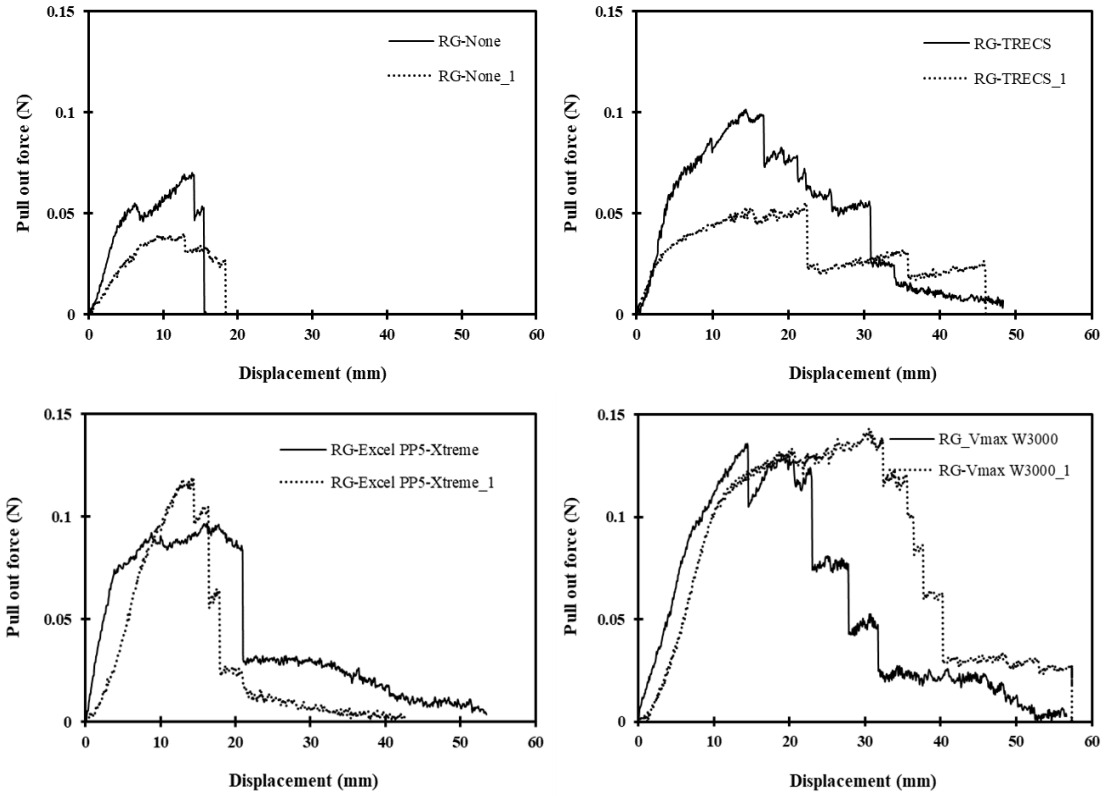

Figure 4-13. Pullout test results of the Ryegrass-TRM systems.

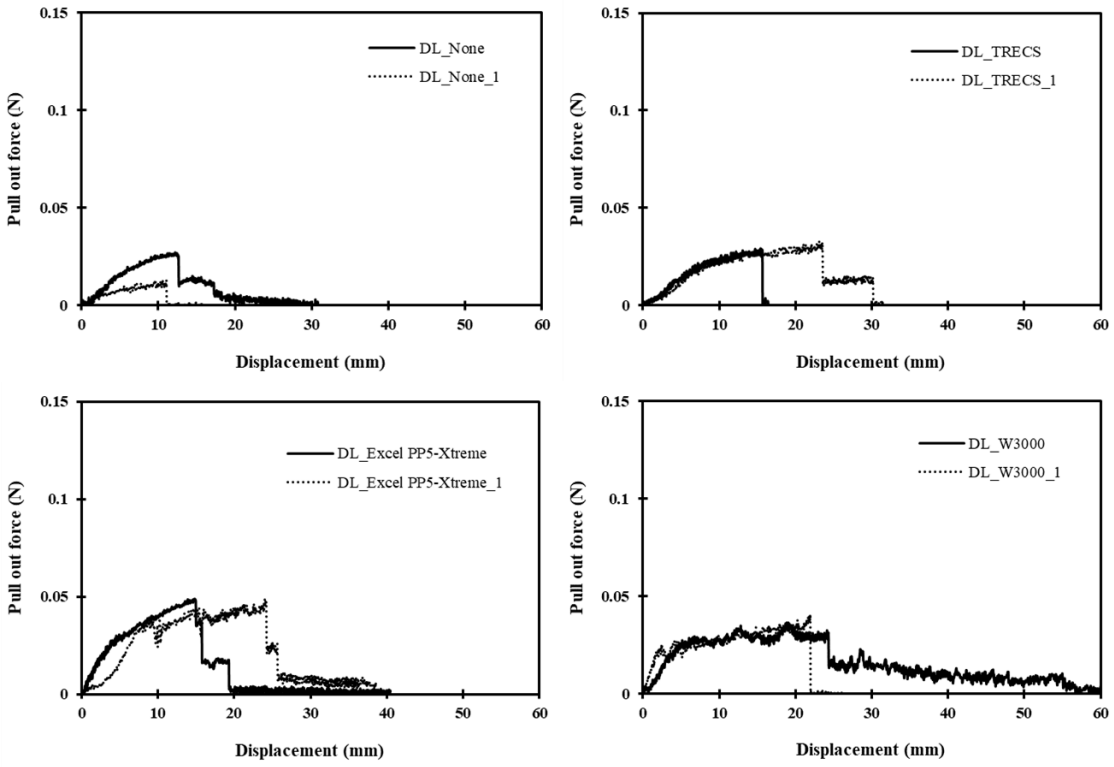

Figure 4-14. Pullout test results of the Dandelion-TRM systems.

4.4 Conclusions

The conclusions of this chapter are summarized as follows:

(1) Young plant roots with TRM coverage have a higher initial pullout modulus compared to those without TRM coverage.

(2) Young plant with fibrous roots, such as ryegrass, presents a higher initial pullout resistance and initial pullout modulus compared with plants with taproots.

(3) TRMs can benefit seed germination and plant growth by retaining soil moisture.

(4) It is recommended to select VMax W3000 to protect seed germination and reinforcement with its special triple-layered woven structure.

CHAPTER 5. SOIL REINFORCEMENT WITH TRMS

5.1 Introduction

5.1.1 Soil reinforcement using polymeric material

Soil reinforcement is an approach to soil improvement where reinforcement materials are installed in the soil to increase soil shear resistance and bearing capacity. Soil reinforcement systems consist of bi- and uni-directional reinforcement systems such as piles, nails, and geosynthetics (Khouly, 1995). Typical soil reinforcement geosynthetics include geogrids, geocell, and geotextiles. Some other materials such as plastic waste and jute fibers are also utilized for soil reinforcement.

CBR strength value is one of the most commonly used engineering indexes to describe the strength of subgrade geomaterials. Numerous researchers have studied the California Bearing Ratio (CBR) of reinforced soil with polymer fibers and geosynthetics. Minh et al. (2020) investigated CBR values of riverbed clay with multiple layers of geotextiles. Their study indicated that more reinforcement layers lead to higher bearing capacity. The test results in Chowdhury et al. (2016) presented a similar conclusion as Minh et al. 2020. They also showed that geotextile located at the top of the soil sample had the most effective improvement in CBR in both soaked and unsoaked conditions. Duncan-Williams & Attoh-Okine (2008) concluded that soil with initial higher bearing capacity would yield less improvement in CBR values with the addition of geosynthetics. Shams et al. (2019) found that freeze-thaw cycles decrease CBR values in reinforced soil samples. Brahmachary and Rokonuzzaman (2018) investigated the influences of the bamboo fiber

amount and size on soil CBR value. The results indicated that higher inclusion of bamboo fiber in soil could improve the soil CBR value. They also observed that CBR value increased with increasing length and diameter of bamboo fiber. Patel and Singh (2017) concluded that CBR value increased with increasing glass fiber content within the limit of 0.75%. Dhatrak et al. (2015) studied the effect of waste plastic bottle chips on-field CBR values in soaked and unsoaked soil conditions. Table 5.1 and Table 5.2 summarize the increase in CBR of soils with various reinforcement types for unsoaked and soaked soils, respectively.

Table 5.1 Increase in CBR of Unsoaked Soil with Reinforcement.

Soil	Geosynthetics	CBR gained	References
Silt (MH)	Geotextile	29.47 %	Minh et al., 2020
Silt&clay (OH)	Bamboo fiber (0.2%)	53.67 %	Brahmachary & Rokonuzzaman, 2018
Clayed sand (SC)	Geotextile (Top)	31.06 %	Chowdhury et al., 2016
	Geotextile (Middle)	18.44 %	
	Geotextile (Bottom)	10.68 %	
Clayey soil	Human hair (2%)	64.89%	Butt et al., 2016
Clayey soil	Plastic bottle chip (2%)	48.83%	Dhatrak &Konmare, 2016
Gravel	Geogrid #1	26%	Adams et al., 2015
	Geogrid #2	41%	
Fly ash	Waste plastic strip (0.25%) at 0.1”	56.65%	Choudhary et al., 2014
Fly ash	Waste plastic strip (0.25%) at 0.2”	40.83%	Choudhary et al., 2014
Sandy clay	Geotextile	34 %	Basu et al., 2009

Clayey soil	Geogrid	13.67 %	Duncan-Williams & Attoh-Okine, 2008
Clayey gravel		15.50 %	
Silt soil #1		11.89 %	
Silt soil #2		6.90 %	

Table 5.2 Increase in CBR of Soaked Soil with Reinforcement.

Soil	**Geosynthetics**	**CBR gained**	**References**
Silt (MH)	Geotextile	200 %	Minh et al., 2020
Clay(CH)	PP fibre (0.3%)	37.8 %	Wang et al., 2019
	PP fibre (0.6%)	77.8 %	
	PP fibre (0.9%)	100 %	
Silt&clay (OH)	Bamboo fiber (0.2%)	24.25 %	Brahmachary & Rokonuzzaman, 2018
Clayed sand (SC)	Geotextile (Top)	38.83 %	Chowdhury et al.., 2016
	Geotextile (Middle)	15.58 %	
	Geotextile (Bottom)	3.0 %	
Clayed soil	Plastic bottle chip (2%)	35.08 %	Dhatrak &Konmare, 2016
Gravel	Geogrid #1	12%	Adams et al., 2015
	Geogrid #2	31%	
Clayey soil	Geogrid	17.80 %	Duncan-Williams & Attoh-Okine, 2008
Clayey gravel		19.80 %	
Silt soil #1		5.15 %	
Silt soil #2		8.20 %	

Figure 5-1 compares CBR improvement amount in unsoaked and unsoaked soils based on collected data from Table 5.1 and Table 5.2. Figure 5-1 displayed the amount of

CBR improvement of soil specimens compacted at optimum moisture content in both soaked and unsoaked conditions. In most cases shown in Figure 5.1, Soil CBR value improvement is greater in unsoaked conditions than in soaked conditions.

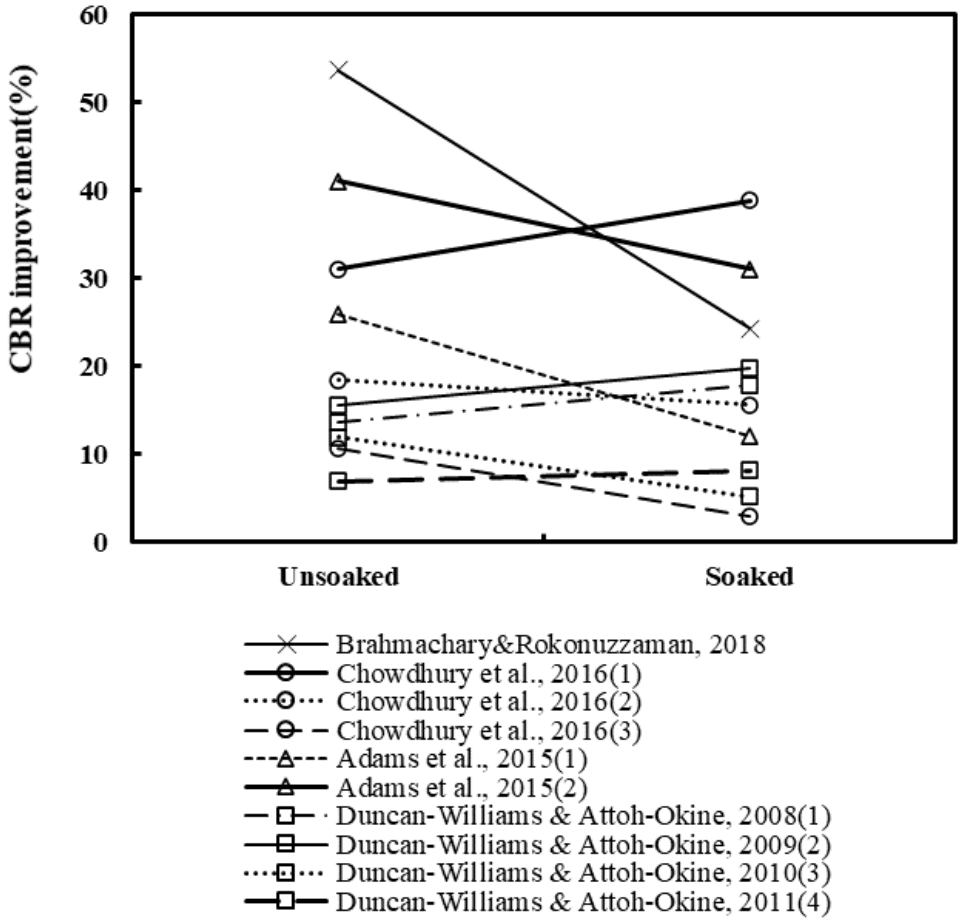

Figure 5-1. Comparison of CBR improvement in soaked and unsoaked conditions.

5.1.2 Research problems

Although synthetic materials are widely studied in soil reinforcement, no research has been conducted on TRM-reinforced soil. The main objective of this study is to investigate the benefit of TRM reinforcement on the bearing capacity of soil by performing modified CBR tests.

5.2 Method

In this study, laboratory CBR tests were performed according to the procedure of ASTM D 1883 (2016) and compaction of the soil is according to Method C in ASTM D 698 (2012). The diameter and height of the mold are 152 (6 inches) and 116 mm (4.58 inches) respectively. The soil (Figure 5-2) used in this study is locally available in Georgia. The soil specimens are prepared by passing 19.0 mm sieve. Standard Proctor compaction tests are carried out to determine the maximum dry density (MDD) and optimum moisture content (OMC). The compaction curve of the soil specimen is plotted in Figure 5-3. The zero air void line (ZAV) is also presented which confirms that the plotted compaction curve is reasonable. The soil is mixed thoroughly with water corresponding to its OMC of 24.2% and MDD is 15.3 kN/m^3. Then the soil is placed in the mold and compacted in three layers under standard effort.

Figure 5-2. Oven-dried soil sample.

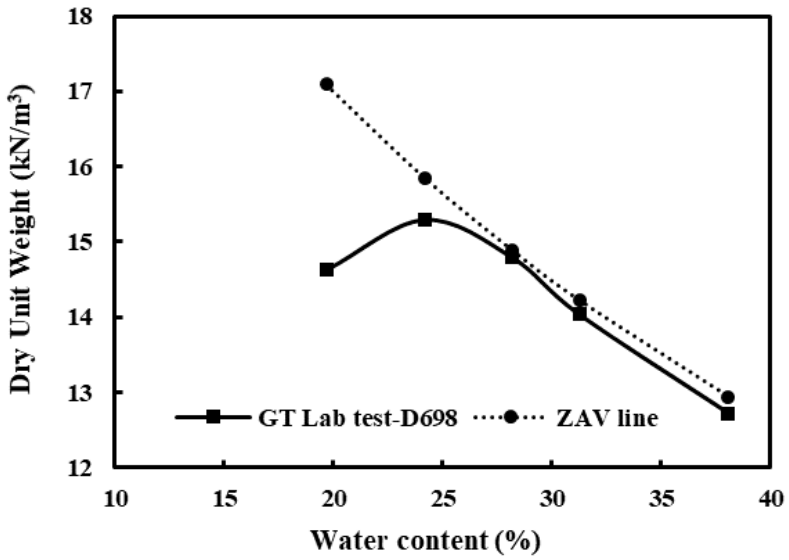

Figure 5-3. Standard proctor compaction curve of Georgia red clay sample.

TRM specimen is placed at the top of the soil specimen and fixed within a circular clamp which was used in the static puncture tests described in Chapter 3. Four TRM specimens are tested in this study: Excel PP5-Xtreme, TRECS, Vmax W3000, and Pyramat Green. The complete test setup is illustrated in Figure 5-4. The soil-TRM system is placed on a load frame. A load cell connected to a piston and an LVDT are connected to a data logger to record force and displacement during the test. By pushing the mold base upward at the constant rate of 0.05 in/min (1.27 mm/min), the load is applied to the test specimen throughout the piston penetration. The load and displacement values are recorded every 0.05 in until total penetration of 2 in. The standard CBR test of soil only case is also conducted to compare the performance of TRMs in soil reinforcement.

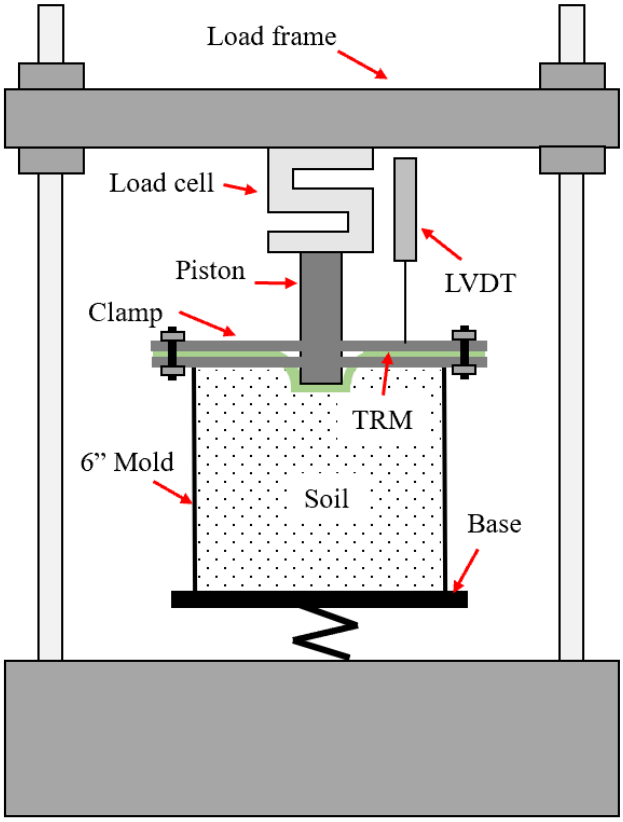

Figure 5-4. Test configuration of CBR test.

5.3 Results and discussion

This study allows for assessment of the reinforcing role of TRM by developing a soil-TRM composite penetration test. In this study, five soil specimens were prepared, and ASTM-standardized-method California Bearing Ratio tests were performed to compare the results of the soil reinforcement by TRMs. Because there's a small gap between TRM and soil specimen, the initial load penetration curve presents a concave upward shape. The latter part of curve shows the reinforcement from TRM. The following load-displacement curves of soil-TRM specimens are plotted after adjusting the initial compression of TRMs (Figure 5-5~5-8). Figure 5-9 compares the test results for the five specimens and illustrates that TRMs reinforce the soil in terms of both initial modulus and final bearing load.

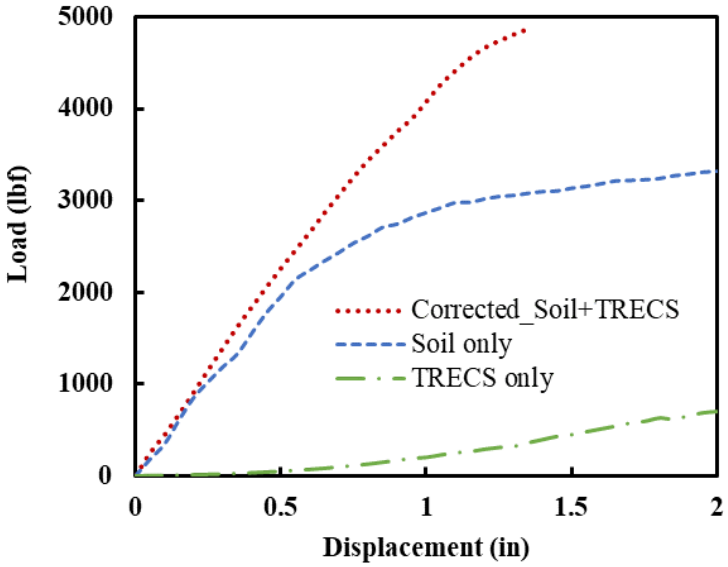

Figure 5-5. Load displacement curve of soil-TRECS system.

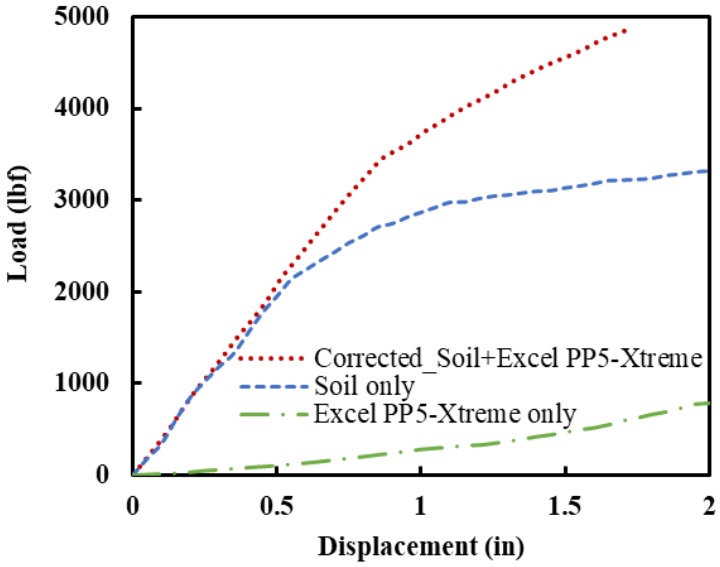

Figure 5-6. Load displacement curve of soil-Excel PP5-Xtreme system.

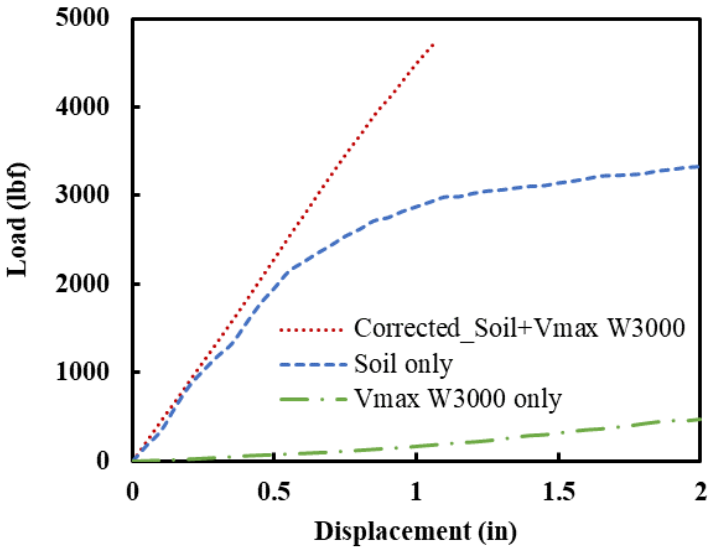

Figure 5-7. Load displacement curve of soil-Vmax W3000 system

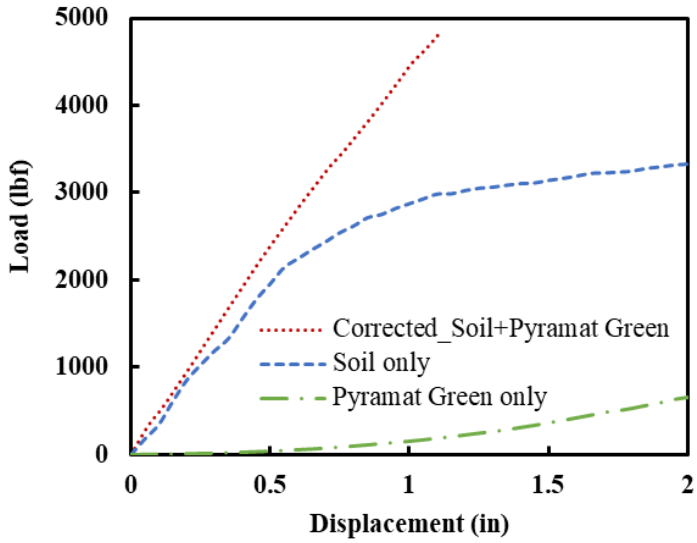

Figure 5-8. Load displacement curve of soil-Pyramat Green system

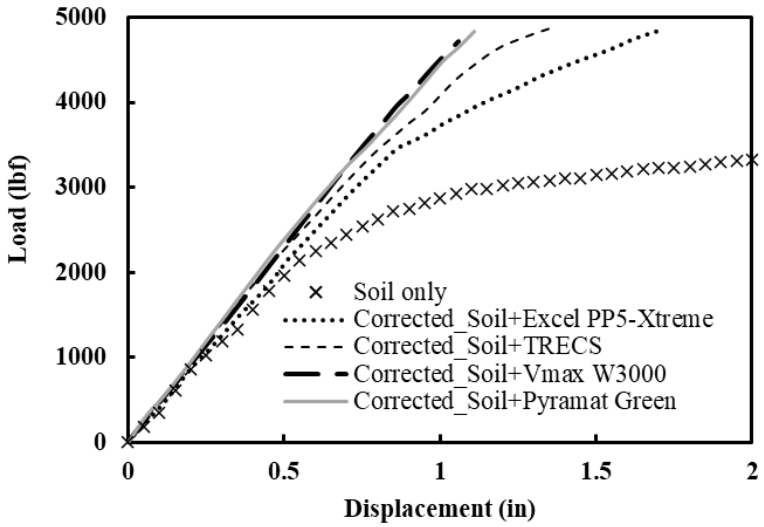

Figure 5-9. Comparison of load-displacement curves of soil specimen reinforced by different turf reinforcement mats.

CBR values are calculated based on stress readings at 0.1 (2.5 mm) and 0.2 inch (5.1 mm) of penetration from the load-displacement curves. The improvement in CBR value of soil with TRM reinforcement present compared to unreinforced soil is calculated as a ratio of CBR value of reinforced soil to that of soil only minus one. This value indicates the contribution of TRM reinforcement to increasing the CBR value of soil. The comparison of soil reinforcement with different TRM specimens is shown in Table 5.3. The results present that TRM enhances the CBR strength at 0.1 inches by up to ~ 60% compared with soil specimens. This effect decreases when penetration reaches 0.2 inches. Among the four TRMs, Pyramat Green shows the greatest improvement in the CBR value of the soil-TRM system. TRECS and Excel PP5-Xtreme provided a lower amount of reinforcement on the soil. Figure 5-10 ~ Figure 5-14 display the correlation between CBR enhancement and the physical properties of TRM. Higher puncture resistance of TRM and mass per unit area indicate more enhancement of CBR value. However, Figure 5-13

indicates that there is no clear relationship between tensile strength and CBR improvement although a slightly positive correlation might be argued.

Table 5.3. Results of CBR test for different TRMs.

Test cases	CBR at 0.1"	Increase in CBR at 0.1"	CBR at 0.2"	Increase in CBR at 0.2"
Soil only	11.05 %	-	17.84 %	-
Soil + TRECS	14.97 %	36.11 %	20.31 %	13.78 %
Soil+ Excel PP5-Xtreme	15.02 %	36.56 %	20.20 %	13.17 %
Soil + Vmax W3000	16.73 %	52.08 %	21.23 %	18.93 %
Soil + Pyramat Green	17.58 %	59.79 %	22.13 %	23.98 %

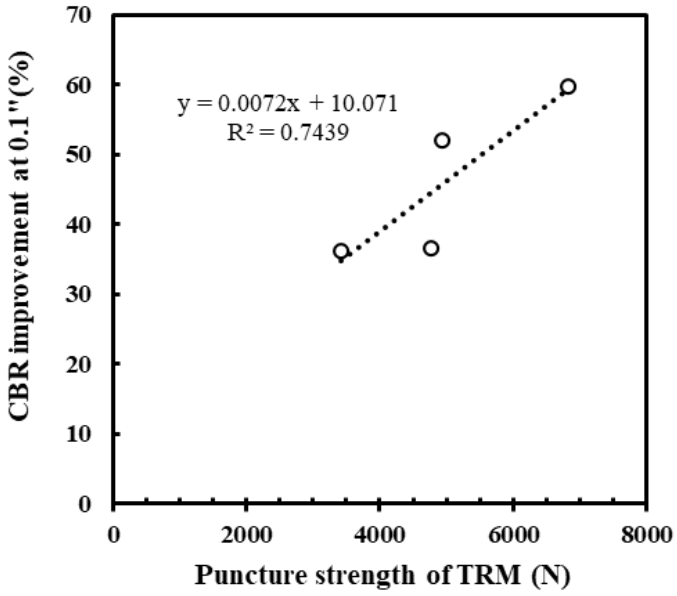

Figure 5-10. Correlation between soil reinforcement by TRM and static puncture resistance of TRM.

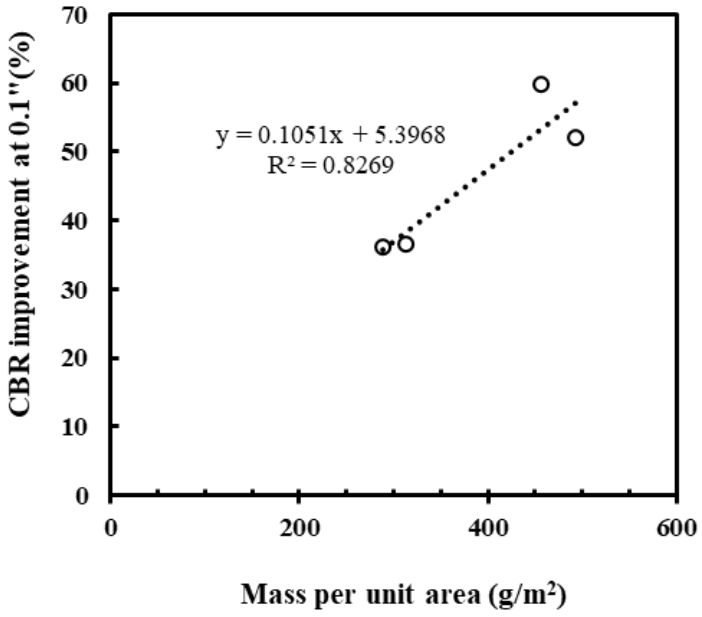

Figure 5-11. Correlation between soil reinforcement by TRM and mass per unit area of TRM.

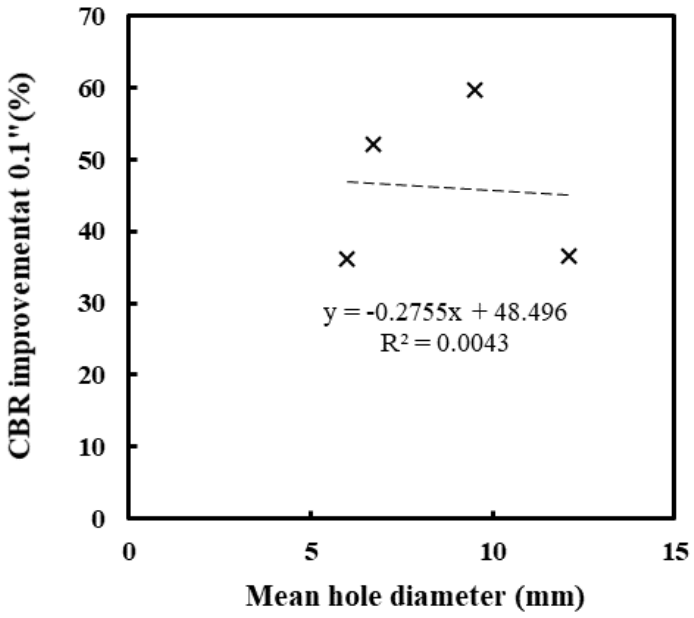

Figure 5-12. Correlation between soil reinforcement by TRM and mean hole diameter measured from the dynamic perforation test.

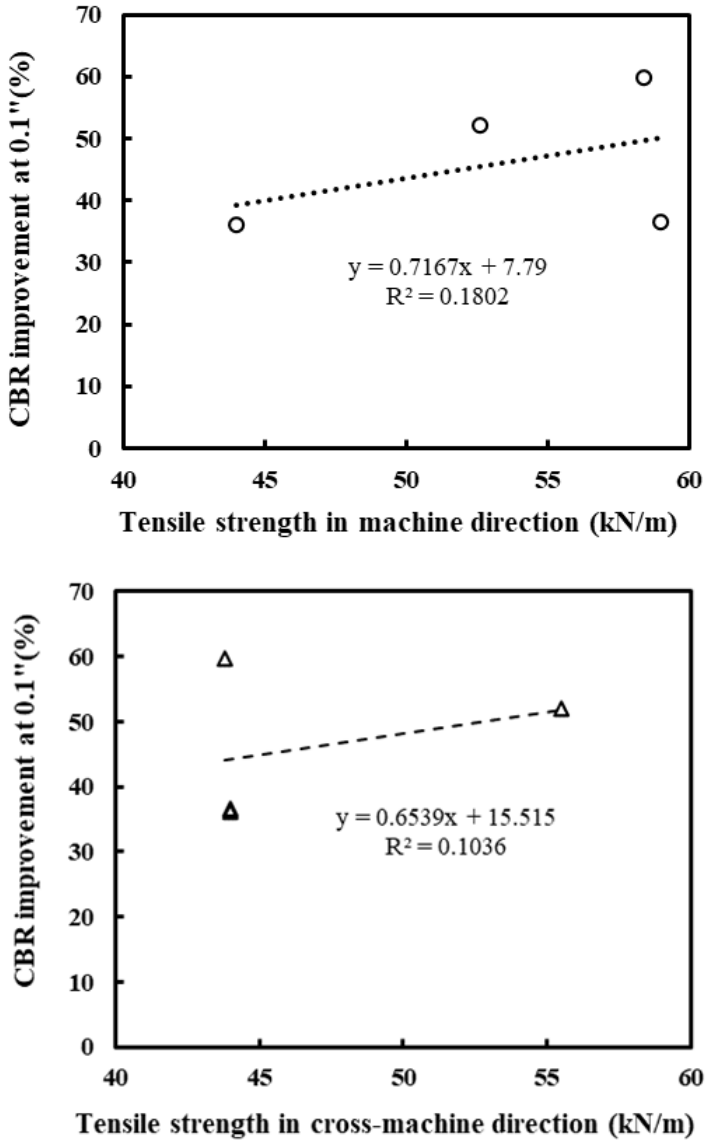

Figure 5-13. Correlation between soil reinforcement by TRM and tensile strength of TRM in the machine and cross-machine directions.

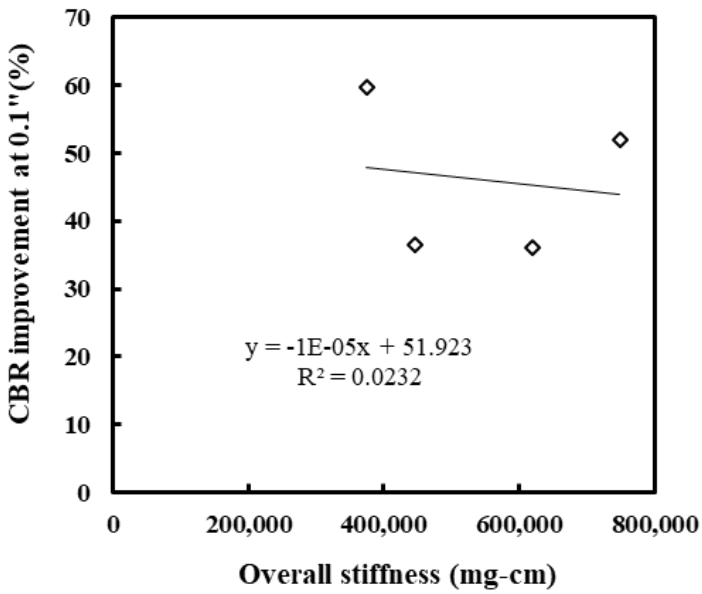

Figure 5-14. Correlation between soil reinforcement by TRM and overall stiffness of TRM.

5.4 Conclusion

A penetration test is proposed for soil-TRM composite specimens to evaluate the reinforcing role of TRM. Based on the present investigation, the following conclusions are drawn:

(1) The improvement of the CBR value of the soil-TRM system at 0.1 inches penetration is greater than that at 0.2 inches.

(2) CBR value of soil increases with the inclusion of turf reinforcement mat. Also, there are increases in both strength modulus and bearing load under a constant rate of penetration with coverage of turf reinforcement mat on the top of the soil.

(3) Pyramat Green shows the greatest improvement in the CBR value of the soil-TRM system, which is up to ~ 60% when compared to unreinforced soil. TRECS and Excel

PP5-Xtreme present a lower amount of reinforcement with soil compared with Pyramat Green and Vmax W3000.

(4) Higher puncture strength of TRM and mass per unit area show a greater enhancement of CBR values. This indicates that a stronger TRM material can improve the soil CBR value more.

(5) The is no clear correlation between the enhancement of penetration parameter and other index properties of TRMs such as stiffness, tensile strength, and hole diameter measured in dynamic perforation test.

CHAPTER 6. NUMERICAL SIMULATIONS

6.1 Introduction

6.1.1 Review of modelling impact response of textiles

In recent years, textiles, treated as soft body materials, have been widely designed and applied in astronomy, civil engineering, and medical science. With the development of apparel and industrial textiles, the basic mechanical properties, testing methods, and evaluation parameters are receiving more attention. The traditional design and mechanical property evaluation of textiles are mostly based on the empirical experience of the designer. This leads to a longer period and higher cost of manufacturing due to the complicated process going from material selection to property testing. Numerical simulation of fabric mechanical properties can help in saving resources, lowering costs, and reducing the manufacturing period. Most numerical studies on puncture resistance have focused on fiber-reinforced polymer composites (FRP) and metal materials while there is limited research on geosynthetics, such as geogrids and turf reinforcement mats.

The deformation of polymeric fabrics, such as creep and stress rearrangement, is usually described by a non-linear elastic-plastic constitutive model. The energy absorption during puncture is affected by material properties, the geometry of the fabric, the shape of the projectile, the impact velocity, the fiber-fiber friction, the fiber-projectile friction, and the boundary conditions (Cheeseman & Bogetti, 2003). The stress and deformation in the microstructure of woven textiles follow the constitutive relationships of material elasticity and plasticity. The stress of fibers increases when the textile is exposed to impact. Higher

tensile strength and failure strain are helpful to mitigate the impacting energy (Tran et al., 2014). Stress and deformation distribution during the puncture process can be determined using the finite element method. The purpose of this study is to provide a convenient method to identify the parameters which influence puncture resistance.

In numerical modeling, material property plays an important role and the values of parameters are usually based on experimental testing. Table 6.1 and Table 6.2 summarized the tested material properties of woven fabrics from literature.

Table 6.1. Tested Material Properties for Woven Fabrics.

Material	E (GPa)	Yield strength (MPa)	Strain at failure (%)	References
PP geotextile	0.033 0.24~0.9 6	380.09 35 -	30.56 1.5 -	Karademir &Frost, 2014 Perkins, 2000
PP geogrid	0.2 0.3 0.6~0.65 2.6~6.5	12 20 25 168	15 15 3 8	Hussein & Meguid, 2016 Perkins, 2000 Dong et al., 2010
PET geotextile	6.0~12.2	1067~2761	14.6~26.1	Rix, 1995
Coir fibres	0.19~0.21	18.69~33.18	8.7~16.2	Subaida et al., 2008
Cotton	0.032	0.3	9	Penava et al., 2014
Geo-jute	2.1	-	-	Rahman et al., 2019
Wool	0.022	0.33	15	Penava et al., 2014
PES	0.005	0.6	42	Penava et al., 2014
Aramid	10.86	2523	-	Yahya et al., 2014
Glass FRP	20.4	280	18	Wang et al., 1995
Kevlar 49	23.8 120~160	425 1400~2200	11 2.5~3.5	Wang et al., 1995 Zhu et al., 2011
Jute laminate	7	60	2.5	Gowda et al., 1999
Polyester resin	1.4	12.1	4.5	Gowda et al., 1999
E-glass/vinylester	42.8	2024	-	Zako et al., 2003
URETEK 5893	-	5.56 8.84	0.014 0.072	Hu et al., 2017

Kevlar 149	1.236 2.079	37.38 40.3	4.09 3.72	Yahya et al, 2011
PET	7.32 6.97	-	-	Wang et al., 2012
Polyamide-66	5.980 0.1196	-	-	Zhou et al., 2020
Carbon/epoxy	220	565		Dixit et al., 2015
PP-glass FRP	118 120	-	-	Valizadeh et al., 2010
Carbon/epoxy FRP	56	554	1.8	Hochard et al., 2001
Woven GRP	26.6 30.6	412 453	1.96 1.96	Callus et al, 1999
Carbon/glass	2.7	70	1.45	Lomov et al., 2008
FEM simulated woven fabric	15	-	-	Li et al., 2017 Wang et al., 2009

Table 6.2. Volume density and Poisson ratio.

Material	Density (g/cm^3)	Poisson ratio	References
E-glass/vinylester	-	0.254	Zako et al., 2003
Kevlar 149	1.44	0.37	Yahya et al., 2011
Kevlar 49	1.44	-	Zhu et al., 2011
PET-TPU	1.25	0.2	Wang et al., 2012
Nonwoven geotextile	1.43	-	Saberi et al., 2017
Woven fabric	1.25	0.2	Wang et al., 2018
KM2	1.44	0.24	López-Gálvez& Soldani 2019
Steel	7.8	0.3	López-Gálvez& Soldani 2019
Aluminum	2.79	0.33	López-Gálvez& Soldani 2019
Polyamide-66	-	0.3	Zhou et al., 2020
FEM simulated woven fabric	-	0.25	Li et al., 2017 Wang et al., 2009
Cotton	0.472	0.216	Penava et al., 2014
Wool	0.413	0.263	Penava et al., 2014
PES	0.653	0.381	Penava et al., 2014
Carbon/epoxy FRP	-	0.035	Hochard et al., 2001
Jute laminate	1.18	0.25	Gowda et al., 1999

Polyester resin	1.22	0.38	Gowda et al., 1999
Carbon/glass	0.91	0.4	Lomov et al., 2008
Coir fibres	0.12	-	Subaida et al., 2008

The challenge in the simulations involves the instability of material and discontinuity of response (Belytschko, 1996). Tran et al. (2014) discussed the advantages and limitations of modeling fabric as homogenized membrane, woven shell elements, and the finest scale at yarn level. Although the approach to building a fabric matrix architecture at a yarn level seems to be the closest way to simulate textile performance such as yarn bending, uncrimping, and sliding, many complicated details such as filament path and yarn-to-yarn interaction are simplified in the numerical simulations. The computational cost of this approach is also very intense and not suitable for materials with complicated woven or knitted structures. Besides, previous studies mostly focused on the ballistic impact on the woven materials, thus failure and deformation at the microscale were extremely important considering the narrow impact area. The static puncture test looks at the failure modes in macro-scale compared with the ballistic perforation test. In this study, the simplified approach is the most efficient way to capture the mechanical response of woven TRMs.

6.1.2 Constitutive model of soil

Mendoza and Caicedo (2018) applied an elastoplastic model to simulate the standard CBR test. The initial stress-strain curve is linear in the elastic behavior and follows Hooke's Law. In plastic behavior, the soil failure path follows the modified Drucker-Prager model (Figure 6-1). In Figure 6-1, the failure surface consists of two parts, one is the Drucker-Prager failure surface and the other is the cap yield surface. The Drucker-Prager failure surface is expressed as:

$$F_s = t - ptan\beta - d = 0 \tag{11}$$

where p is mean effective stress, t is deviator stress, β is the friction angle and d is cohesion. The cap yield surface is expressed as:

$$F_c = \sqrt{(p - p_a)^2 + \left(\frac{Rt}{1 + \alpha - \alpha/cos\beta}\right)^2} - R(d + p_a tan\beta) = 0 \tag{12}$$

where R is a material index; α is a number to define transition surface between Drucker-Prager failure surface and the cap, p_a is a function of volumetric plastic strain which is calculated from

$$p_a = \frac{p_b - Rd}{1 + Rtan\beta} \tag{13}$$

where p_b is a parameter based on the compression law of material and is a function of void ratio and volumetric strain. p_b is calculated from

$$\varepsilon_v^p = \frac{\lambda - \kappa}{1 + e_0} ln \frac{p}{p_b} \tag{14}$$

where e_0 is the initial void ratio, λ is the slope of the virgin isotropic compressibility line, and κ is the slope of the unloading-reloading line of soil. The transition failure surface between the Drucker-Prager and the cap yield surface is expressed as

$$F_t = \sqrt{(p - p_a)^2 + \left[t - \left(1 - \frac{\alpha}{cos\beta}\right)(d + p_a tan\beta)\right]^2} - \alpha(d + p_a tan\beta) = 0 \tag{15}$$

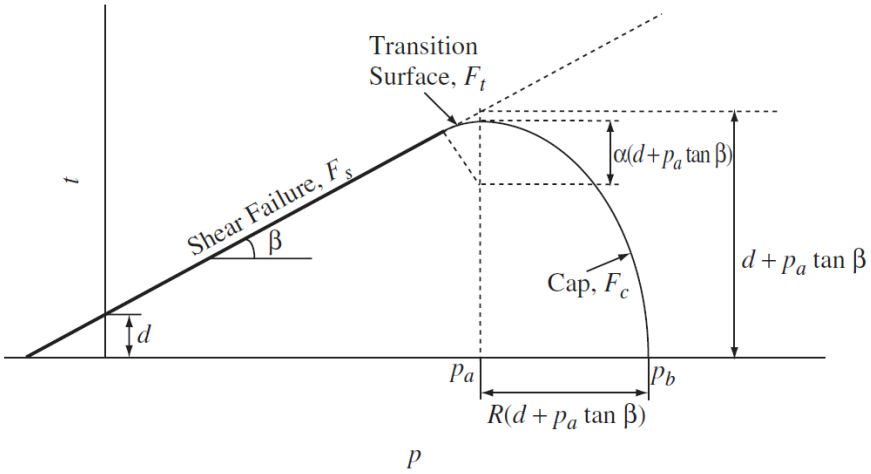

Figure 6-1. Yield surface in the modified Drucker-Prager model (Helwany, 2007)

6.1.3 Research problems

In practice, turf reinforcement mats and other woven erosion control products are facing damage from punctures by dropped stones and knife cuts amongst other effects. This can lead to loss of material endurance in long-term erosion control. Finite element analysis can be used to predict stress and deformation distribution at each time step of the puncture process. The objective of this chapter is to simulate the puncture process and to study the damage characteristics of woven turf reinforcement mats considering the shape of the probe, material density and geometry of the fabric model.

6.2 Method

6.2.1 Geometry model of probe

A series of simulations are performed with projectiles of the same mass and impact energy. The projectile is defined as a discrete rigid body with different tip shapes of flat, cone, and hemisphere for each projectile. The angle of the cone-shape tip is 45 degrees, which is the same as the angle of the drop cone tip in the dynamic perforation test. Point

mass inertia is applied to the probe. The projectile models with different tip shapes are shown in Figure 6-2. Because the probe model is a rigid body, we do not need to determine the material property for the probe.

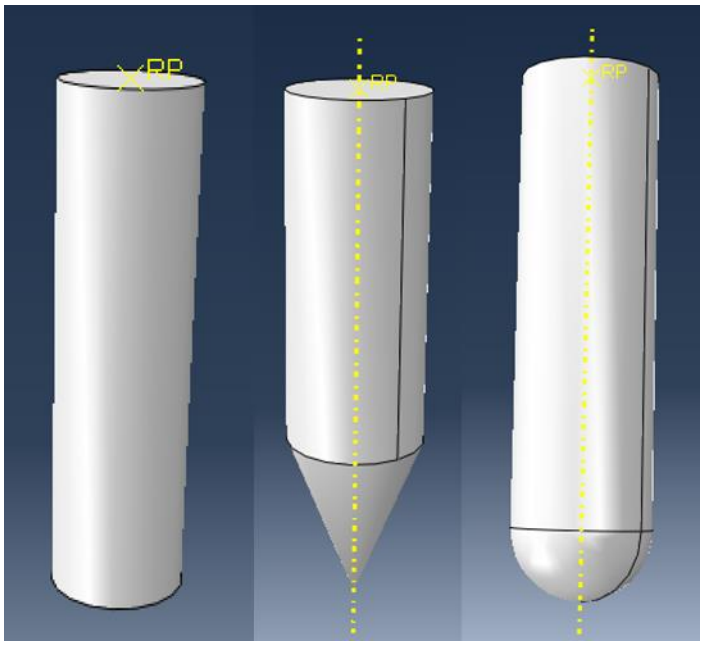

Figure 6-2. Project models in ABAQUS: flat, conical, and hemispherical tip shapes.

6.2.2 Geometry model of turf reinforcement mat

The previous simulations (Özdemir& Mert, 2013) of the indentation and burst process on woven textiles assumed different interactions between fabric and projectile. Although previous studies assumed the shape and arrangement of fibers, they (Sockalingam et al., 2017; Jovicic, 2003) could not completely represent the actual interaction between yarns in the machine and cross-machine directions, as well as the interaction between woven textile and projectile. Considering the difficulties of defining contact properties as well as the assembly of fibers, holes were used in a fabric plate model to represent the voids between the yarns. Figure 6-3 displays a geometry model for TRM with a plain weave matrix. Figure 6-4 displays geometry models for TRM pyramid

structure matrix. The material of the TRM models is assumed isotropic. Considering the woven TRMs mentioned in Chapter 3 are all made of polypropylene and we lack elastic modulus and yield strength measurements from manufacturers, the material property defined in this part will be based on collected values for PP geotextile and geogrids in literature. The range of elastic modulus is between 33~6500 MPa while the range of yield strength is between 12~380 MPa which was shown in Table 6.1. The material property settings are summarized in Table 6.3.

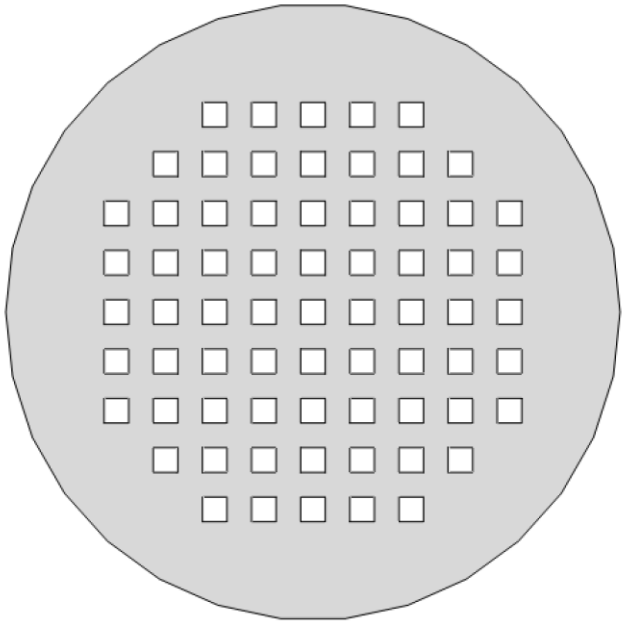

Figure 6-3. TRM model with a similar shape of plain weave matrix.

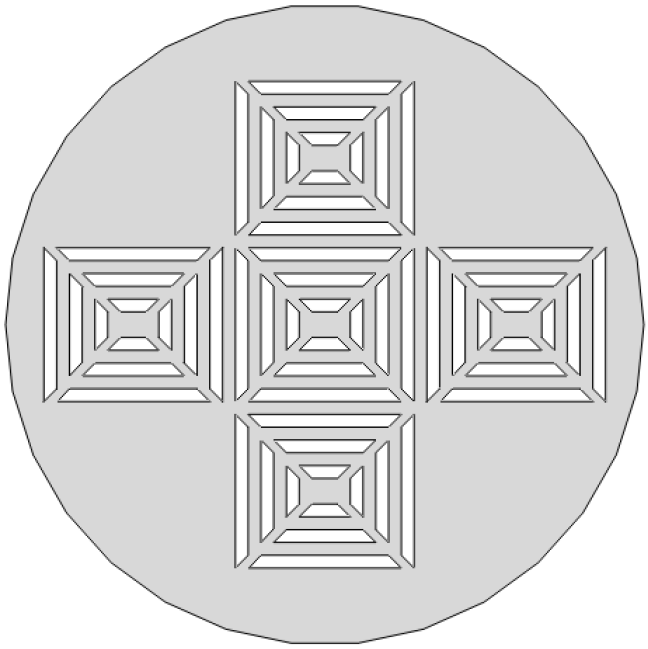

Figure 6-4. TRM model with a similar shape of pyramid structure matrix.

Table 6.3. Material Properties.

Density (g/cm^3)	Elastic modulus (MPa)	Yield stress (MPa)	Poisson ratio
0.9	500	20	0.3

6.2.3 Load and boundary conditions

The TRM fabric model is restrained at the boundary without displacement in x, y and z directions. The dynamic explicit module is used in this simulation and the load in z-direction is applied to the reference point of the projectile. The damaged elements are deleted by defining a damage evolution based on effective plastic displacement. Figure 6-5 displays the load and boundary condition regions in the model. The simulation is modeled at the same velocity of as the projectile movement.

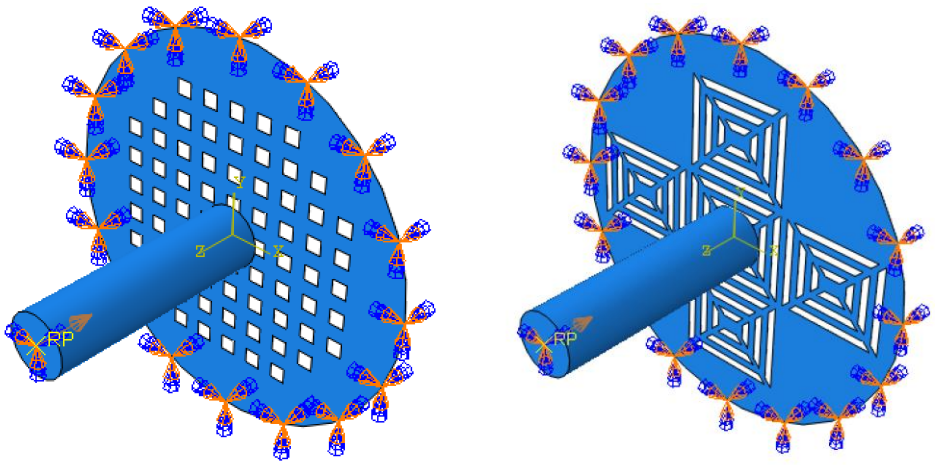

Figure 6-5. Load module and boundary conditions of the models.

6.2.4 Meshing scheme of the fabric and projectile

The rigid projectile is modeled by 898 R3D4 elements and the TRM material with plain weave geometry is modeled by 8608 C3D8R elements as shown in Figure 6-6 and 6-7. TRM model with the architecture of the pyramid matrix is modeled by 3222 C3D10 elements displayed in Figure 6-8. Other sizes and types of elements were also considered but issues such as much longer calculating time and great element distortion occurred during the meshing process.

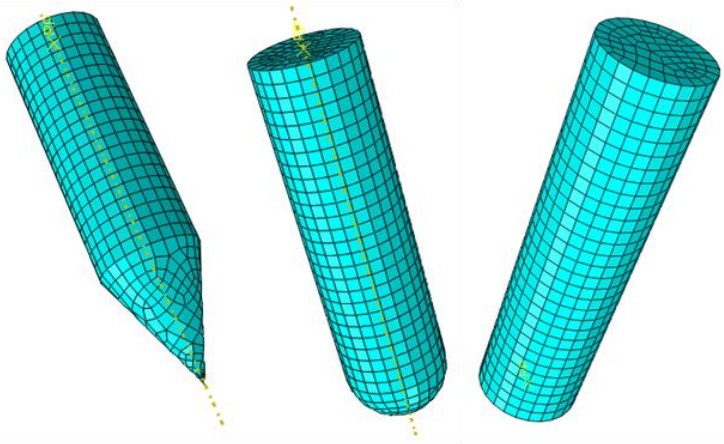

Figure 6-6. Finite element discretization of rigid probes with different shapes.

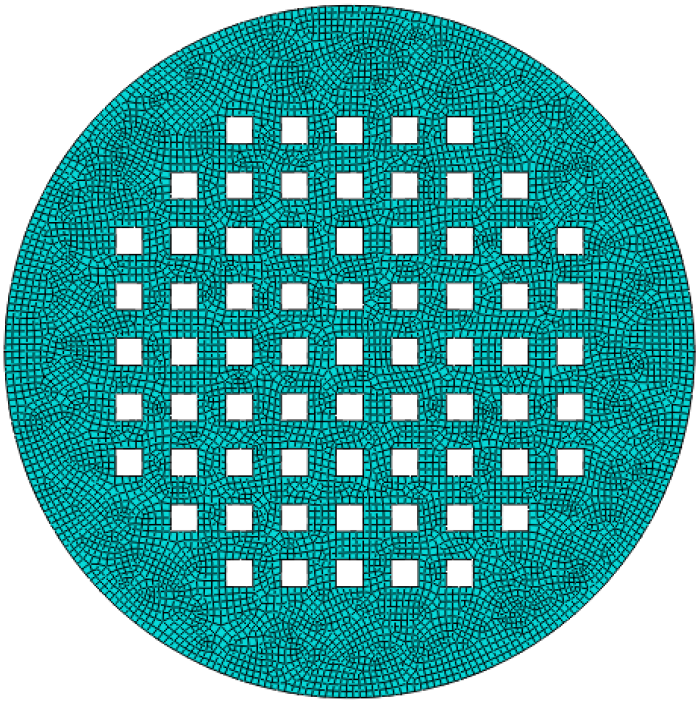

Figure 6-7. Finite element discretization of plain weave fabric model.

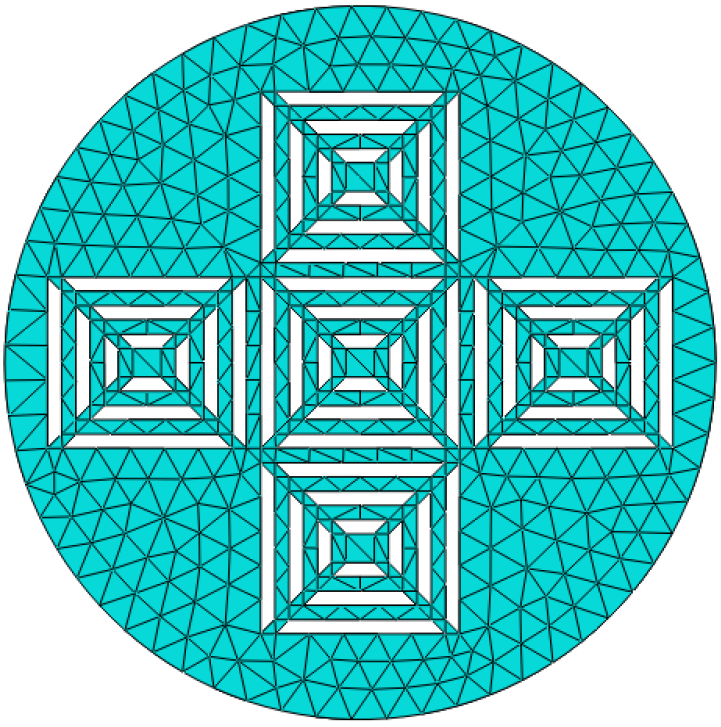

Figure 6-8. Finite element discretization of pyramid matrix fabric model.

6.3 Simulation of CBR test on soil and TRM system

6.3.1 Geometry model of soil and TRM system

The model of the soil-TRM system is defined as an asymmetry model. The size of the soil model is designed as a cylinder with a radius of 76 mm and a depth of 60 mm. The red-colored blocks above the green rectangular block (Figure 6-9) is defined as TRM material. The material properties of soil include a density of 2 g/cm^3 and an elastic modulus of 28 MPa. The Poisson ratio is 0.3 for both materials.

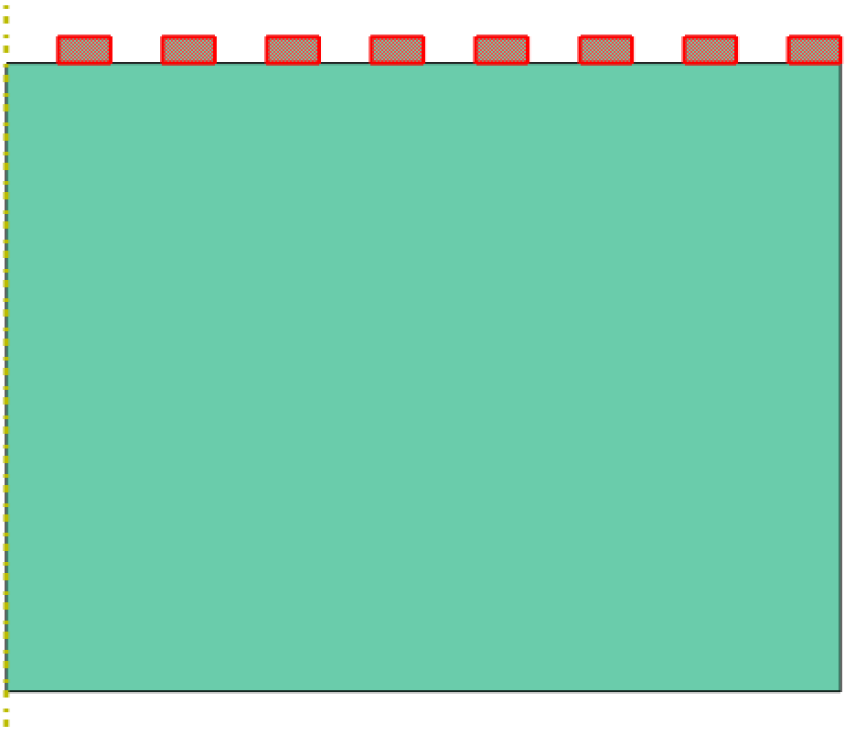

Figure 6-9. Geometry model of the soil-TRM system.

6.3.2 Load and boundary conditions

Due to symmetry in geometry, only a quarter of the cylindrical soil specimen is modelled. The y axis of the model and boundary of TRM is specified as XSYMM where

U1, UR2, and UR3 are fixed. The x-axis of the model is located at the base of soil and the boundary condition is defined as zero displacements in x and y directions. The outside of the soil cylinder boundary is restrained by zero displacements in the x-direction. The boundary condition of the model is displayed in Figure 6-10. The load is applied to the model in the vertical direction. 2280 C3D8R elements are generated in the model (Figure 6-11). C3D10M elements were also tried but caused great element distortion during mesh generation. The contact between TRM and soil is defined as a general contact.

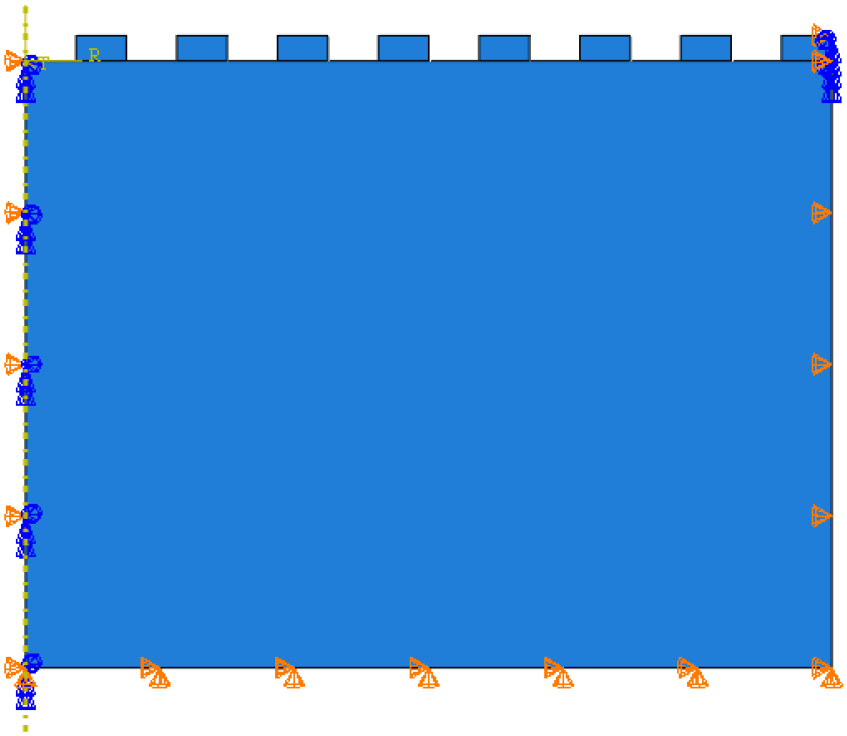

Figure 6-10. The boundary condition of soil-TRM model.

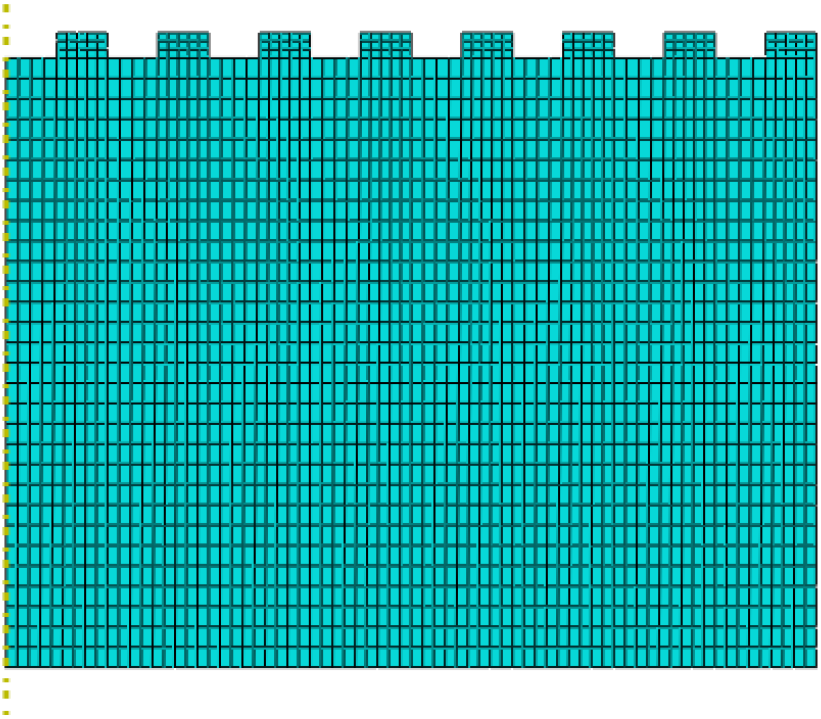

Figure 6-11. Finite element discretization of soil-TRM model.

6.4 Results

Because of the lack of testing data of the anisotropic TRM material, the material is assumed isotropic in the simulated model. Besides, the purpose of this study is to compare the influence of probe shape, fabric geometry, and density on simulation results, so it is not necessary to compare the results with experimental testing data in this thesis.

6.4.1 Influence of tip shape

The puncture process is usually divided into two steps: first, the projectile penetrates the fabric from its voids, the yarns rearrange and extend with the fabric surface moving in the same direction as the projectile moves; then the yarns break due to shear or tensile failure and fabric surface rebounds.

The shape of the projectile affects the response of fabric to penetration by surface contact. The observation of the simulation results (Figure 6-12~Figure 6-14) indicates that the broken parts were located at the edge of the projectile tip which is in accordance with the conclusion from Prosser et al. (2000). This phenomenon can be explained by stress concentration in the filaments at these locations. It can be observed that the yarns slip when a conical projectile penetrates the fabric. There are fewer yarns involved in energy absorption. Hemispherical projectiles were found to penetrate the fabric mainly by stretching the yarns to tensile failure, and flat projectiles sheared the yarns due to their sharp edges. The vertical displacements of the fabric surface display distinctive characteristics during the puncture process. At the initial contact between projectile and fabric, the fabric contacted with flat-tip projectile (Figure 6-12) shows a circular shape of deformation while the other two fabrics contacted with conical-tip (Figure 6-13) and hemispherical-tip (Figure 6-14) projectiles present a square shape of deformation. When the fabric fails, four yarns break at the fabric contacted with flat-tip projectile, two yarns break at the fabric contacted with conical-tip projectile, and three yarns break at the fabric contacted with a hemispherical-tip projectile. Flat projectile tip shape indicates the capability to impact more yarns thus leads to higher resistance to fabric failure.

Figure 6-15 shows that woven fabric impacted with a projectile with a flat tip has the greatest deformation at failure. When comparing the energy dissipation (Figure 6-16, Figure 6-17) during the puncture process, the energy absorption of the fabric was greater with penetration by flat and hemispherical projectiles than in penetration with a conical projectile. A previous study with similar modeling results (Yahya et al., 2012) concluded

that flat-tip projectile resulted in higher crimp interchange than yarn extension during the puncture process when compared with penetration with an arch-shape impactor.

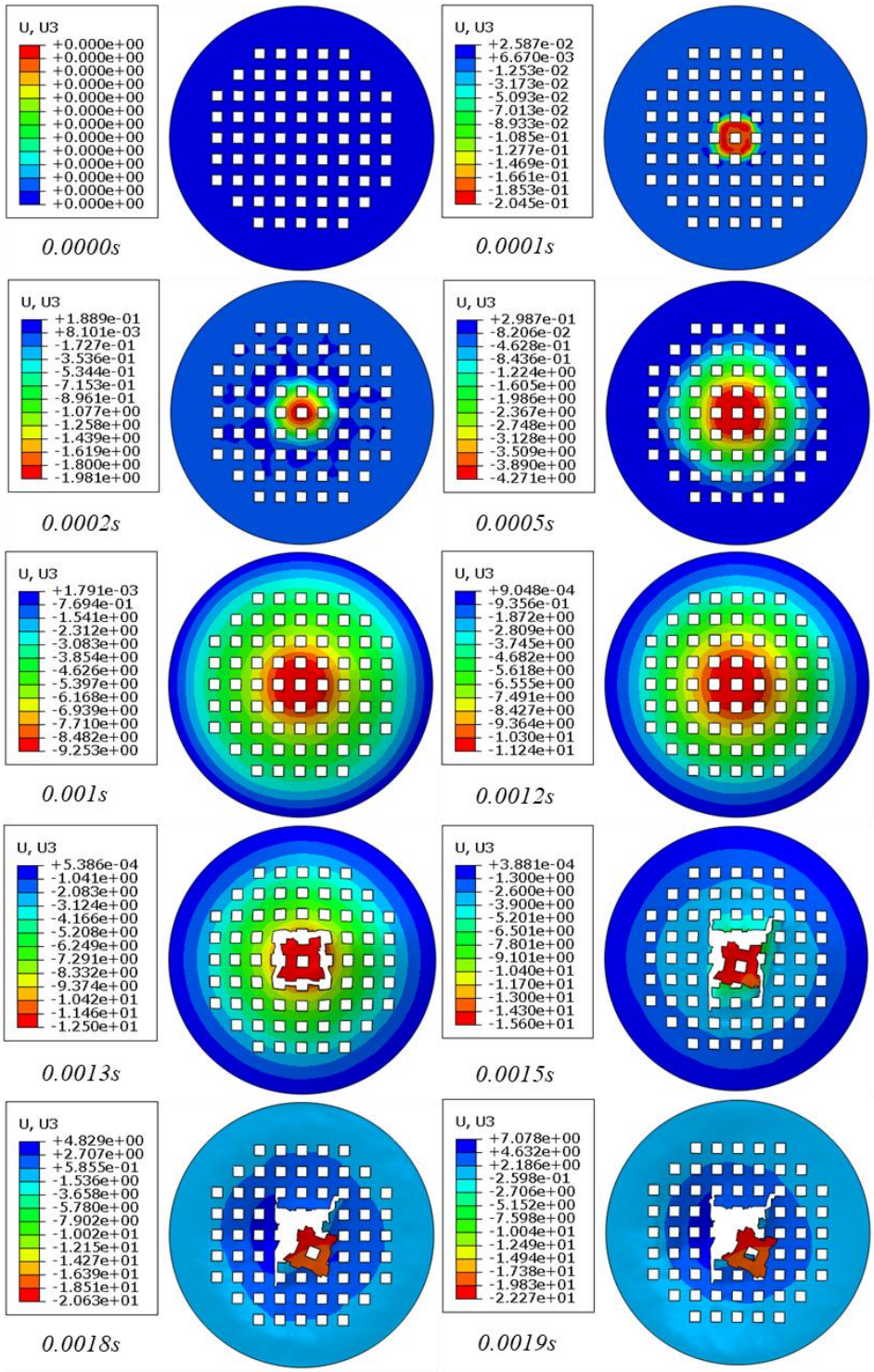

Figure 6-12. Displacement distribution of flat tip penetration

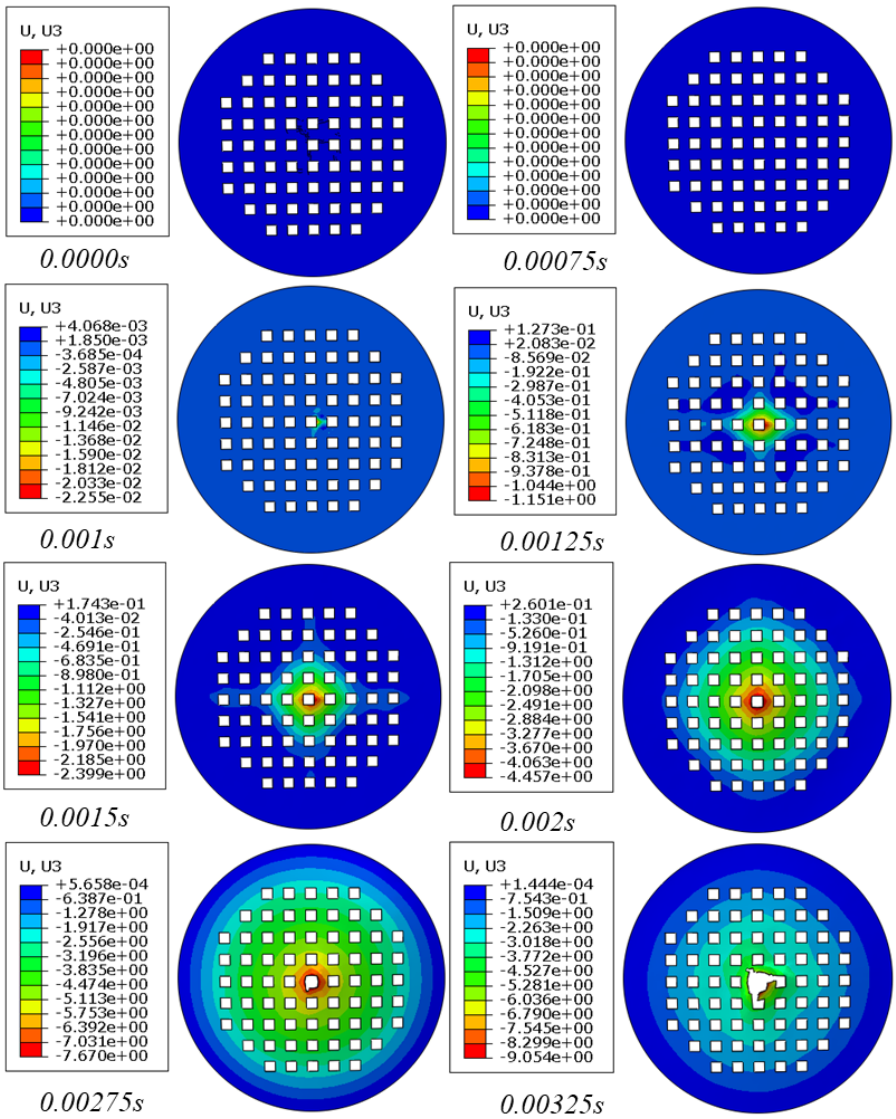

Figure 6-13. Displacement distribution of conical tip penetration

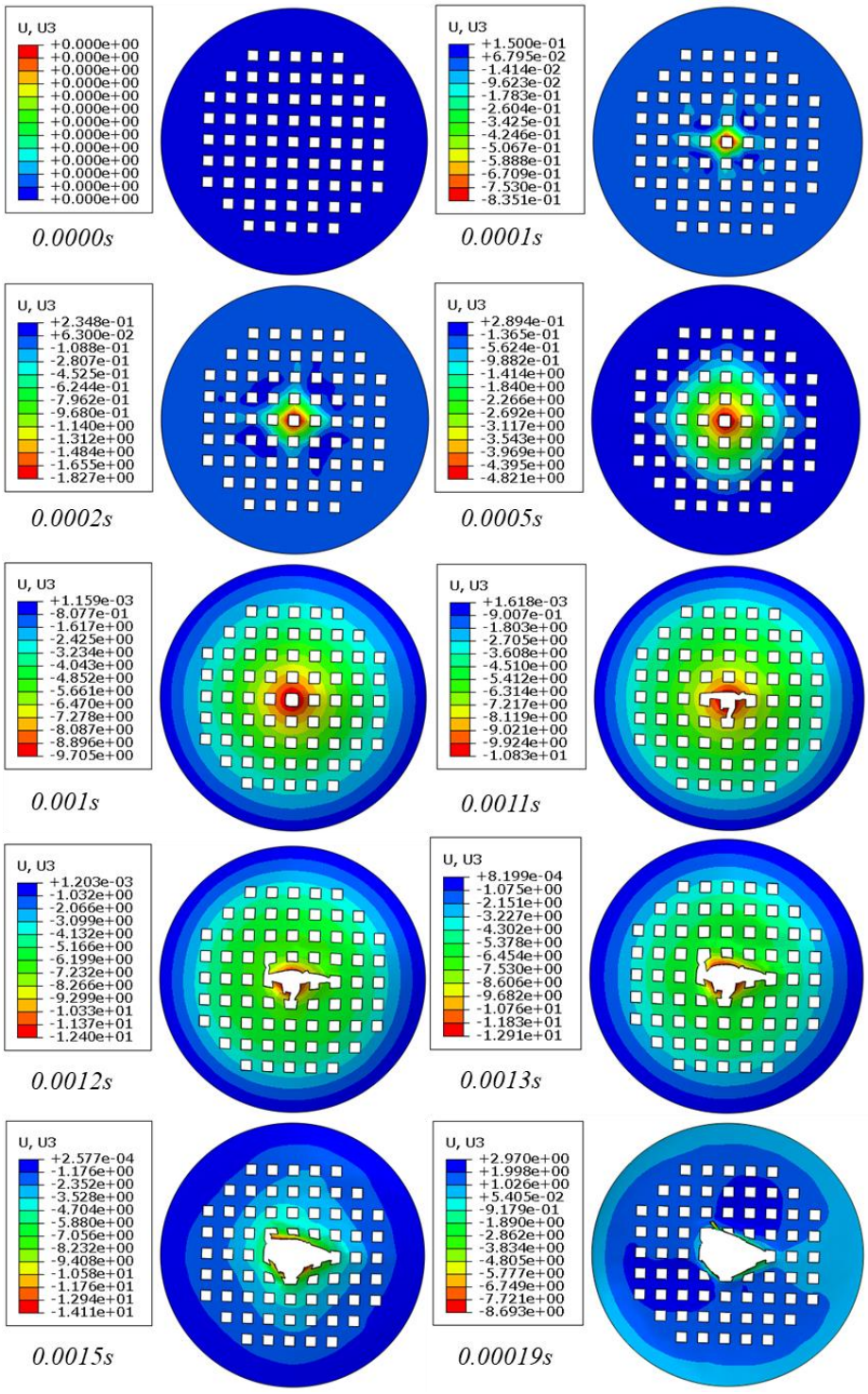

Figure 6-14. Displacement distribution of hemispherical tip penetration

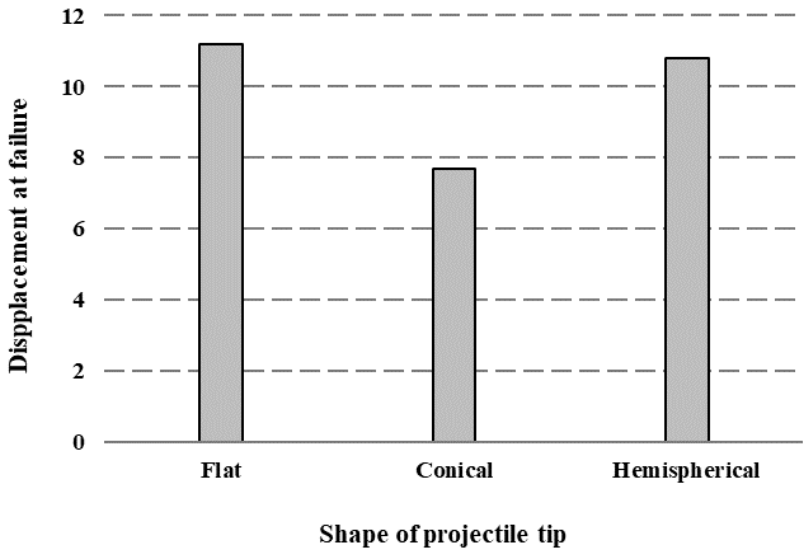

Figure 6-15. Deformation at the failure of fabric

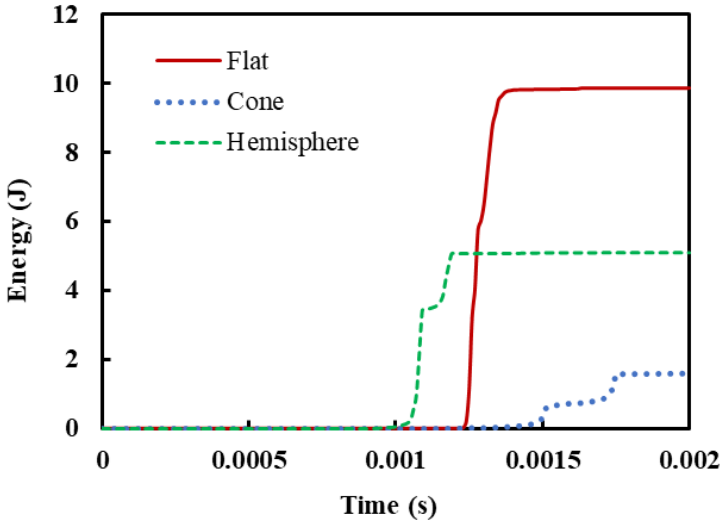

Figure 6-16. Damage dissipation during penetration.

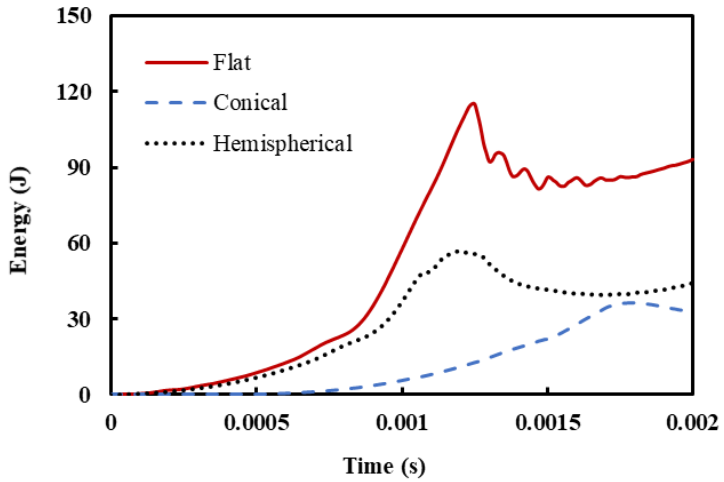

Figure 6-17. Internal strain energy evolution of fabrics with different projectile shapes.

6.4.2 Influence of material density

In this portion of the study, the models are simulated with the same penetration speed, boundary conditions, and same flat-tip projectile. The only variable is material density. The simulation compares the stress distribution during the penetration of fabrics with different material densities. At the same penetration displacement, the stress at yarn breakage increases with higher density (Figure 6-18~ 6-20). The results indicate that fabric with a higher density shows greater resistance to puncture failure. Figure 6-18 and Figure 6-19 display similar yarn breakage modes when flat projectiles sheared the yarns by sharp edges.

Figure 6-21 compares the strain energy evolutions of fabrics with different material densities. The fabric with a density of 1.2 g/cm^3 absorbs the most energy during penetration compared with fabrics with densities of 0.5 and 0.9 g/cm^3. Figure 6-22 shows a similar

damage dissipation during penetration of fabric with densities of 0.9 and 1.2 g/cm^3 which is greater than that of fabric with a density of 0.5 g/cm^3.

Figure 6-20 show that failure appears to be larger for higher density materials. The higher density of a single fiber is stiffer thus the fibers are not easy to slip laterally during penetration by a flat-shape projectile. Energy will distribute on the surface of fabric and lead to a larger damage area.

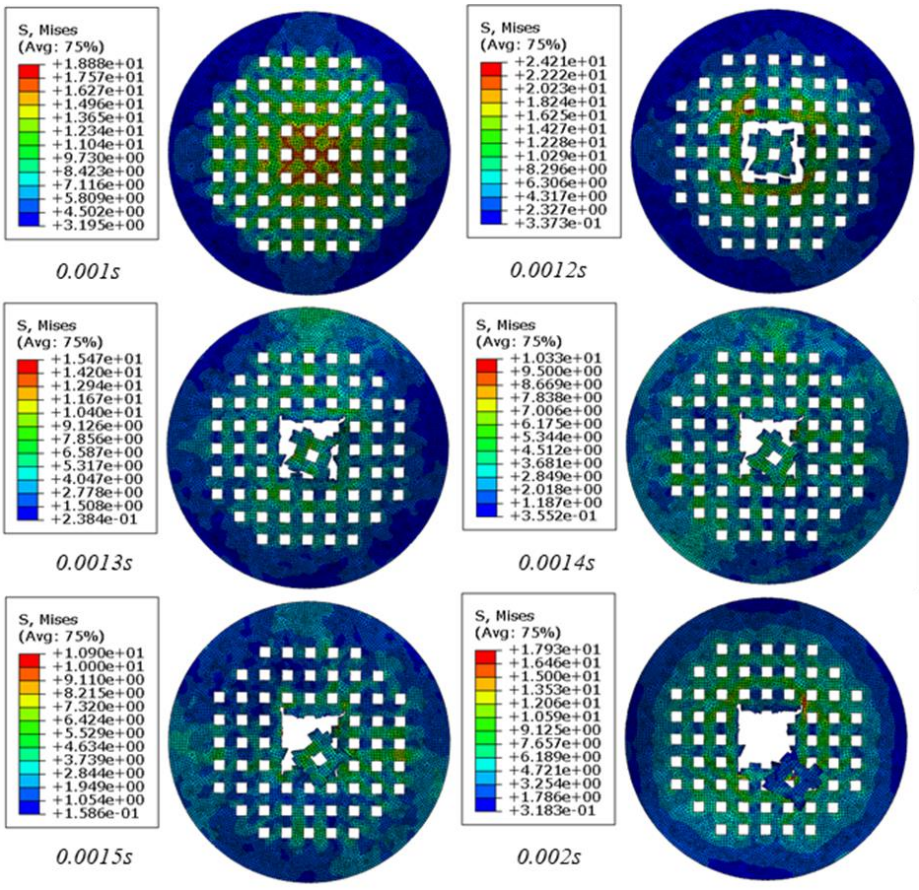

Figure 6-18. Stress distribution of penetration on material with a density of 0.5 g/cm^3.

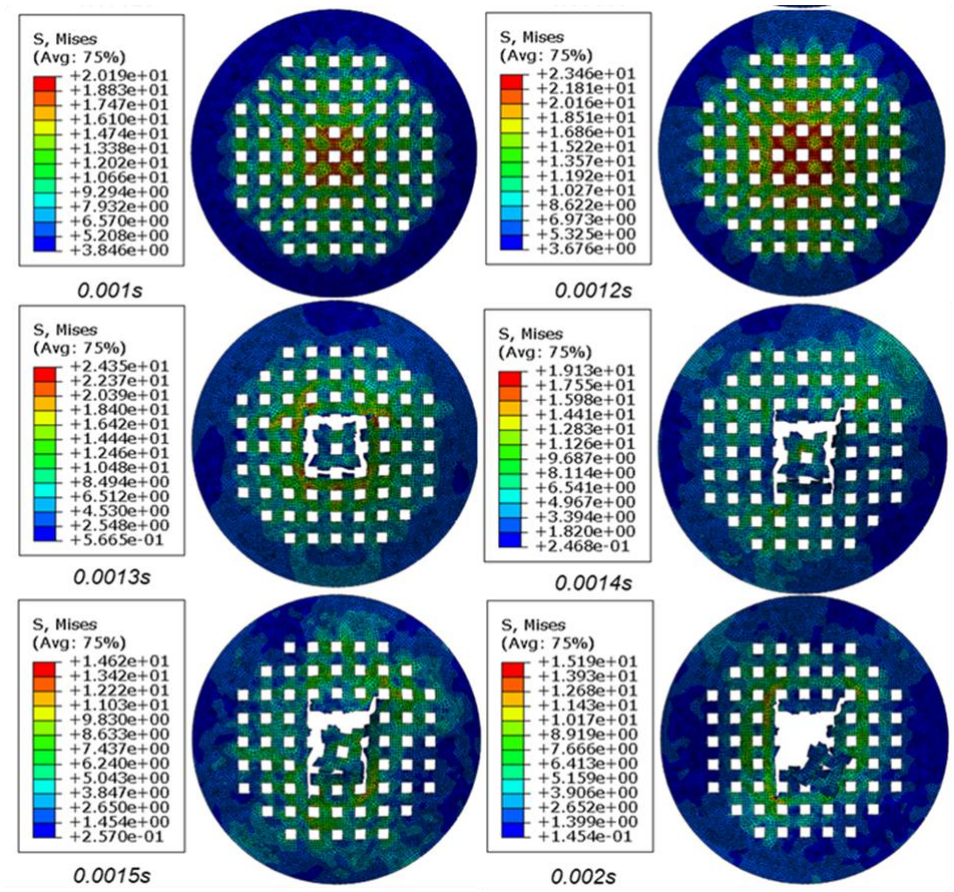

Figure 6-19. Stress distribution of penetration on material with a density of 0.9 g/cm^3.

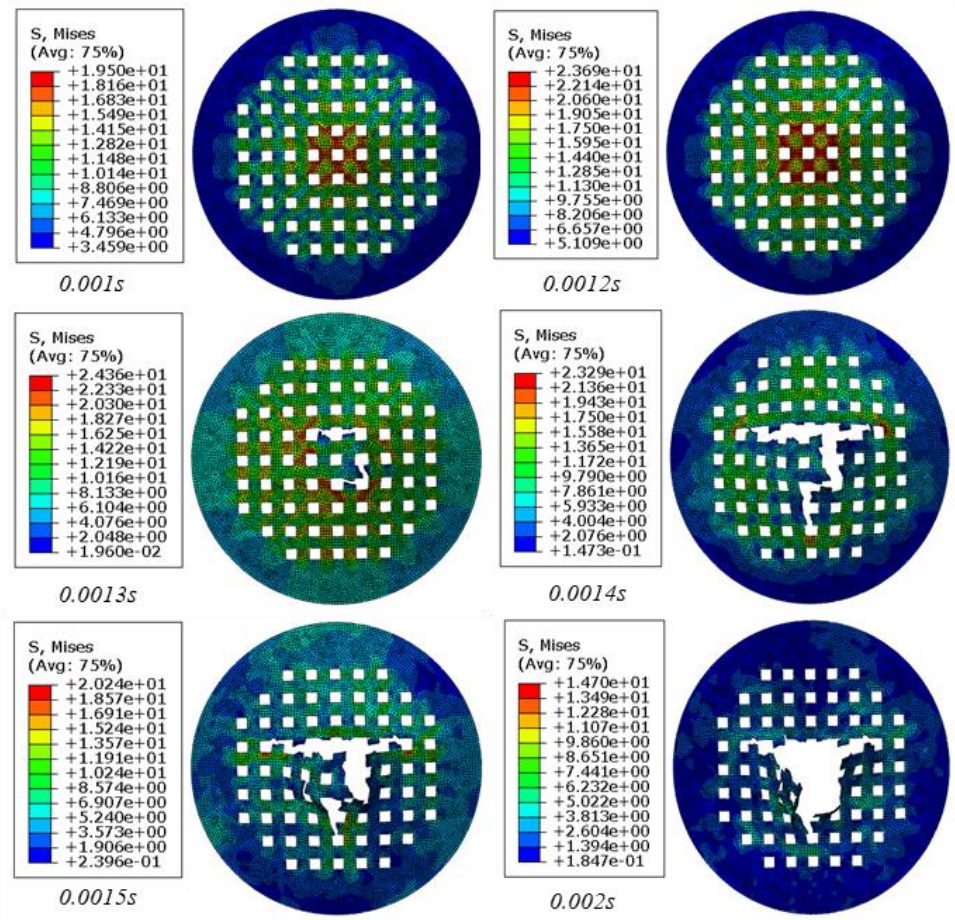

Figure 6-20. Stress distribution of penetration on material with a density of 1.2 g/cm^3.

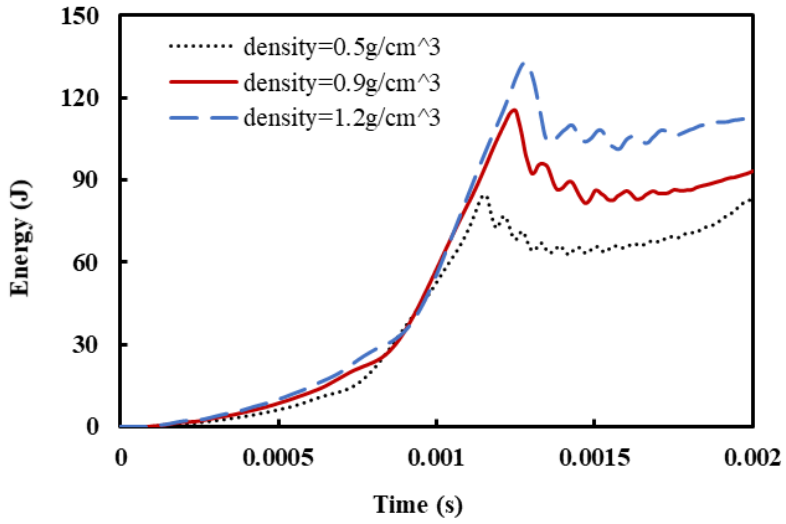

Figure 6-21. Internal strain energy evolution of fabrics with different material densities.

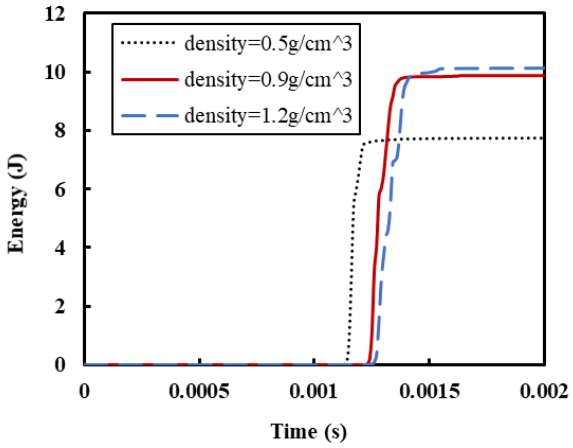

Figure 6-22. Damage dissipation of fabrics with different material densities.

6.4.3 Influence of fabric geometry

In this part of the study, the models are simulated with the same material property, penetration speed, boundary conditions. The only variable is the geometry of the fabric. The simulation compares the deformation during penetration of fabrics with different geometries. Figure 6-23 indicates that fabric with the geometry with a plain weave possesses more strain energy than the fabric with a pyramid matrix.

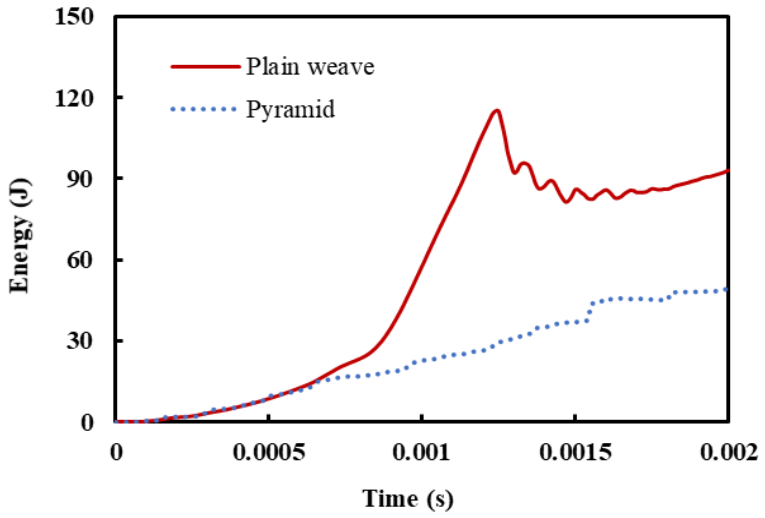

Figure 6-23. Internal strain energy evolution of fabrics with different geometries.

The plain weave fabric displays more puncture resistance than the fabric with pyramid matrix as shown in Figure 6-24. The results can be applied to geotextiles with similar woven structures by changing material properties based on measured Young's modulus and yield strength/strain.

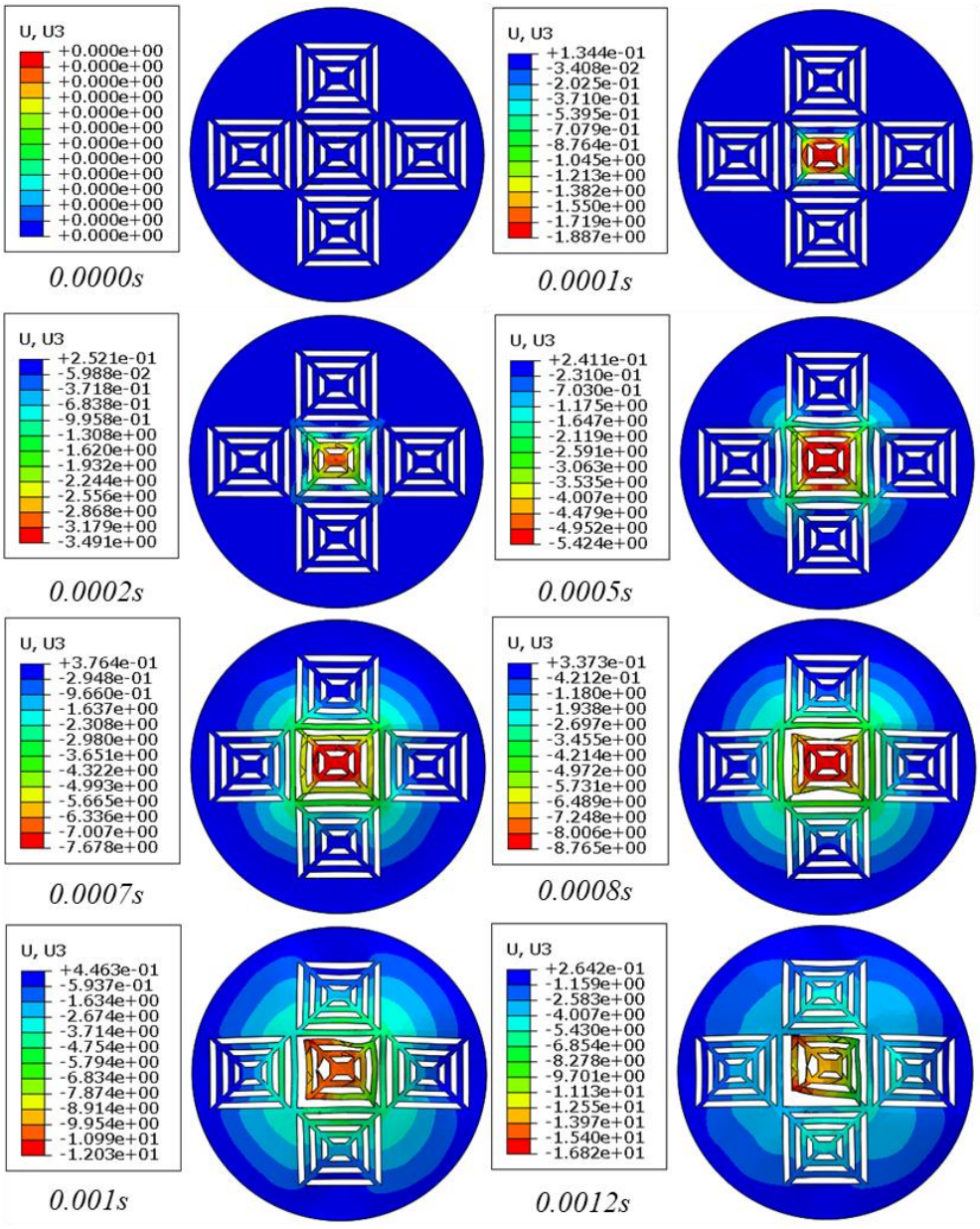

Figure 6-24. Deformation distribution of material with a pyramid geometry

6.4.4 Simulated results of soil and TRM system.

The vertical displacement and corresponding stress distribution of the soil-TRM system model are displayed in Figure 6-25. Figure 6-26 displays the vertical displacement and corresponding stress distribution of the soil only model. Figure 6-27 compares the vertical stress in soil only and TRM-reinforced soil models as a function of depth and shows how the TRM takes over some load from plunger at shallow depth.

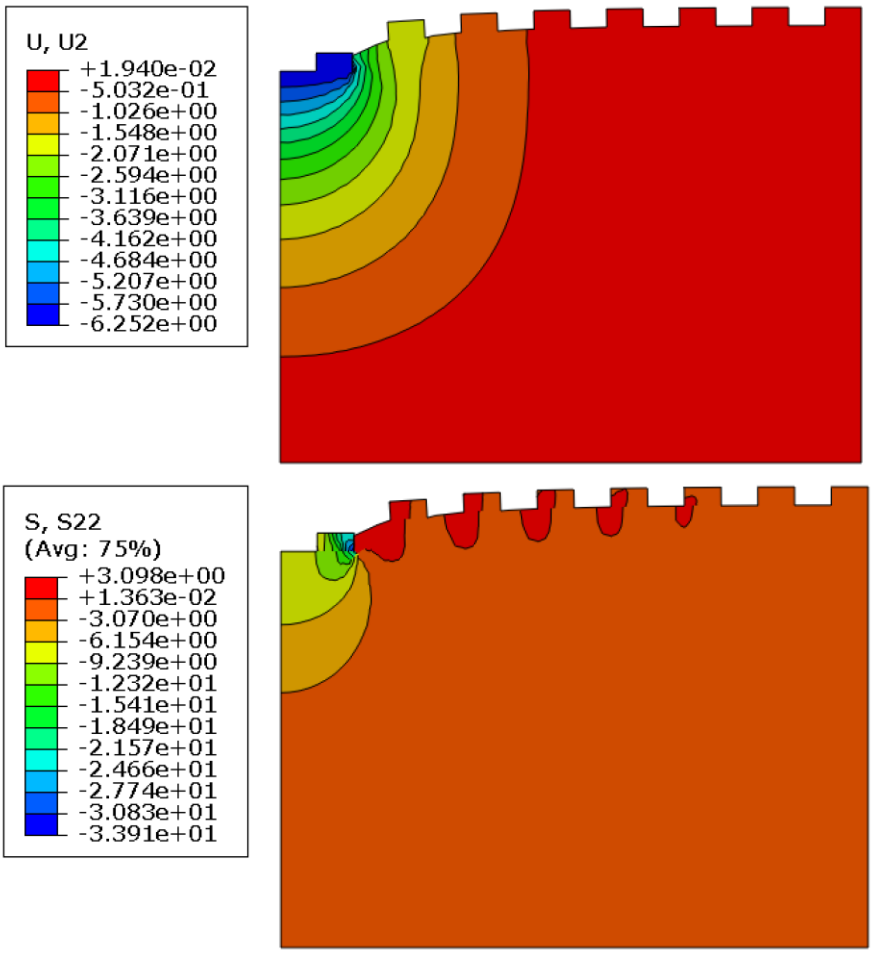

Figure 6-25. Vertical displacement and stress distributions of the soil-TRM system

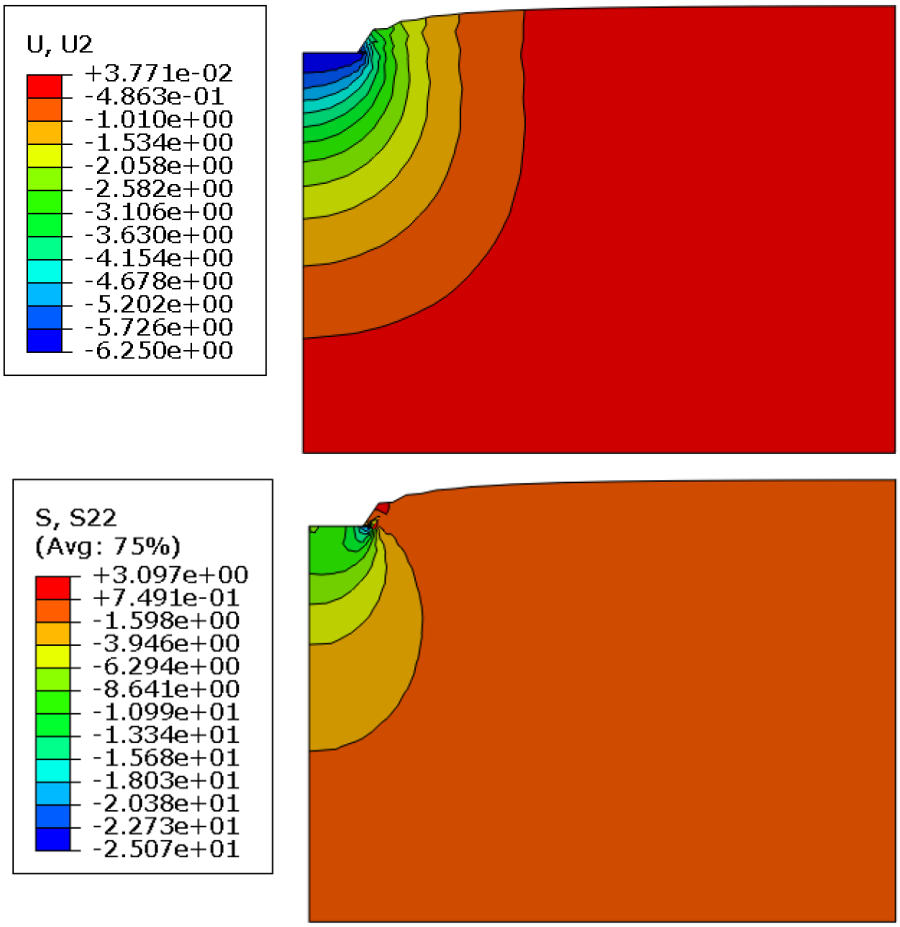

Figure 6-26. Vertical displacement and stress distributions of the soil-only model

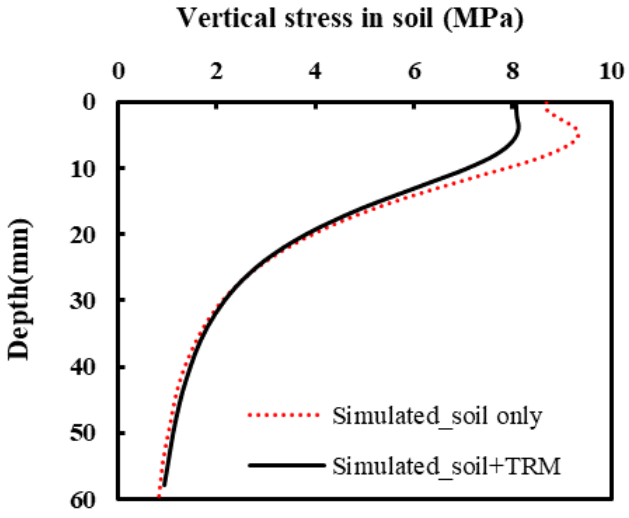

Figure 6-27. Vertical stress distribution in depth at the center of soil specimen with penetration of 6.35 mm (0.25 inches) in simulation.

Figure 6-28 records the force and displacement curves of simulated CBR test of soil only and soil-TRM models and it is observed that forces applied on the soil increase with addition of turf reinforcement mat at a displacement of 2.54mm (0.1 in) thus the CBR value of reinforced soil is also improved.

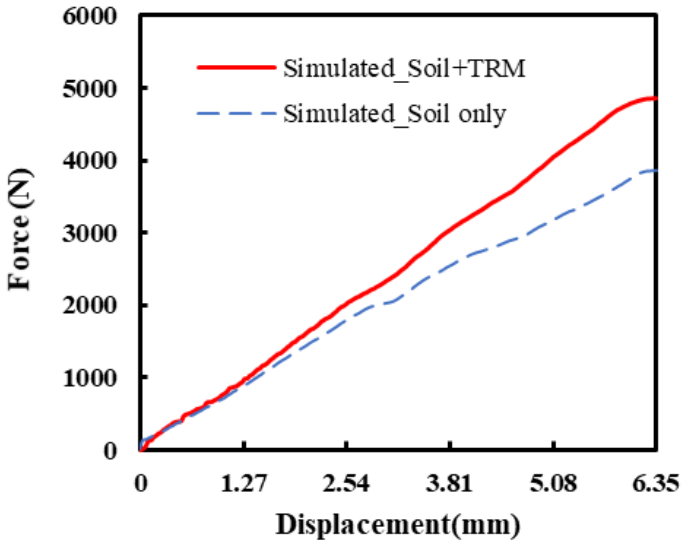

Figure 6-28. Force-displacement curve of simulated specimens

6.5 Conclusion

In this chapter, the static puncture test of TRM and CBR test of the soil-TRM system are simulated using the finite element method. The simulated static puncture test of TRM describes the fabric deformation characteristics considering material density, the shape of the projectile, and geometry of the fabric. The conclusion are summarized as follows:

(1) The puncture process includes the rearrangement and extension of yarns. The yarns break due to shear or tensile damage. The stress is concentrated at the tip of the

projectile. When yarns break, the stress in the yarns suddenly decreased as the fabric surface rebounds.

(2) Woven fabric impacted with a projectile of flat tip yields the highest resistance against puncture.

(3) Fabrics with higher density possess greater resistance to puncture failure which matches the conclusion from experimental results in Chapter 3.

(4) The simulation of the soil-TRM system indicates that TRM can improve the CBR value of soil and it reinforces the soil at a shallow depth.

.

CHAPTER 7. CONCLUSIONS

7.1 Introduction

Over the past decade, the US rolled erosion control product market has developed numerous types of products, especially turf reinforcement mats (TRMs). With the increasing application of TRMs in engineering projects, the damage of products during installation needs to be taken into consideration. Meanwhile, the gap between the classification criteria of TRMs proposed by the Erosion Control Technology Council and those developed by the Department of Transportation in different states cannot be ignored. With updated ASTM standard testing methods, index properties can be measured and bench-scale performance of TRMs in the laboratory can be conducted. The National Transportation Product Evaluation Program (NTPEP) of the American Association of State Highway and Transportation Officials (AASHTO) provides standard testing reports of currently certified products and laboratory tests of products are performed by TRI Inc.

Most of the studies to date have been performed on other RECPs and geotextiles, while there is limited work on turf reinforcement mats. Bolt and Dusynska (2010) pointed out that the loss of geotextiles' strength mainly occurred during installation. They concluded that strength loss due to aging degradation was negligible compared with strength loss due to damage during construction. However, there is no reported data about the measurement of strength loss over the lifetime for TRMs since the degradation time of TRMs is normally over 36 months as shown in the manufacturers' brochure. Compared with other products, the NTPEP provided limited data of index properties and performance tests for TRMs. This thesis compared the index properties and mechanical performance

between seven TRMs and other TRM products in NTPEP reports. This thesis also provides some suggestions on general TRM classification criteria at the end of this chapter.

7.2 Standard Testing for TRMs

7.2.1 Design recommendations based on index property and mechanical performance

Based on collected data from NTPEP in Chapters 2 & 3, the range of index properties for listed TRMs in the current market is summarized in Table 7.1. Except for mass per unit area and thickness, other average values of listed index properties are lower than the average value mentioned in the ASTM standard for woven TRMs. This may be reasonable because the test data collected during this study include some non-woven TRMs, which are composed of more than one material (Table 2.8), while data collected by ASTM is only based on woven TRM specimens. Except for light penetration, the minimum values of other index properties satisfy the GSI (Table 2.3) as well as ECTC (Table 2.2) specified values for the least severe erosion conditions. Due to the wide range of light penetration, it is not clear that light penetration is an appropriate index to categorize TRMs as the GSI specification does. The author suggests removing light penetration as one of the TRM classification criteria.

Table 7.1. Range of TRMs' index properties

Properties	Max	Min	Average	Avg value in ASTM standard
Mass per unit area (g/m^2)	784	271	435	269.43
Thickness (mm)	13.9	3.6	8.5	4.32
Tensile strength-MD (kN/m)	72.9	4.4	19.8	44.47
Tensile strain-MD (%)	48	15	26	29.87
Tensile strength-TD (kN/m)	58.4	2.5	15.7	37.55

Tensile strain-TD (%)	36	15	24	25.93
Light penetration (%)	57	5	18	23.26

In this study, HPTRMs and TRMs are temporarily classified only based on tensile strength. Based on ECTC criteria, TRMs with tensile strength higher than 43.8 kN/m can be classified as high-performance turf reinforcement mats (HPTRMs). Plots of correlation between two index properties are displayed in Figure 7-1~7-4 based on data collected from NTPEP. There is no clear linear relationship between light penetration and mass per unit area for TRMs (Figure 7-1), as well as between tensile strengths in the machine direction and tensile strength cross-machine direction for HPTRMs (blue dash line in Figure 7-3). If ignoring HPTRM classification, it can obtain a weak linear relationship between tensile strengths/strains in the machine and cross-machine directions as shown by the black dotted line in Figures 7-3 and 7-4. It may not be feasible to determine one index value directly based on another measured index value. However, some general trends such as light penetration decrease with increasing mass per unit area and thickness, and ultimate tensile strength in the machine direction is greater than that in the cross-machine direction can be observed.

The index properties listed in Table 7.1 are used for quality control to check material conformance, which can also be set in TRM classification criteria. Mass per unit area affects surface coverage of TRMs on soil and potential for water absorption, which indirectly plays a role in reducing rain splash erosion effects. Thickness influences the ability to reserve water and soil within TRMs' coverage, especially during early vegetation establishment. Light penetration of TRMs affects the soil loss and growth of vegetation. Further work should be conducted to investigate how the geometry structure of TRMs

influences light penetration. Considering the inner correlation between light penetration, mass per unit area, and thickness, the extent of how these three indexes influence erosion control performance can be further studied. Rain splash protection performance of six woven TRMs is evaluated by ASTM Standard D7101 and the NTPEP reported results are displayed in Figure 7-5. Except for TRECS, the other five TRMs has similar weave structures.

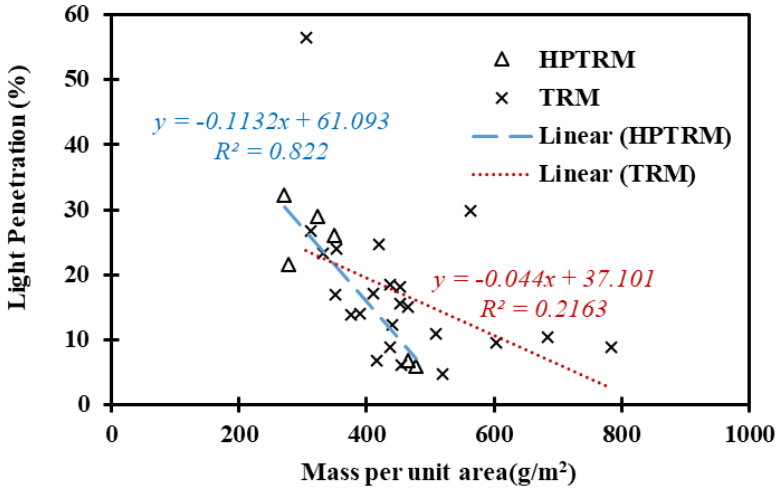

Figure 7-1. Correlation between light penetration and mass per unit area.

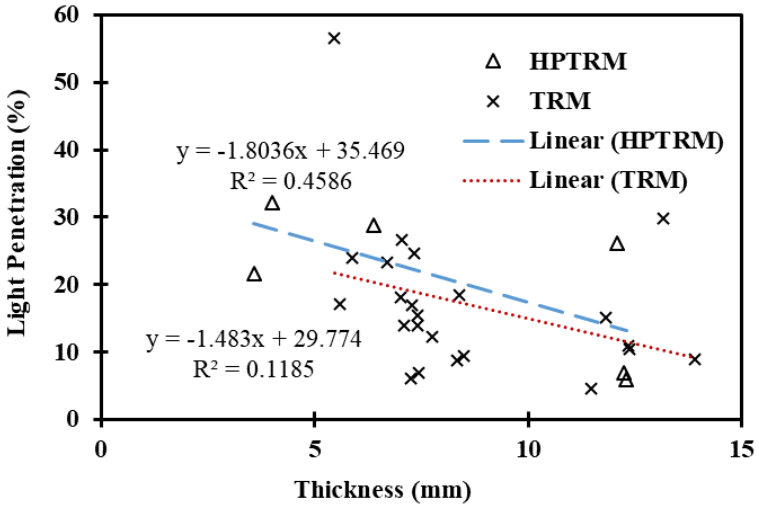

Figure 7-2. Correlation between light penetration and thickness.

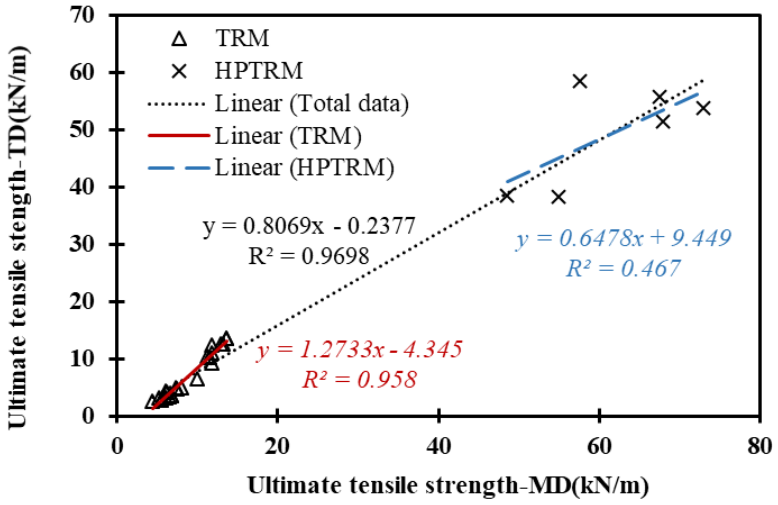

Figure 7-3. Correlation between tensile strength in machine and cross-machine directions.

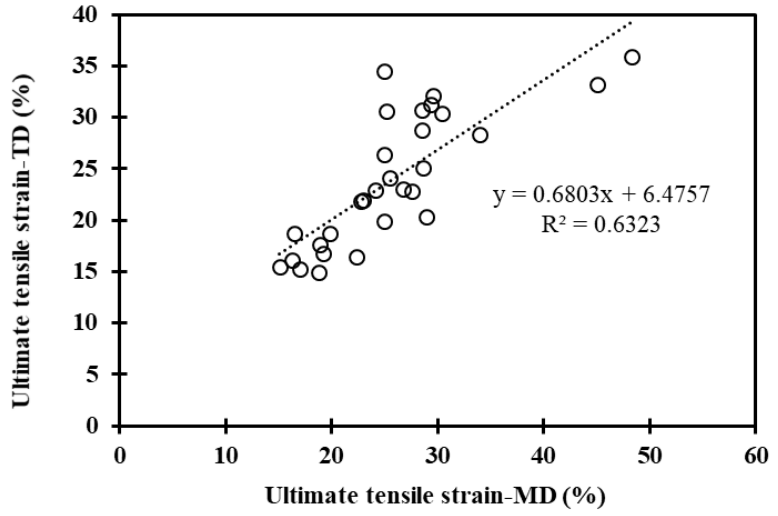

Figure 7-4. Correlation between tensile strain in the machine and cross-machine directions.

Soil loss ratio is calculated by the ratio between mean mass soil loss from TRM protected surface and unprotected soil surface. The lower soil loss ratio indicates a better performance of rain splash protection. The plots for correlation between soil loss ratio and mass per unit area, thickness, and light penetration are presented in Figures 7-6, 7-7 and 7-8. There is a trend that decreasing light penetration and increasing mass per unit area can

lower the soil loss ratio, which indicates the improvement of TRMs' performance in rain splash protection. There needs to be a minimum thickness to withstand the effect from sharp edges of stones. There is no clear trend showing how the thickness of TRMs influences rain splash protection performance. There is no necessary connection between mass per unit area and the thickness of woven material. Mass per unit area of woven material is controlled by the linear density of yarns and density of each fiber, while thickness is determined by fabric layers and weave structure.

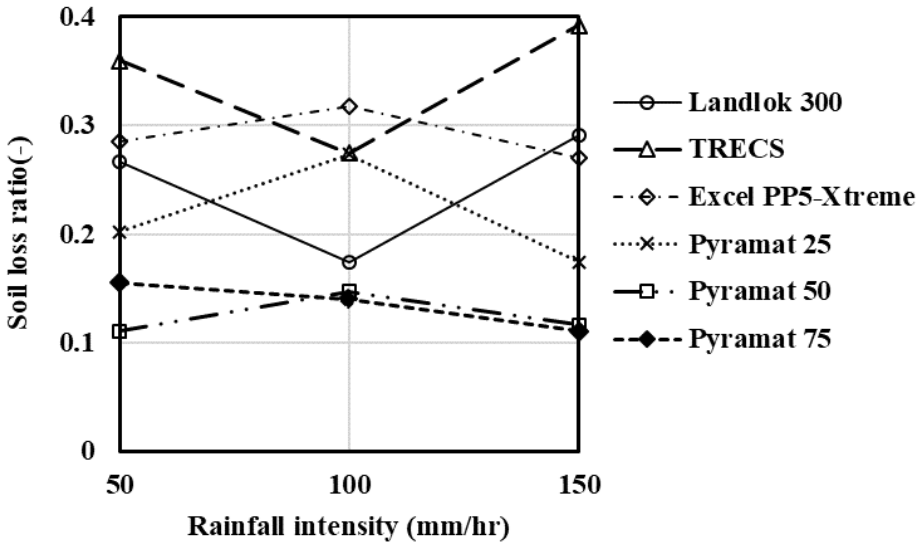

Figure 7-5. Unvegetated TRM ability to protect soil from rain splash.

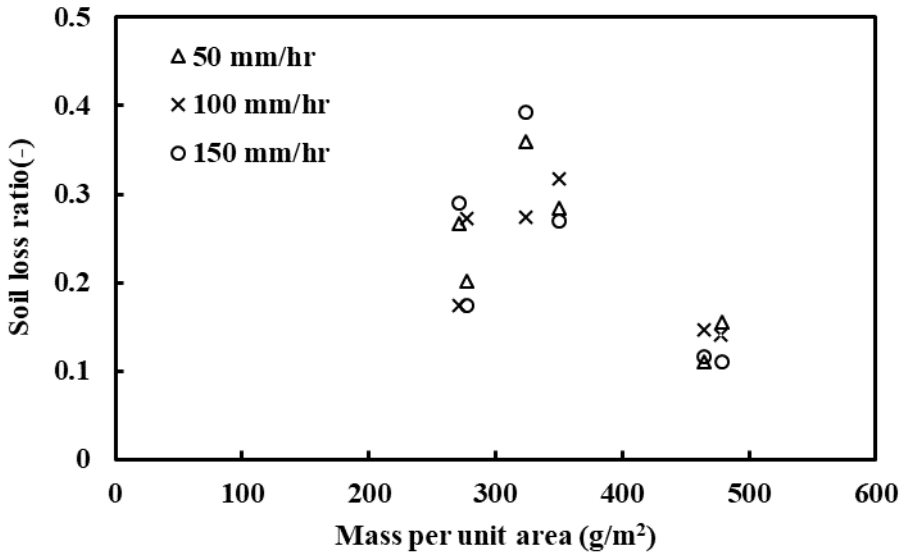

Figure 7-6. Correlation between soil loss ratio and mass per unit area.

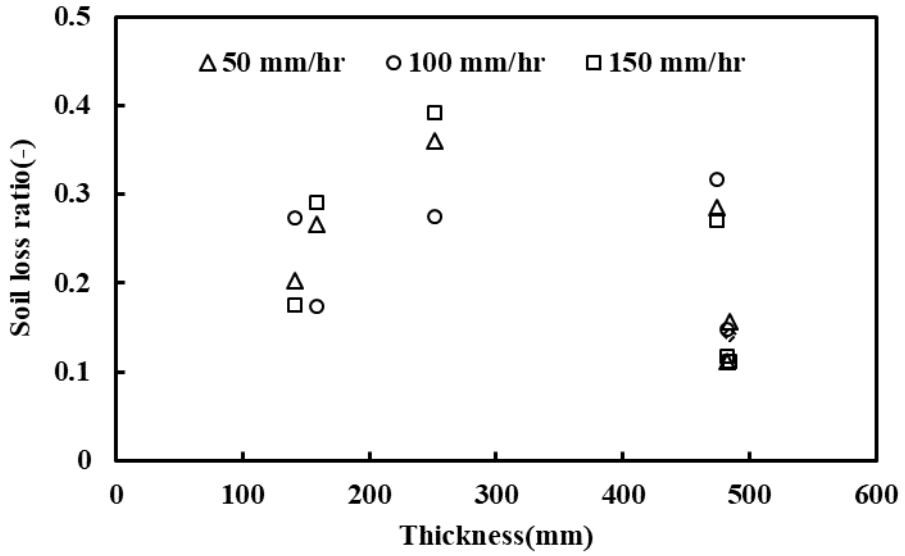

Figure 7-7. Correlation between soil loss ratio and thickness.

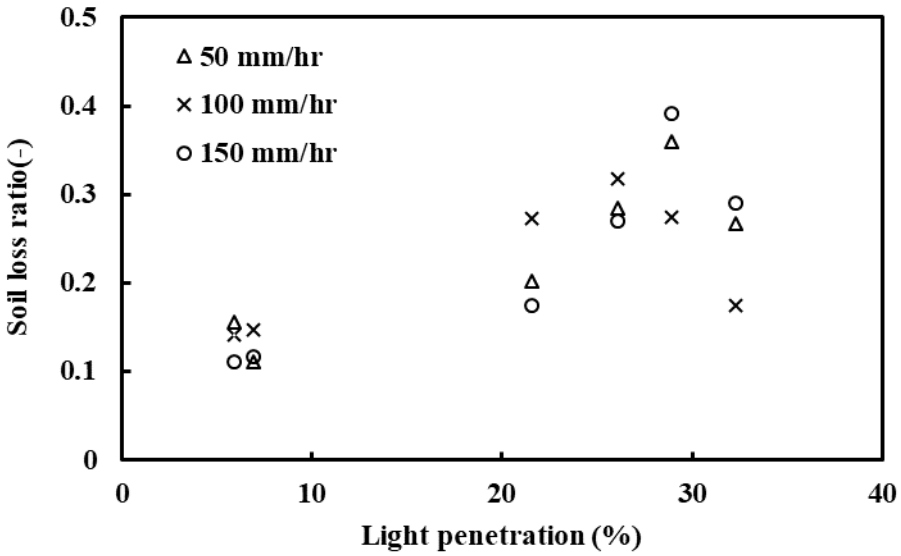

Figure 7-8. Correlation between soil loss ratio and light penetration.

Flexural rigidity (stiffness) and tensile strength do not appear to be important predictors of rain splash protection performance (Smith, 2007), however, these mechanical indexes are important parameters to reflect the material's capacity to resist damage during construction. The average stiffness in the machine direction is greater than that in the cross-machine direction as shown in ASTM D6575 which presents an opposite trend with results in Chapter 3's measurement. This may be accounted for by the geometry difference between woven TRMs and double-net TRMs. To provide a more comprehensive estimation of flexural properties, it is suggested to perform other loop tests besides a standard cantilever test, such as the heart loop test and hanging pear loop test mentioned in Chapter 2.

Puncture resistance of TRMs measured in both dynamic perforation tests and static puncture tests should be displayed in TRM product evaluation reports. Puncture resistance reflects the forces that can cause damage to TRMs during installation and construction.

The application of an appropriate puncture test approach is based on fabric structure and simulated damage in engineering practice (Bolt and Dusynska, 2010). Static puncture test indicates the capability of bearing slow puncture initiation while dynamic perforation test simulates damage caused by a sudden drop of a sharp or angular shaped object such as aggregate on coverage materials (Bolt and Dusynska, 2010). There is no clear correlation between static puncture resistance and mean hole diameter in Figure 7-9 based on measured data in Chapter 3. However, static puncture resistance is linearly correlated with tensile strength (Figure 3-35). Thus, reporting both test values in product evaluation is recommended.

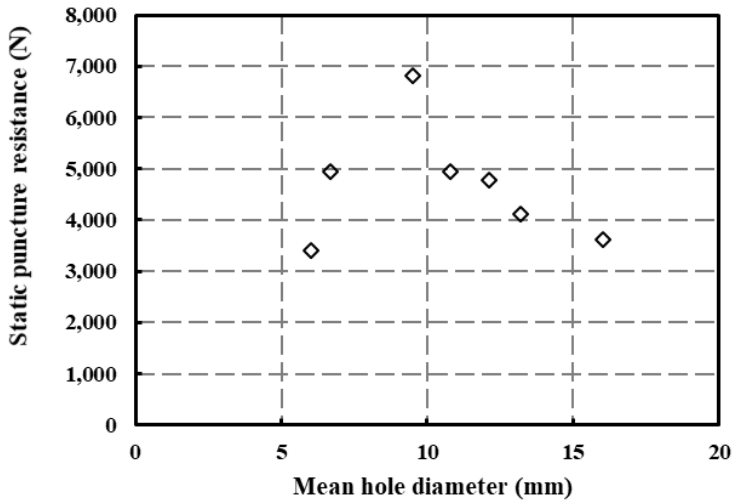

Figure 7-9. Correlation between static and dynamic puncture resistance

Index test values do not reflect material performance on site because they do not consider field conditions, such as characteristics of armor stone, the number of drops on specimens, drop height, etc. Before w deciding to apply the TRM material including geotextile in specific locations, it is suggested to conduct field tests such as drop rock tests to assess geotextile performance (Cheah et al., 2015). The thickness change of TRMs

during the tensile strength test should also be considered because too much stretching will reduce thickness and puncture resistance capability.

In conclusion, it is recommended that multiple index properties as well as erosion protection performance factors including mass per unit area, thickness, flexural rigidity, light penetration, tensile strength/strain in the machine and cross-machine directions, static puncture resistance as well as mean hole diameter for dynamic perforation test should be presented in product datasheets. It is also necessary to determine maximum CBR displacement, minimum thickness, minimum tensile strength, and maximum tensile extension for quality control of TRMs.

7.2.2 ASTM standard index test accuracy on TRMs

The standard deviation of ASTM standard index test results is used to check material uniformity. A larger standard deviation of the ASTM standard index indicates less uniformity in material manufacturing. Table 7.2 summarizes the reproducibility standard deviation mentioned in ASTM standards. Reproducibility standard deviation is calculated by test results from different operators applying the same test approach in different laboratories. Based on data collected from NTPEP reports, plots of the standard deviation of measured indexes for six woven TRMs are displayed in Figure 7-10 ~7-16. The standard deviation of each index is calculated from ten specimens in each test. Compared with standard deviation values listed in Table 7.2, TRECS, Pyramat 50, and Pyramat 75 show higher standard deviations of mass per unit area (Figure 7-10). All six products present less tensile strength/strain in the machine and cross-machine directions (Figure 7-11~7-14). Except for Pyramat 25, the other five products display a higher standard deviation of the

thickness (Figure 7-15). Landlok 300 shows a much higher standard deviation of light penetration (Figure 7-16).

Table 7.2. Reproducibility standard deviation of TRMs' index properties

Properties	Woven TRMs	Reference
Mass per unit area (g/m^2)	7.05	ASTM D6475
Thickness (mm)	0.36	ASTM D6525
Tensile strength-MD (kN/m)	9.89	ASTM D6818
Tensile strain-MD (%)	4.08	ASTM D6818
Tensile strength-TD (kN/m)	14.32	ASTM D6818
Tensile strain-TD (%)	4.33	ASTM D6818
Light penetration (%)	1.89	ASTM D6567

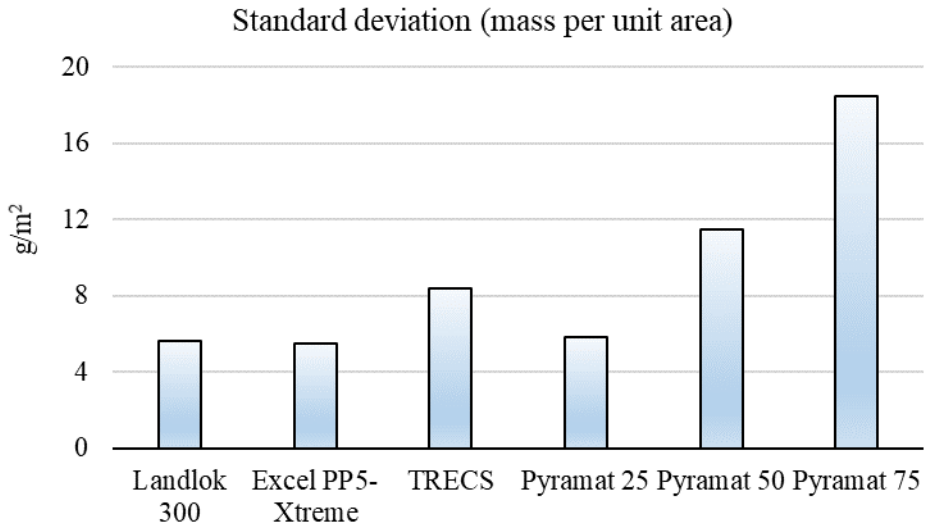

Figure 7-10. The standard deviation of mass per unit area for six woven TRMs

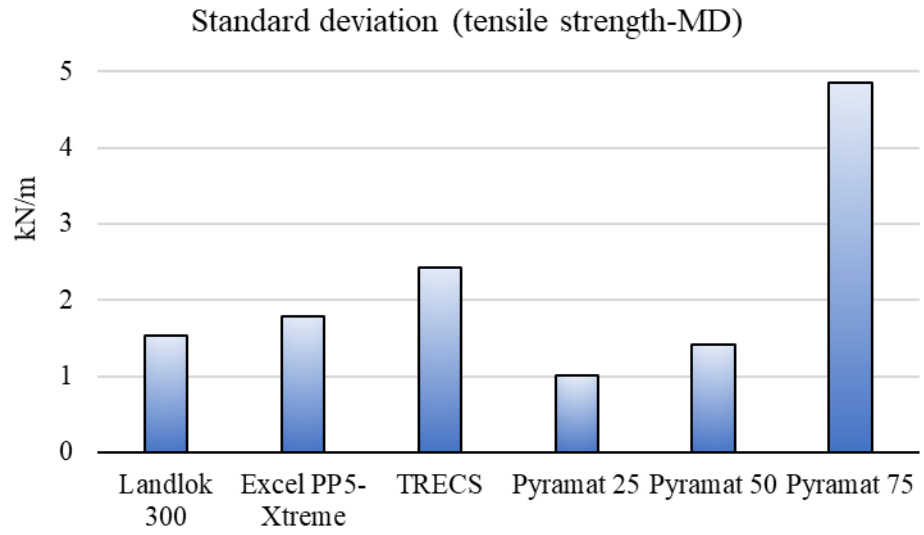

Figure 7-11. Standard deviations of tensile strength in machine direction for six woven TRMs.

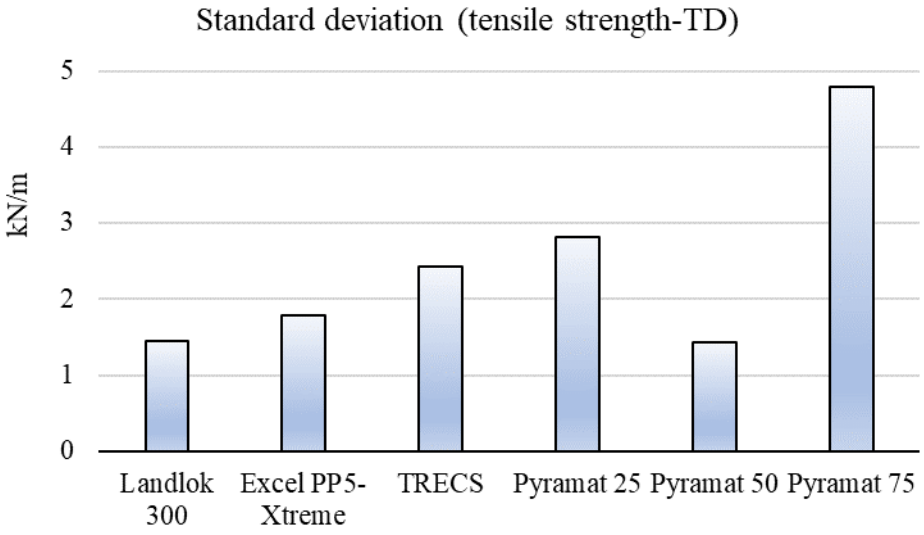

Figure 7-12. Standard deviations of tensile strength in cross-machine direction for six woven TRMs.

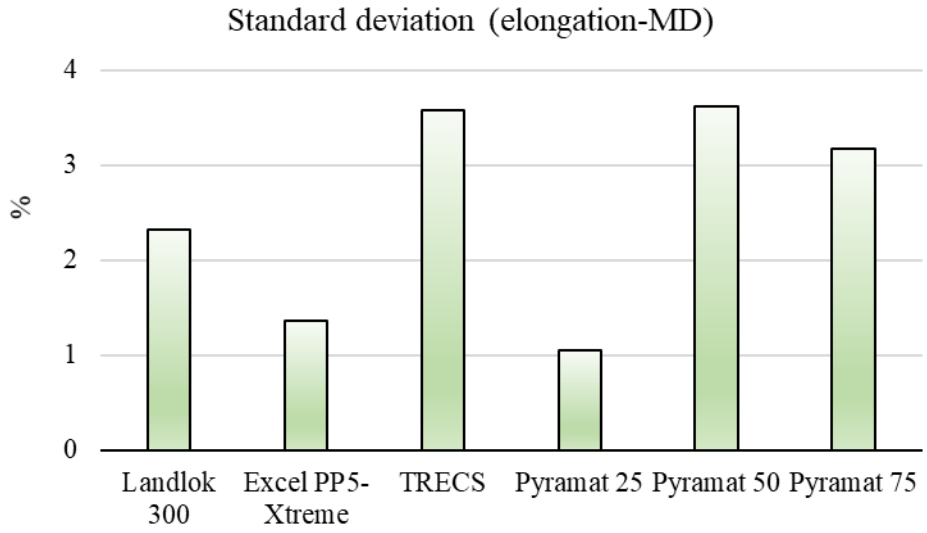

Figure 7-13. Standard deviations of elongation in machine direction for six woven TRMs.

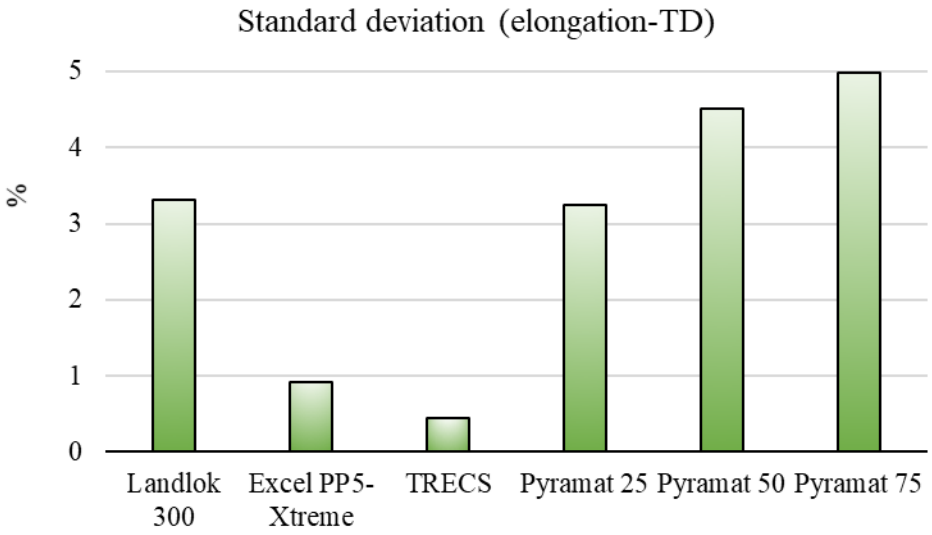

Figure 7-14. Standard deviations of elongation in cross-machine direction for six woven TRMs.

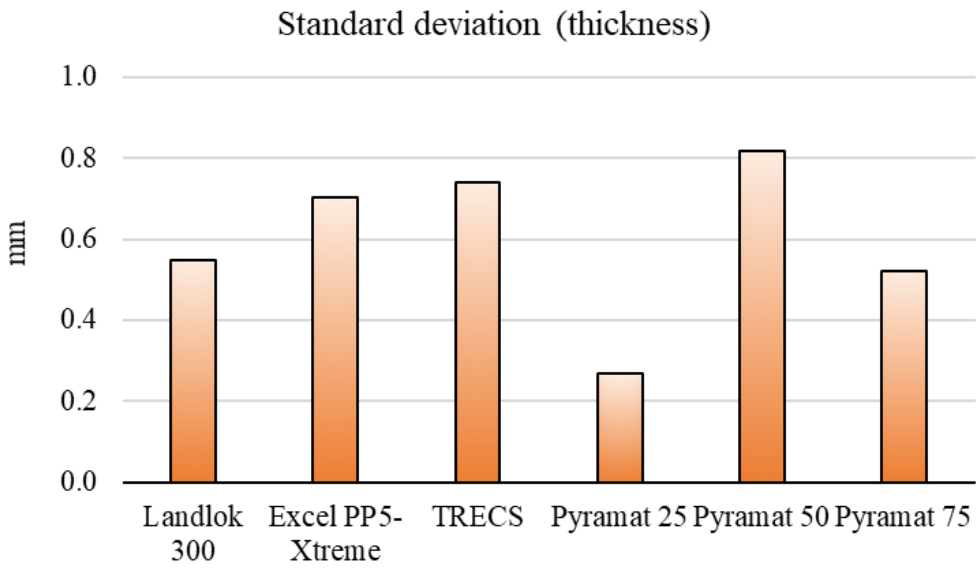

Figure 7-15. Standard deviations of thickness for six woven TRMs.

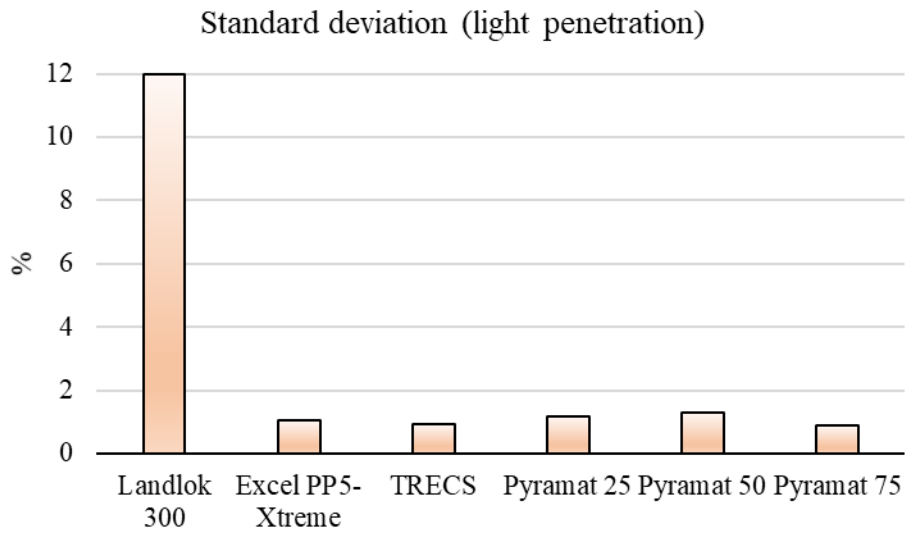

Figure 7-16. Standard deviations of light penetration for six woven TRMs.

7.3 Categorization of TRMs

Burns et al (2013) recommended considering slope steepness, time to establish the vegetation, UV degradation, and product material (eg. straw, wood fiber, etc.) as criteria to select appropriate RECP materials. As a reference in selecting appropriate TRM products,

we can consider the similar aspects but with further detailed criteria as ECTC recommendation, such as allowable vegetated and unvegetated shear stresses, tensile strength, and elongation. Table 7.3 compares unvegetated allowable shear stresses for ECTC and GDOT classifications.

Table 7.3. Unvegetated allowable shear stresses

Classes	ECTC classification	GDOT classification
1/A	> 2 psf	> 2 psf
2/B	> 2 psf	> 4 psf
3/C	> 2 psf	> 6 psf
4/D	> 2 psf	> 8 psf
5/E	> 2 psf	> 10 psf
6/F	> 2 psf	> 12 psf

ECTC classification provided the same unvegetated allowable shear stress for all categories of TRMs but different vegetated allowable shear stresses for each category of TRMs as shown in Table 2.2 in Chapter 2. The common requirement for providing unvegetated shear stress of at least 2.0 psf for all types of TRMs is not appropriate, because TRMs should improve the protection of soil surface before the establishment of vegetation. Thus, it is recommend that classifying categories of TRMs considering different unvegetated permissible shear stresses as outlined in the GDOT report and Burns et al. (2011) as well as retaining the other requirements mentioned in ECTC classification. The proposed classification of TRMs is shown in Table 7.4.

Table 7.4. Suggested classification of TRMs

Type	Application and standard specification
5.A	A TRM designed for use on geotechnically stable slopes up to 1:1 (H:V), provide unvegetated shear stress of at least 2.0 lbs/ft^2 (96Pa), and vegetated shear stress of at least 6.0 lbs/ft^2 (287Pa). Tensile strength value at the time of manufacture is at least 150 ×150 lbs/ft (2.2×2.2 kN/m). Minimum UV stability is 80% at 500 hrs. Static puncture strength at the time of manufacture is at least 2000 N. Maximum hole diameter of dynamic perforation test at the time of manufacture should be less than 25 mm.
5.B	A TRM designed for use on geotechnically stable slopes up to 1:1 (H:V), provide unvegetated shear stress of at least 4.0 lbs/ft^2 (192Pa), and vegetated shear stress of at least 8.0 lbs/ft^2 (383Pa). Tensile strength value at the time of manufacture is at least 175 ×175 lbs/ft (2.6×2.6 kN/m). Minimum UV stability is 80% at 500 hrs. Static puncture strength at the time of manufacture is at least 2000 N. Maximum hole diameter of dynamic perforation test at the time of manufacture should be less than 25 mm.
5.C	A TRM designed for use on geotechnically stable slopes up to 0.5:1 (H:V), provide an unvegetated shear stress of at least 6.0 lbs/ft^2 (287Pa), and vegetated shear stress of at least 10.0 lbs/ft^2 (479Pa). Tensile strength value at the time of manufacture is at least 200 ×200 lbs/ft (2.9×2.9 kN/m). Minimum UV stability is 80% at 1000 hrs. Static puncture strength at the time of manufacture is at least 2000 N. Maximum hole diameter of dynamic perforation test at the time of manufacture should be less than 25 mm.
5.D	A TRM designed for use on geotechnically stable slopes up to 0.5:1 (H:V), provide unvegetated shear stress of at least 8.0 lbs/ft^2 (383Pa), and vegetated shear stress of at least 12.0 lbs/ft^2 (575Pa). Tensile strength value at the time of manufacture is at least 325 ×225 lbs/ft (4.8×3.3 kN/m). Minimum UV

stability is 80% at 1000 hrs. Static puncture strength at the time of manufacture is at least 2500 N. Maximum hole diameter of dynamic perforation test at the time of manufacture should be less than 25 mm.

5.E A TRM designed for use on geotechnically stable slopes up to 0.5:1 (H:V), provide unvegetated shear stress of at least 10.0 lbs/ft^2 (479Pa), and vegetated shear stress of at least 12.0 lbs/ft^2 (575Pa). Tensile strength value at the time of manufacture is at least 1500 ×1500 lbs/ft (21.9×21.9 kN/m). Minimum UV stability is 90% at 1000 hrs. Static puncture strength at the time of manufacture is at least 3000 N. Maximum hole diameter of dynamic perforation test at the time of manufacture should be less than 20 mm.

5.F A high-performance TRM designed for use on slopes up to 0.5:1 (H:V), provide unvegetated shear stress of at least 12.0 lbs/ft^2 (575Pa), and vegetated shear stress of at least 14.0 lbs/ft^2 (670Pa). Tensile strength value at the time of manufacture is at least 3000 ×3000 lbs/ft (43.8×43.8 kN/m). Minimum UV stability is 80% at 3000 hrs. Static puncture strength at the time of manufacture is at least 4000 N. Maximum hole diameter of dynamic perforation test at the time of manufacture should be less than 15 mm.

7.4 Main contributions

Potential damage on the turf reinforcement mat can lead to failure of its function in erosion protection. Standard tests such as static puncture test and dynamic perforation test are applied to model material damage from installation or construction of TRMs. In this study, a set of experimental tests are performed on turf reinforcement mats to evaluate the puncture resistance of seven TRMs.

Chapter 3 evaluates turf reinforcement mats through basic index property tests and discusses the relationship between index properties and puncture resistance of TRM. Higher mass per unit area shows greater static puncture strength and extension for TRMs.

There is no strong relationship between stiffness and static puncture resistance. The tested and collected index properties of TRMs are summarized and standard index property testing methods are evaluated. There are some general trends such as light penetration decreases with increasing mass per unit area and thickness. Basic criteria of TRM classification are also proposed considering properties such as tensile strength, unvegetated, and vegetated shear stresses.

Chapter 4 studied young plant root's interaction with turf reinforcement mats. Although it is not clear about the correlation between light penetration of TRMs and measured plant seed germination enhancement, TRM can reduce 40.3~78.0% water evaporation thus maintaining soil moisture during seed germination. The pullout test results of Dandelion and Ryegrass show that TRM coverage improves the initial pullout modulus of plant roots. The observation from the pullout tests also indicates that young plants with fibrous roots have higher pullout resistance and initial pullout modulus compared to plants with taproots.

Chapter 5 summarized modified CBR tests to analyze soil reinforcement by turf reinforcement mats. The contribution of TRM reinforcement to increasing the CBR value of soil at 0.1 inches is up to ~60% compared with soil only specimens. The effect of soil reinforcement diminishes when penetration reaches 0.2 inches. Pyramat Green displays the greatest improvement in CBR value among the four tested TRMs. There is no strong relationship between tensile strength and CBR improvement while TRMs reinforce soil more with their higher puncture resistance and mass per unit area.

Chapter 6 simulated static puncture test and CBR test of soil-TRM system performance using the finite element method. The modeling results indicate that TRM model impacted with a projectile of flat tip yields the highest resistance against puncture compared with those impacted by projectiles of conic and hemispheric tips. The results also suggest that TRM with a higher density is more difficult to penetrate thus possesses greater puncture resistance. The vertical stress-depth curve of the simulated CBR penetration of soil-TRM system shows that TRM reinforces the soil at shallow depth and this conclusion matches the experimental results in Chapter 5.

7.5 Recommendations for Future Work

This study can be expanded by performing additional laboratory testing. Plant uprooting resistance over soil-TRM composites can be investigated during water flow with different flow velocities. It is necessary to study micro mechanisms of sediment entrapment by plant root hair in soil stabilization especially in water flow. Other mechanical tests such as direct shear test and cyclic load test can be conducted to measure shear strength of plant-TRM-soil systems and discuss the characteristics of soil-TRM composites under repeated loads.

Further work can also be focused on the development of sustainable turf reinforcement mat materials as well as their long-term environmental effects because current non-degradable materials could become environmental threats. Previous studies indicate that the composite RECP materials may lose 50% strength after 36 months' service (Smith, 2007). This thesis only explored the test methods and mechanical properties of TRMs before construction. However, performance testing of TRMs at different lifetime

after being put into use should be investigated. The change of puncture resistance, ultimate tensile strength, and percentage of elongation at failure considering aging effects can be recorded. We can also study the elongation recovery rate after static puncture and dynamic perforation tests. Besides, Scanning Electron Microscopy (SEM) can be applied to study the micro-mechanisms of repeated tension fatigue for TRMs. Other bending rigidity testing approaches besides cantilever methods should be studied and applied to standardized testing. Since vegetation establishment is the ultimate solution for erosion control, the moisture capture ability of current TRM fibers can also be explored.

APPENDIX A. STIFFNESS TEST RESULTS

Table A.1. Flexural Rigidity: Machine Direction

Material	Flexural Rigidity, *G* (mg-cm), Machine Direction						
	1*	2*	3*	4*	Avg	STD DEV	COV
Pyramat(Green)	229,913	225,915	235,999	221,963	228,448	5,187	0.0227
Pyramat(Tan)	210,183	164,265	210,183	210,183	198,703	19,883	0.1001
Landlok 300	151,125	154,300	186,343	173,594	166,340	14,398	0.0866
Landlok 3000G	212,463	205,516	210,711	193,727	205,604	7,318	0.0356
T-RECS	193,721	256,539	247,356	234,871	233,122	24,013	0.1030
Excel PP5-Xtreme	219,799	230,292	225,005	246,649	230,436	10,069	0.0437
VMax W3000	229,675	257,551	246,577	264,289	249,523	13,087	0.0524

*Average of four tests

Table A.2. Flexural Rigidity: Cross-Machine Direction

Material	Flexural Rigidity, *G* (mg-cm), Cross-Machine Direction						
	1*	2*	3*	4*	Avg	STD DEV	COV
Pyramat(Green)	595,312	638,003	654,019	569,162	614,124	33,680	0.0548
Pyramat(Tan)	247,494	242,165	230,030	254,719	243,602	9,014	0.0370
Landlok 300	209,196	212,472	214,043	231,683	216,881	8,741	0.0403
Landlok 3000G	350,086	361,225	339,778	333,810	346,225	10,436	0.0301
T-RECS	1,574,560	1,676,388	1,624,943	1,695,957	1,642,962	47,247	0.0288
Excel PP5-Xtreme	859,927	862,066	853,531	874,975	862,625	7,791	0.0090
VMax W3000	2,319,988	2,215,557	2,187,630	2,262,628	2,246,451	50,209	0.0224

*Average of four tests

APPENDIX B. STATIC PUNCTURE TEST RESULTS

Table B.1. Test Results for Puncture Strength of Seven HPTRMs

Sample	Maximum Load (N)					
	1	2	3	Average	STD DEV	COV
Pyramat(Green)	6,928	6,165	7,383	6,825	615	0.09
Pyramat(Tan)	4,251	4,219	3,894	4,121	198	0.05
Landlok 300	3,229	3,903	3,726	3,620	350	0.10
Landlok 3000G	5,350	4,669	4,810	4,943	359	0.07
T-RECS	3,281	3,430	3,535	3,415	128	0.04
Excel PP5-Xtreme	4,711	4,930	4,684	4,775	135	0.03
VMax W3000	4,404	4,931	5,490	4,941	543	0.11

Table B.2 – Photos of Specimens After Failure – Static Penetration

Material	Specimen after Failure
Pyramat(Green)	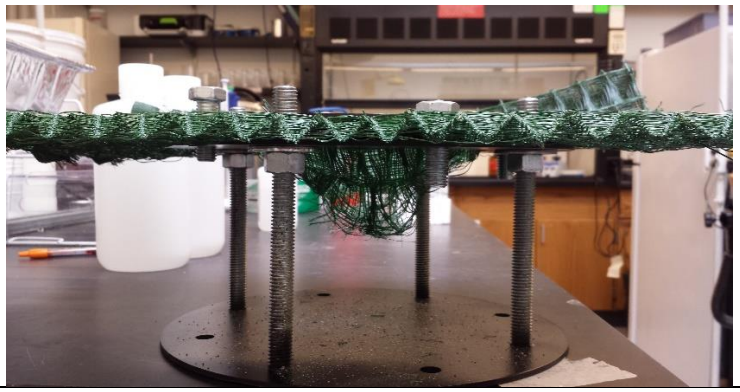
Pyramat(Tan)	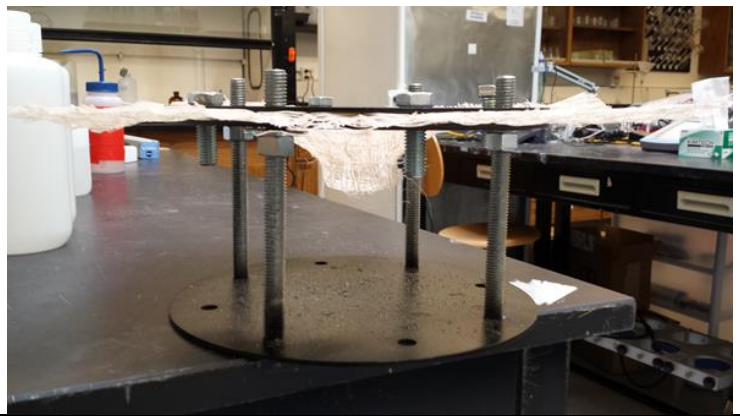
Landlok 300	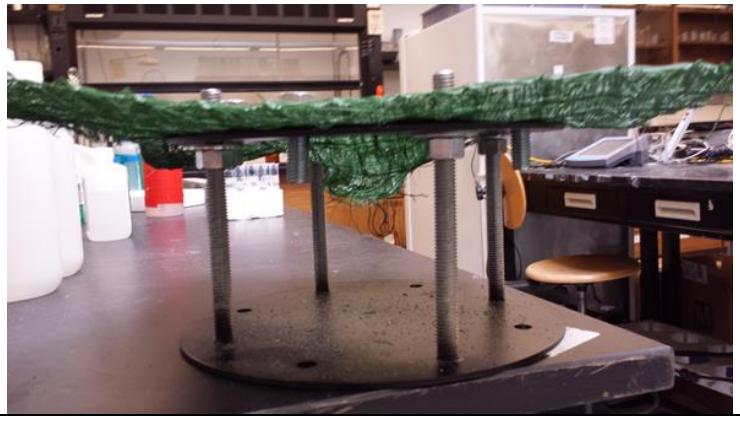

Landlok 3000G	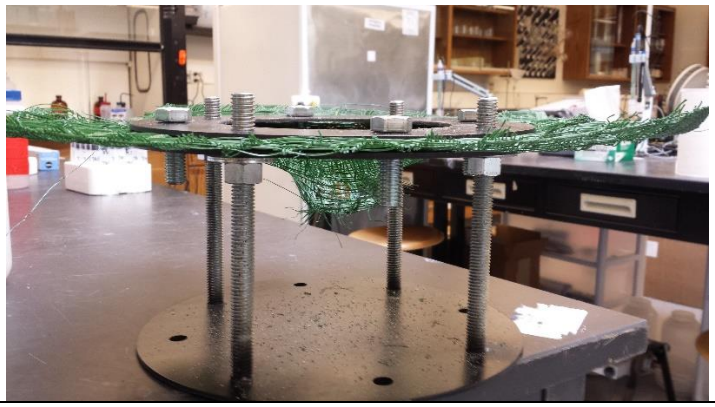
T-RECS	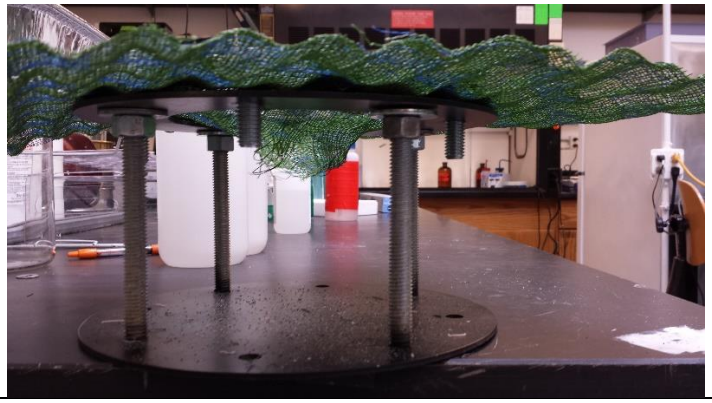
Excel PP5-Xtreme	
VMax W3000	

APPENDIX C. DYNAMIC PERFORATION TEST RESULTS

Table C.1. Test results for Pyramat Green

Sample Number	Hole Diameter (mm)	Remarks
1	10.5	Center
2	7.0	Center
3	12.0	Center
4	9.8	Center
5	8.0	Center
6	11.4	bottom
7	8	Bottom
8	10	Bottom
9	12	Bottom
10	11	Bottom
11	12.0	Border
12	10.0	Border
13	8.0	Border
14	9.0	Border
15	10.0	Border
16	12.0	Middle
17	13.0	Middle
18	12.0	Middle
19	12.0	Middle
20	11.5	Middle
21	5.5	Top
22	6.0	Top
23	6.0	Top
24	5.8	Top
25	6.0	Top
Total	Average (mm)	9.5
	Standard deviation	2.38
	COV(%)	24.90
Border	Average	9.8
	Standard deviation	1.33
	COV(%)	13.54
Top	Average	5.9
	Standard deviation	0.20
	COV(%)	3.34
Middle	Average	12.1
	Standard deviation	0.49

	COV(%)	4.05
Bottom	Average	10.5
	Standard deviation	1.40
	COV(%)	13.36
Center	Average	9.5
	Standard deviation	1.78
	COV(%)	18.81

Table C.2. Test results for Pyramat Tan

Sample Number	Hole Diameter (mm)	Remarks
1	18.0	center
2	18.2	center
3	18.5	center
4	18.4	center
5	18.2	center
6	13.0	bottom, loose side
7	13.8	bottom, loose side
8	13.0	bottom, loose side
9	14.0	bottom, loose side
10	14.0	bottom, loose side
11	11.8	bottom, dense side
12	12.0	bottom, dense side
13	12.0	bottom, dense side
14	12.0	bottom, dense side
15	12.0	bottom, dense side
16	15	middle, loose side
17	15.2	middle, loose side
18	16	middle, loose side
19	16	middle, loose side
20	14.5	middle, loose side
21	8.0	middle, dense side
22	8.0	middle, dense side
23	8.0	middle, dense side
24	8.5	middle, dense side
25	8.2	middle, dense side
26	14.0	border
27	13.0	border
28	14.0	border
29	14.2	border
30	11.5	Top
31	10.8	Top
32	12.0	Top
33	11.0	Top
34	11.3	Top
Total	Average	13.26
	Standard deviation	2.9871
	COV(%)	22.5221
Center	Average	18.26
	Standard deviation	0.1744
	COV(%)	0.9549

Bottom, loose side	Average	13.56
	Standard deviation	0.4630
	COV(%)	3.4147
Bottom, dense side	Average	11.96
	Standard deviation	0.0800
	COV(%)	0.6689
Middle, loose side	Average	15.34
	Standard deviation	0.5851
	COV(%)	3.8145
Middle, dense side	Average	8.14
	Standard deviation	0.1960
	COV(%)	2.4074
Top	Average	11.32
	Standard deviation	0.4167
	COV(%)	3.6807
Border	Average	13.8
	Standard deviation	0.46904158
	COV(%)	3.398852

Table C.3. Test results for Landlok 300

Sample Number	Hole Diameter (mm)	Remarks
1	20.0	center
2	20.0	center
3	22.0	center
4	20.2	center
5	20.4	center
6	19.4	bottom of slope
7	20.3	bottom of slope
8	19.0	bottom of slope
9	18.0	bottom of slope
10	20.0	bottom of slope
11	17.8	bottom of slope
12	16.4	border
13	14.2	border
14	15.2	border
15	15.5	border
16	15.0	border
17	16.2	middle of slope
18	14.0	middle of slope
19	15.0	middle of slope
20	15.6	middle of slope
21	14.0	middle of slope
22	14.0	middle of slope
23	10.3	top
24	10.8	top
25	9.8	top
26	10.0	top
27	10.2	top
Total	Average	16.05
	Standard deviation	3.6175
	COV(%)	22.5415
Border	Average	15.26
	Standard deviation	0.7144
	COV(%)	4.6817
Top	Average	10.22
	Standard deviation	0.3370
	COV(%)	3.2979
Middle	Average	14.80
	Standard deviation	0.8718

	COV(%)	5.8904
Bottom	Average	19.08
	Standard deviation	0.9353
	COV(%)	4.9010
Center	Average	20.52
	Standard deviation	0.7547
	COV(%)	3.6780

Table C.4. Test results for Landlok 3000G

Sample Number	Hole Diameter (mm)	Remarks
1	10	Center
2	10	Center
3	9.5	Center
4	10.2	Center
5	10	Center
6	13	Bottom
7	14	Bottom
8	12	Bottom
9	15.2	Bottom
10	14	Bottom
11	12	Border
12	14	Border
13	14.5	Border
14	12.2	Border
15	14	Border
16	10.5	Middle
17	11	Middle
18	10.5	Middle
19	10.3	Middle
20	11.5	Middle
21	6	Top
22	8	Top
23	6	Top
24	6.5	Top
25	6	Top
Total	Average	11.03
	Standard deviation	2.5709
	COV(%)	23.3064
Border	Average	13.34
	Standard deviation	1.0307
	COV(%)	7.7266
Top	Average	6.5
	Standard deviation	0.7746
	COV(%)	11.9169
Middle	Average	10.76
	Standard deviation	0.4363
	COV(%)	4.0553
Bottom	Average	13.64

	Standard deviation	1.0763
	COV(%)	7.8907
Center	Average	9.94
	Standard deviation	0.2332
	COV(%)	2.3465

Table C.5. Test results for T-RECS

Sample Number	Hole Diameter (mm)	Remarks
1	7	top
2	6.5	top
3	7	top
4	7	top
5	7	top
6	7	Bottom, blue&green mix
7	7	Bottom, blue&green mix
8	7	Bottom, blue&green mix
9	6.8	Bottom, blue&green mix
10	7	Bottom,blue&green mix
11	4	Bottom,green
12	4	Bottom, green
13	4	Bottom, green
14	4	Bottom, green
15	4.2	Bottom, green
Total	Average	5.97
	Standard deviation	1.3690
	COV(%)	22.9445
Bottom, green	Average	4.04
	Standard deviation	1.9802
	COV(%)	0.0800
Bottom, blue&green	Average	6.96
	Standard deviation	0.0800
	COV(%)	1.1494
Top	Average	6.90
	Standard deviation	0.2000
	COV(%)	2.8986

Table C.6. Test results for Excel PP5-Xtreme

Sample Number	Hole Diameter (mm)	Remarks
1	14	Center
2	13.5	Center
3	13.8	Center
4	14.2	Center
5	14	Center
6	13	Bottom
7	14	Bottom
8	12	Bottom
9	15.2	Bottom
10	14	Bottom
11	10	Border
12	9.8	Border
13	10	Border
14	10	Border
15	9.8	Border
16	12	Middle
17	13	Middle
18	12.8	Middle
19	12.5	Middle
20	13	Middle
21	11	Top
22	10	Top
23	9.5	Top
24	10.2	Top
25	10	Top
Total	Average	11.03
	Standard deviation	2.57
	COV(%)	23.31
Border	Average	9.92
	Standard deviation	0.10
	COV(%)	0.99
Top	Average	10.14
	Standard deviation	0.4883
	COV(%)	4.8152
Middle	Average	12.66
	Standard deviation	0.3774
	COV(%)	2.9807
Bottom	Average	13.64

	Standard deviation	1.0763
	COV(%)	7.8907
Center	Average	13.90
	Standard deviation	0.2366
	COV(%)	1.7025

Table C.7. Test results for VMax W3000

Sample Number	Hole Diameter (mm)	Remarks
1	6.0	top side, black line
2	5.8	top side, black line
3	6.0	top side, black line
4	6.0	top side, black line
5	5.9	top side, black line
6	4.0	top side, middle
7	4.0	top side, middle
8	4.0	top side, middle
9	4.2	top side, middle
10	4.1	top side, middle
11	9.0	bottom side, black line
12	9.0	bottom side, black line
13	9.0	bottom side, black line
14	8.8	bottom side, black line
15	9.0	bottom side, black line
16	8.0	bottom side, middle
17	7.8	bottom side, middle
18	8.0	bottom side, middle
19	8.2	bottom side, middle
20	8.0	bottom side, middle
total	average	6.74
	Standard deviation	1.8956
	COV(%)	28.1250
top side black line	average	5.94
	Standard deviation	0.0829
	COV(%)	1.3959
top side middle	average	4.06
	Standard deviation	0.0800
	COV(%)	1.9704
bottom side black line	average of total	8.96
	Standard deviation	0.0800
	COV(%)	0.8929
bottom side middle	average of total	7.98
	Standard deviation	0.0980
	COV(%)	1.2278

APPENDIX D. GRAIN SIZE DISTRIBUTIONS OF SOIL USED IN HYDRAULIC CONDUCTIVITY RATIO TEST

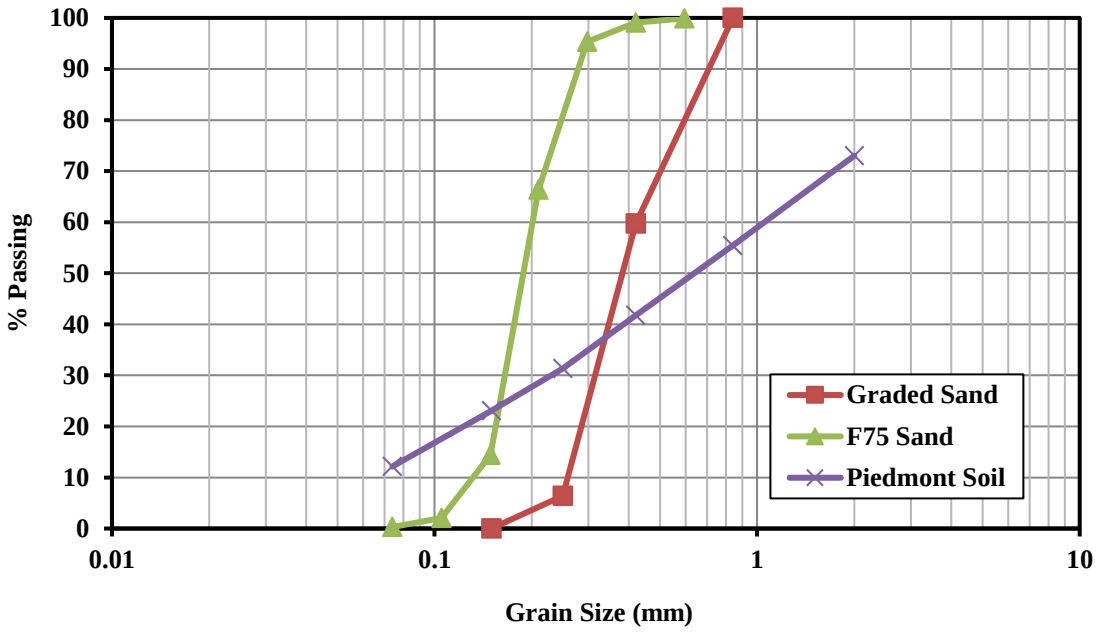

Figure D-1. Grain size distributions of soil samples.

REFERENCES

Abbaspour, A., Tanyu, B. F., Aydilek, A. H., & Dayioglu, A. Y. (2018). Methodology to evaluate hydraulic compatibility of geotextile and RCA in underdrain systems. Geosynthetics International, 25(1), 67-84.

Adams, C. A., Apraku, E., & Opoku-Boahen, R. (2015). Effect of triaxial geogrid reinforcement on CBR strength of natural gravel soil for road pavements. J. Civ. Eng. Res, 5(2), 45-51.

Allen, S. R. "Evaluation and standardization of rolled erosion control products." Geotextiles and Geomembranes 14, no. 3-4 (1996): 207-221.

Allen, T. M., and R. J. Bathurst. "Characterization of geosynthetic load-strain behavior after installation damage." Geosynthetics International 1.2 (1994): 181-199.

Ammann, Martin, et al. "Significance of tree root decomposition for shallow landslides." For Snow Landsc Res 82.79-94 (2009): 79.

Amezketa, E. (1999). Soil aggregate stability: a review. Journal of sustainable agriculture, 14(2-3), 83-151.

Askari, Azadeh Seif, Saeed Shaikhzadeh Najar, and Yoness Alizadeh Vaghasloo. "Study the Effect of Test Speed and Fabric Weight on Puncture Behavior of Polyester Needlepunched Nonwoven Geotextiles." Journal of Engineered Fibers and Fabrics 7, no. 3 (2012): 155892501200700301.

ASTM International. D6241-14 Standard Test Method for Static Puncture Strength of Geotextiles and Geotextile-Related Products Using a 50-mm Probe. West Conshohocken, PA; ASTM International, 2014. doi: https://doi.org/10.1520/D6241-14

ASTM International. D6460-19 Standard Test Method for Determination of Rolled Erosion Control Product (RECP) Performance in Protecting Earthen Channels from Stormwater-Induced Erosion. West Conshohocken, PA; ASTM International, 2019. doi: https://doi.org/10.1520/D6460-19

ASTM International. D6475-17 Standard Test Method for Measuring Mass per Unit Area of Erosion Control Blankets. West Conshohocken, PA; ASTM International, 2017. doi: https://doi.org/10.1520/D6475-17

ASTM International. D6525/D6525M-18 Standard Test Method for Measuring Nominal Thickness of Rolled Erosion Control Products. West Conshohocken, PA; ASTM International, 2018. doi: https://doi.org/10.1520/D6525_D6525M-18

ASTM International. D6566-18 Standard Test Method for Measuring Mass Per Unit Area of Turf Reinforcement Mats. West Conshohocken, PA; ASTM International, 2018. doi: https://doi.org/10.1520/D6566-18

ASTM International. D6567-18 Standard Test Method for Measuring the Light Penetration of a Rolled Erosion Control Product (RECP). West Conshohocken, PA; ASTM International, 2018. doi: https://doi.org/10.1520/D6567-18

ASTM International. D6575/D6575M-16 Standard Test Method for Determining Stiffness of Geosynthetics Used as Turf Reinforcement Mats (TRMs). West Conshohocken, PA; ASTM International, 2016. doi: https://doi.org/10.1520/D6575_D6575M-16

ASTM International. D6818-18a Standard Test Method for Ultimate Tensile Properties of Rolled Erosion Control Products. West Conshohocken, PA; ASTM International, 2018. doi: https://doi.org/10.1520/D6818-18A

ASTM International. D7101-13e1 Standard Index Test Method for Determination of Unvegetated Rolled Erosion Control Product (RECP) Ability to Protect Soil from Rain Splash and Associated Runoff Under Bench-Scale Conditions. West Conshohocken, PA; ASTM International, 2013. doi: https://doi.org/10.1520/D7101-13E01

Atmatzidis, D. K., and D. A. Chrysikos. "On the Static Puncture Strength of Non-woven Geotextiles." 7th International Conference on Geosynthetics. Nice. 2002.

Austin, Deron N., and Lynn E. Ward. "ECTC provides guidelines for rolled erosion-control products." Geotechnical Fabrics Report 14, no. 3 (1996): 18-21.

Barton, Christopher, and Karen Kinkead. "Do erosion control and snakes mesh?." Journal of Soil and Water Conservation 60, no. 2 (2005): 33A-35A.

Basu, G., Roy, A. N., Bhattacharyya, S. K., & Ghosh, S. K. (2009). Construction of unpaved rural road using jute–synthetic blended woven geotextile–A case study. Geotextiles and Geomembranes, 27(6), 506-512.

Baucom, J. N., & Zikry, M. A. (2003). Evolution of failure mechanisms in 2D and 3D woven composite systems under quasi-static perforation. Journal of composite materials, 37(18), 1651-1674.

Belytschko, T., & Tabbara, M. (1996). Dynamic fracture using element-free Galerkin methods. International Journal for Numerical Methods in Engineering, 39(6), 923-938.

Bergado, DT, S Youwai, CN Hai, and P Voottipruex. "Interaction of Nonwoven Needle-Punched Geotextiles under Axisymmetric Loading Conditions." Geotextiles and Geomembranes 19, no. 5 (2001): 299-328.

Bolt, Adam, and Angelika Duszynska. "Static puncture resistance of non-woven geotextiles." In Modern Building Materials, Structures and Techniques. Proceedings of the International Conference, vol. 10, p. 1083. Vilnius Gediminas Technical University, Department of Construction Economics & Property, 2010.

Brahmachary, T. K., & Rokonuzzaman, M. (2018). Investigation of random inclusion of bamboo fiber on ordinary soil and its effect CBR value. International Journal of Geo-Engineering, 9(1), 10.

Burns, Susan E., Hyunwook Choo, and Jong Muk Won. Categorization of erosion control matting for slope applications. No. FHWA-GA-16-11-22. Georgia. Department of Transportation. Office of Research, 2013.

Burns, Susan E. Categorization of erosion control matting. No. GDOT PROJ NO. 07-25. Georgia. Dept. of Transportation, 2012.

Butt, W. A., Mir, B. A., & Jha, J. N. (2016). Strength behavior of clayey soil reinforced with human hair as a natural fibre. Geotechnical and Geological Engineering, 34(1), 411-417.

Callus, P. J., Mouritz, A. P., Bannister, M. K., & Leong, K. H. (1999). Tensile properties and failure mechanisms of 3D woven GRP composites. Composites Part A: Applied Science and Manufacturing, 30(11), 1277-1287.

Capilleri, P. P., Motta, E., & Raciti, E. (2016). Experimental study on native plant root tensile strength for slope stabilization. Procedia Engineering, 158, 116-121.

Cappello, Leonardo, et al. "Exploiting textile mechanical anisotropy for fabric-based pneumatic actuators." Soft robotics 5.5 (2018): 662-674.

Chapman, B. M. "The bending and creasing of multicomponent viscoelastic fiber assemblies: Part III: the mechanics of a two-dimensional assembly of generalized linear viscoelastic fibers of different types." Textile Research Journal 44.4 (1974): 306-309.

Cheah, Charmaine, et al. "Effect of simulated rock dumping on geotextile." 12th Australian New Zealand Conference on Geomechanics (2015).

Cheeseman, B. A., & Bogetti, T. A. (2003). Ballistic impact into fabric and compliant composite laminates. Composite structures, 61(1-2), 161-173.

Cheng, H., Yang, X., Liu, A., Fu, H., & Wan, M. (2003, October). A study on the performance and mechanism of soil-reinforcement by herb root system. In Proceedings of third international vetiver conference, Guangzhou, China (Vol. 384, p. 390).

Choudhary, A. K., Jha, J. N., Gill, K. S., & Shukla, S. K. (2014). Utilization of fly ash and waste recycled product reinforced with plastic wastes as construction materials in flexible pavement. In Geo-Congress 2014: Geo-characterization and Modeling for Sustainability (pp. 3890-3902).

Chowdhury, S., Chatterjee, S., KushagraSen, A.P., Vashi, J. and Daftardar, A., (2016) IMPROVEMENT OF CBR FOR CLAYEY SAND SUBGRADE USING WOVEN GEOTEXTILE., Indian Geotechnical Conference IGC 2016

Clark, L. A., & Wynn, T. M. (2007). Methods for determining streambank critical shear stress and soil erodibility: Implications for erosion rate predictions. Transactions of the ASABE, 50(1), 95-106.

Cooper, D. N. E. "The stiffness of woven textiles." Journal of the Textile Institute Transactions 51.8 (1960): T317-T335.

Coppin, Nick J, and Ivor G Richards. Use of Vegetation in Civil Engineering. Construction Industry Research and Information Association London, 1990.

De Baets, S., Poesen, J., Reubens, B., Wemans, K., De Baerdemaeker, J., & Muys, B. (2008). Root tensile strength and root distribution of typical Mediterranean plant species and their contribution to soil shear strength. Plant and soil, 305(1-2), 207-226.

De Baets, S., Poesen, J., Knapen, A., Barberá, G. G., & Navarro, J. A. (2007). Root characteristics of representative Mediterranean plant species and their erosion-reducing potential during concentrated runoff. Plant and Soil, 294(1-2), 169-183.

Dhatrak, A. I., & Konmare, S. D. (2015). Performance of randomly oriented plastic waste in flexible pavement. Int J Pure Appl Res Eng Technol (IJPRET), 3(9), 193-202.

Dixit, A., Misra, R. K., & Mali, H. S. (2015). Finite element analysis of quasi-static indentation of woven fabric textile composites using different nose shape indenters: Finite-Elemente-Analyse von quasi statischen Eindrücken mit verschiedenen Indentergeometrien bei textilen Kompositen. Materialwissenschaft und Werkstofftechnik, 46(10), 1014-1028.

Dong, Y. L., Han, J., & Bai, X. H. (2010). Bearing capacities of geogrid-reinforced sand bases under static loading. In Ground Improvement and Geosynthetics (pp. 275-281).

Dudeck, A. E., N. P. Swanson, L. N. Mielke, and A. R. Dedrick. "Mulches for Grass Establishment on Fill Slopes 1." Agronomy Journal 62, no. 6 (1970): 810-812.

Duncan-Williams, E., & Attoh-Okine, N. O. (2008). Effect of geogrid in granular base strength–An experimental investigation. Construction and building materials, 22(11), 2180-2184.

EN ISO 13433. (2006). Geosynthetics—Dynamic perforation test (cone drop test).

Ennos, A. R. (1990). The anchorage of leek seedlings: the effect of root length and soil strength. Annals of Botany, 65(4), 409-416.

Evette, A., Labonne, S., Rey, F., Liebault, F., Jancke, O., & Girel, J. (2009). History of bioengineering techniques for erosion control in rivers in Western Europe. Environmental Management, 43(6), 972.

Genet, M., et al. (2005). "The influence of cellulose content on tensile strength in tree roots." Plant and Soil 278(1-2): 1-9.

Ghosh, Tushar K. "Puncture Resistance of Pre-Strained Geotextiles and Its Relation to Uniaxial Tensile Strain at Failure." Geotextiles and Geomembranes 16, no. 5 (1998): 293-302.

Glinski, J. (2018). Soil physical conditions and plant roots. CRC press.

Golzarian, Mahmood R., and Ross A. Frick. "Classification of images of wheat, ryegrass and brome grass species at early growth stages using principal component analysis." Plant Methods 7.1 (2011): 28.

Gowda, T. M., Naidu, A. C. B., & Chhaya, R. (1999). Some mechanical properties of untreated jute fabric-reinforced polyester composites. Composites Part A: applied science and manufacturing, 30(3), 277-284.

Gray, D. H., & Sotir, R. B. (1996). Biotechnical and soil bioengineering slope stabilization: a practical guide for erosion control. John Wiley & Sons.

Gyssels, G., Poesen, J., Bochet, E., & Li, Y. (2005). Impact of plant roots on the resistance of soils to erosion by water: a review. Progress in physical geography, 29(2), 189-217.

Gyssels, Gwendolyn, and Jean Poesen. "The importance of plant root characteristics in controlling concentrated flow erosion rates." Earth Surface Processes and Landforms: The Journal of the British Geomorphological Research Group 28, no. 4 (2003): 371-384.

Han, Jie, and Jun Guo. "Geosynthetic-stabilized vegetated earth surfaces for environmental sustainability in civil engineering." Innovative Materials and Design for Sustainable Transportation Infrastructure. 2015.

Helwany, S. (2007). Applied soil mechanics with ABAQUS applications. John Wiley & Sons.

Hisatake, Kazuo, Satoko Tanaka, and Youko Aizawa. "Evaporation rate of water in a vessel." Journal of applied physics 73.11 (1993): 7395-7401.

Hochard, C., Aubourg, P. A., & Charles, J. P. (2001). Modelling of the mechanical behaviour of woven-fabric CFRP laminates up to failure. Composites Science and Technology, 61(2), 221-230.

Hoya, Akihiko, et al. "Germination and seedling survivorship characteristics of hybrids between native and alien species of dandelion (Taraxacum)." Plant species biology 19.2 (2004): 81- Hochard, C., Aubourg, P. A., & Charles, J. P. (2001). Modelling of the mechanical behaviour of woven-fabric CFRP laminates up to failure. Composites Science and Technology, 61(2), 221-230.

Hsieh, Chiwan, and Jau-Bih Wang. "Clamping mechanism effects on the puncture resistance tests of high strength geotextiles." Journal of GeoEngineering 3.2 (2008): 47-53.

Krolak (2016). Highways in the River Environment- Floodplains, Extreme Events, Risk, and Resilience. Hydraulic Engineering Circular No. 17, 2nd Edition, U.S. Department of Transportation Federal Highway Administration, https://www.fhwa.dot.gov/engineering/ hydraulics/ pubs/hif16018.pdf

Hussein, M. G., & Meguid, M. A. (2016). A three-dimensional finite element approach for modeling biaxial geogrid with application to geogrid-reinforced soils. Geotextiles and Geomembranes, 44(3), 295-307.90.

Hu, J., Gao, C., He, S., Chen, W., Li, Y., Zhao, B., ... & Yang, D. (2017). Effects of on-axis and off-axis tension on uniaxial mechanical properties of plain woven fabrics for inflated structures. Composite Structures, 171, 92-99.

Jastrow, J. D., Miller, R. M., & Lussenhop, J. (1998). Contributions of interacting biological mechanisms to soil aggregate stabilization in restored prairie. Soil Biology and Biochemistry, 30(7), 905-916.

Ji, J., et al. (2020). "Energy-based fibre bundle model algorithms to predict soil reinforcement by roots." Plant and Soil 446(1): 307-329.

Jia, X., Sun, B., & Gu, B. (2012). A numerical simulation on ballistic penetration damage of 3D orthogonal woven fabric at microstructure level. International Journal of Damage Mechanics, 21(2), 237-266.

Jones, D. R. V., D. A. Shercliff, and N. Dixon. "Difficulties associated with the specification of protection geotextiles using only unit weight." Proceedings of the Second European Geosynthetics Conference, Bologna, Italy. 2000.

Jovicic, J. M. (2003). Numerical modeling and analysis of static and ballistic behavior of multi-layered/multiphase composite materials using detailed microstructural discretization. PhD Dissertation, Drexel University.

Kamali Dolatabadi, Mehdi. "Anisotropy in geometrical and tensile properties of plain weave fabric: verifying a semi-empirical model." The Journal of The Textile Institute 108.9 (2017): 1537-1544.

Kader, M. A., Senge, M., Mojid, M. A., & Ito, K. (2017). Recent advances in mulching materials and methods for modifying soil environment. Soil and Tillage Research, 168, 155-166.

Kapfer, Joshua M., and Rori A. Paloski. "On the threat to snakes of mesh deployed for erosion control and wildlife exclusion." Herpetological Conservation and Biology 6, no. 1 (2011): 1-9.

Karademir, T., & Frost, J. D. (2014). Micro-scale tensile properties of single geotextile polypropylene filaments at elevated temperatures. Geotextiles and Geomembranes, 42(3), 201-213..

Khanna, Sumee. "Aging effects of environmental factors on rolled erosion control products." PhD diss., Texas A&M University, 2005.

Khouly, M. A. (1995). Analysis of soil-reinforcement interaction, Doctoral dissertation, The Ohio State University.

Kilby, W. F. (1963). 2—Planar stress–strain relationships in woven fabrics. Journal of the Textile Institute Transactions, 54(1), T9-T27.

Koerner, George R., and Robert M. Koerner. "Puncture resistance of polyester (PET) and polypropylene (PP) needle-punched nonwoven geotextiles." Geotextiles and Geomembranes 29.3 (2011): 360-362.

Lammens, Nicolas, et al. "Improved accuracy in the determination of flexural rigidity of textile fabrics by the Peirce cantilever test (ASTM D1388)." Textile Research Journal 84.12 (2014): 1307-1314.

Lan, Jian, Zhang, L., Shao S., Yao A., “Study on characteristics of growth and development of turf-type perennial ryegrass.” Pratacultural Science 20 no.5 (2003): 43-45

Lee, B. L., et al. "Penetration failure mechanisms of armor-grade fiber composites under impact." Journal of composite materials 35.18 (2001): 1605-1633.

Li, T. T., Fang, J., Huang, C. H., Lou, C. W., Lin, J. Y., Lin, M. C., ... & Lin, J. H. (2017). Numerical simulation of dynamic puncture behaviors of woven fabrics based on the Finite Element Method. Textile Research Journal, 87(11), 1308-1317.

Loades, K. W., Bengough, A. G., Bransby, M. F., & Hallett, P. D. (2015). Effect of root age on the biomechanics of seminal and nodal roots of barley (Hordeum vulgare L.) in contrasting soil environments. Plant and Soil, 395(1-2), 253-261.

Lomov, S. V., Ivanov, D. S., Truong, T. C., Verpoest, I., Baudry, F., Bosche, K. V., & Xie, H. (2008). Experimental methodology of study of damage initiation and development in textile composites in uniaxial tensile test. Composites Science and Technology, 68(12), 2340-2349.

López-Gálvez, H., & Soldani, X. (2019). Suitability of numerical model from low to high velocity impacts against KM2 fabrics with isotropic hypothesis. Composite Structures, 214, 390-396.

Lo, W. M. W. (2002). A study of fabric anisotropy. Hong Kong Polytechnic University -- Dissertations

Mahadevan, L., and Keller, J. B. (1999). Periodic folding of thin sheets. Siam Review, 41(1), 115-131

McCool, D. K. (2017). The revised universal soil loss equation. In Soil erosion research methods (pp. 105-126). Routledge.

Mendoza, C., & Caicedo, B. (2018). Elastoplastic framework of relationships between CBR and Young’s modulus for granular material. Road Materials and Pavement Design, 19(8), 1796-1815.

Minh, D. N., Thanh, T. N., & Le Huu, T. (2020). The Effects of Soaking Process on the Bearing Capacity of Soft Clay Reinforced by Nonwoven Geotextile. In Geotechnics for Sustainable Infrastructure Development (pp. 669-676). Springer, Singapore.

Morgan, Roy PC, and R. Jane Rickson. Slope stabilization and erosion control: a bioengineering approach. Taylor & Francis, 2003.

Murphy, VP, and RM Koerner. "CBR Strength (Puncture) of Geosynthetics." Geotechnical Testing Journal 11, no. 3 (1988): 167-72.

Ning, Wei et al., “Germination Characteristics of Taraxacum variegatum Kitag (Asteraceae).” Journal of Shenyang Agriculture University 44 no.2 (2013): 219-222

Niziolomski, J. (2014). Optimising soil disturbance and mulch attenuation for erosion and runoff control in asparagus crops.

Norris, Joanne E. "Root reinforcement by hawthorn and oak roots on a highway cut-slope in Southern England." Plant and Soil 278.1-2 (2005): 43-53.

Olschewski, Jan, Stefan Cantré, and Fokke Saathoff. "Proposals for Future Index Parameters for Erosion Control Products." (2012).

Özdemir, H., & Mert, E. (2013). The effects of fabric structural parameters on the tensile, bursting, and impact strengths of cellular woven fabrics. Journal of the Textile Institute, 104(3), 330-338.

Pan, N., Kovar, R., Dolatabadi, M. K., Wang, P., Zhang, D., Sun, Y., & Chen, L. (2015). Origin of tensile strength of a woven sample cut in bias directions. Royal Society Open Science, 2(5), 140499.

Patel, S. K., & Singh, B. (2017). Experimental Investigation on the Behaviour of Glass Fibre-Reinforced Cohesive Soil for Application as Pavement Subgrade Material. International Journal of Geosynthetics and Ground Engineering, 3(2), 13.

Peirce, F. T. (1930). "The “handle” of cloth as a measurable quantity." Journal of the Textile Institute Transactions 21(9): T377-T416.

Penava, Ž., Šimić-Penava, D., & Knezic, Ž. (2014). Determination of the elastic constants of plain woven fabrics by a tensile test in various directions. Fibres & Textiles in Eastern Europe.

Perkins, S. W. (2000). Constitutive modeling of geosynthetics. Geotextiles and Geomembranes, 18(5), 273-292.

Plaut, Raymond H. "Formulas to determine fabric bending rigidity from simple tests." Textile Research Journal 85.8 (2015): 884-894.

Plaut, R. H., & Virgin, L. N. (2014). Deformation and vibration of upright loops on a foundation and of hanging loops. International Journal of Solids and Structures, 51(18), 3067-3075.

Pollen, Natasha, and Andrew Simon. "Estimating the mechanical effects of riparian vegetation on stream bank stability using a fiber bundle model." Water Resources Research 41.7 (2005).

Prosser, R. A., Cohen, S. H., & Segars, R. A. (2000). Heat as a factor in the penetration of cloth ballistic panels by 0.22 caliber projectiles. Textile Research Journal, 70(8), 709-722.

Rahman, M. M., Saha, S., Hamdi, A. S. A., & Alam, M. J. B. (2019). Development of 3-D Finite Element Models for Geo-Jute Reinforced Flexible Pavement. Civ. Eng. J, 5, 437-446.

Rauchecker, M., et al. (2019). Measuring the Tensile Strength of Phleum pratense L. Roots. Recent Advances in Geotechnical Research, Springer: 163-173.

Reubens, Bert, Jean Poesen, Frédéric Danjon, Guy Geudens, and Bart Muys. "The role of fine and coarse roots in shallow slope stability and soil erosion control with a focus on root system architecture: a review." Trees 21, no. 4 (2007): 385-402.

Rickson, R. Jane. "The role of simulated vegetation in soil erosion control." Vegetation and erosion. Processes and environments. (1990): 99-111.

Rix, G. J. (1995). Installation Damage to Woven Polyproplene Geotextiles. School of Civil and Environmental Engineering, Georgia Institute of Technology.

Saberi, E., Najar, S. S., Abdellahi, S. B., & Soltanzadeh, Z. (2017). A hyperelastic approach for finite element modelling puncture resistance of needle punched nonwoven geotextiles. Fibers and Polymers, 18(8), 1623-1628.

Santillan, S. T., Virgin, L. N., & Plaut, R. H. (2006). Post-bauckling and Vibration of Heavy Beam on Horizontal or Inclined Rigid Foundation.

Santillan, S., Virgin, L. N., & Plaut, R. H. (2005). Equilibria and vibration of a heavy pinched loop. Journal of sound and vibration, 288(1-2), 81-90.

Semeraro, Federico, et al. "Anisotropic analysis of fibrous and woven materials part 1: Estimation of local orientation." Computational Materials Science 178 (2020): 109631.

Schmidt, K. M., et al. "The variability of root cohesion as an influence on shallow landslide susceptibility in the Oregon Coast Range." Canadian Geotechnical Journal 38.5 (2001): 995-1024.

Shams, B., Ardakani, A., & Roustaei, M. (2019). Laboratory investigation of geotextile position on CBR of clayey sand soil under freeze-thaw cycle. Scientia Iranica.

Smith, J. L., Davieau, M. R., & Bhatia, S. K. (2007). Evaluation of soil erosion using the rainsplash technique. In Geotechnics of Soil Erosion (pp. 1-10).

Sockalingam, S., Chowdhury, S. C., Gillespie Jr, J. W., & Keefe, M. (2017). Recent advances in modeling and experiments of Kevlar ballistic fibrils, fibers, yarns and flexible woven textile fabrics–a review. Textile Research Journal, 87(8), 984-1010.

Stokes, A., Atger, C., Bengough, A. G., Fourcaud, T., & Sidle, R. C. (2009). Desirable plant root traits for protecting natural and engineered slopes against landslides. Plant and soil, 324(1-2), 1-30.

Subaida, E. A., Chandrakaran, S., & Sankar, N. (2008). Experimental investigations on tensile and pullout behaviour of woven coir geotextiles. Geotextiles and Geomembranes, 26(5), 384-392.

Takatera, M., & Shinohara, A. (1996). An analysis to compare conventional methods for estimating bending rigidity of fabrics. Journal of the Textile Machinery Society of Japan, 42(3-4), 86-92.

Tan, V. B. C., Shim, V. P. W., & Zeng, X. (2005). Modelling crimp in woven fabrics subjected to ballistic impact. International journal of impact engineering, 32(1-4), 561-574.

"Taraxacum officinale". Natural Resources Conservation Service PLANTS Database. USDA. Retrieved 8 December 2015.

Termonia, Yves. "Puncture resistance of fibrous structures." International Journal of Impact Engineering 32.9 (2006): 1512-1520.

Theisen, Marc S., and R. G. Carroll Jr. "Turf reinforcement-the" soft armor" alternative." In Erosion Control: Technology in Transition. Proceedings of Conference-International Erosion Control Association, XXI, held at Washington DC, USA, 14-17 Feb. 1990., pp. 255-270. International Erosion Control Association, 1990.

Tran, T. K., Kim, D. J., & Choi, E. (2014). Behavior of double-edge-notched specimens made of high performance fiber reinforced cementitious composites subject to direct tensile loading with high strain rates. Cement and concrete research, 63, 54-66.

Tosi, M. (2007). "Root tensile strength relationships and their slope stability implications of three shrub species in the Northern Apennines (Italy)." Geomorphology 87(4): 268-283.

Valizadeh, M., Lomov, S., Ravandi, S. A. H., Salimi, M., & Rad, S. Z. (2010). Finite element simulation of a yarn pullout test for plain woven fabrics. Textile research journal, 80(10), 892-903.

Vannoppen, Wouter, Matthias Vanmaercke, Sarah De Baets, and Jean Poesen. "A review of the mechanical effects of plant roots on concentrated flow erosion rates." Earth-Science Reviews 150 (2015): 666-678.

Van Dyke, Titi, and EI-Hajjar . "Comparison of CBR and Pin Puncture Strength Testing Used in the Evaluation of Geotextiles." , 3rd Pan-American conference on Geosynthetics (2016).

Van Dyke, Stacy. "Comparison of CBR and Pin Puncture Strength Testing Used in the Evaluation of Geotextiles." (2014).

Vergani, C., E. A. Chiaradia, and G. B. Bischetti. "Variability in the tensile resistance of roots in Alpine forest tree species." Ecological Engineering 46 (2012): 43-56.

Waldron, L. J., and Suren Dakessian. "Soil reinforcement by roots: calculation of increased soil shear resistance from root properties." Soil science 132.6 (1981): 427-435.

Waldron, L. J. "The shear resistance of root-permeated homogeneous and stratified soil." Soil Science Society of America Journal 41.5 (1977): 843-849.

Wang, D., Naouar, N., Vidal-Salle, E., & Boisse, P. (2018). Longitudinal compression and Poisson ratio of fiber yarns in meso-scale finite element modeling of composite reinforcements. Composites Part B: Engineering, 141, 9-19.

Wang, X. Q., Cui, Y. L., Zhang, S. M., Ge, J. G., & Wu, X. F. (2015). Research on Construction Technology of Three-Dimensional Reinforced Rigid-Flexible Composite Ecological Retaining Wall. In Applied Mechanics and Materials (Vol. 744, pp. 560-564). Trans Tech Publications Ltd.

Wang, H. "Research on mechanism of root reinforcing soil and slope erosion in slope protection by vegetation." PhD Dissertation, Southwest Jiaotong University, People's Republic of China (2010).

Wang, J. Y., Hughes, P. N., & Augrade, C. E. (2019). CBR strength of London Clay reinforced with polypropylene fibre. Proceedings of the XVII ECSMGE-2019, Geotechnical Engineering foundation of the future ISBN, 978-9935.

Wang, P., Y. Zhang, and B. Sun. "Tear And Puncture Behaviors Of Flexible Composites." 18th International Conference on Composite Materials, August, Korea. 2011.

Wang, P., Sun, B., & Gu, B. (2012). Comparison of stab behaviors of uncoated and coated woven fabrics from experimental and finite element analyses. Textile Research Journal, 82(13), 1337-1354.

Wang, X., Georganas, N. D., & Petriu, E. M. (2009, November). Fiber-level structure recognition of woven textile. In 2009 IEEE International Workshop on Haptic Audio visual Environments and Games (pp. 117-122). IEEE.

Wang, Y., Li, J., & Zhao, D. (1995). Mechanical properties of fiber glass and kevlar woven fabric reinforced composites. Composites Engineering, 5(9), 1159-1175.

Watn, A., & Chew, S. H. (2002, September). Geosynthetic damage-from laboratory to field. In GEOSYNTHETICS: STATE OF THE ART-RECENT DEVELOPMENTS. PROCEEDINGS OF THE SEVENTH INTERNATIONAL CONFERENCE ON GEOSYNTHETICS, 7-ICG, HELD 22-27 SEPTEMBER 2002, NICE, FRANCE. VOLUME 4.

Wu, Tien H., William P. McKinnell III, and Douglas N. Swanston. "Strength of tree roots and landslides on Prince of Wales Island, Alaska." Canadian Geotechnical Journal 16.1 (1979): 19-33.

Yahya, M. F., Ghani, S. A., & Salleh, J. (2014). Effect of impactor shapes and yarn frictional effects on plain woven fabric puncture simulation. Textile Research Journal, 84(10), 1095-1105.

Yahya, M. F., Salleh, J., Ahmad, W. Y. W., & Ghani, S. A. (2012, December). Finite element analysis of impactor shapes effects on puncture damage of plain woven fabric. In 2012 IEEE Colloquium on Humanities, Science and Engineering (CHUSER) (pp. 729-734). IEEE.

Yahya, M. F., Salleh, J., & Ahmad, W. Y. W. (2011, September). Uniaxial failure resistance of square-isotropic 3D woven fabric modelled with finite element analysis. In 2011 IEEE Symposium on Business, Engineering and Industrial Applications (ISBEIA) (pp. 16-21). IEEE.

Ye, Jingxue, Qi, Y., Wang, D., and Sun G., “Study on Seed Germination Features of Taraxacum mongolicum”, Northern Horticulture, no.5 (2013): 30~32.

Yokozeki, Tomohiro, et al. "Mechanical properties of corrugated composites for candidate materials of flexible wing structures." Composites Part A: applied science and manufacturing 37.10 (2006): 1578-1586.

Zako, M., Uetsuji, Y., & Kurashiki, T. (2003). Finite element analysis of damaged woven fabric composite materials. Composites Science and Technology, 63(3-4), 507-516.

Zhang, Chaobo, Xia Zhou, Jing Jiang, Yang Wei, Juanjuan Ma, and Paul D. Hallett. "Root moisture content influence on root tensile tests of herbaceous plants." Catena 172 (2019): 140-147.

Zhang, Chaobo, Dongrong Li, Jing Jiang, Xia Zhou, Xiaoyu Niu, Yang Wei, and Juanjuan Ma. "Evaluating the potential slope plants using new method for soil reinforcement program." CATENA 180 (2019): 346-354.

Zhang, C.-B., et al. (2014). "Why fine tree roots are stronger than thicker roots: The role of cellulose and lignin in relation to slope stability." Geomorphology 206: 196-202.

Zhang, Yingying, et al. "Anisotropic mechanical properties and constitutive relations of PTFE coated glass fibers." Composite Structures 179 (2017): 601-616.

Zheng, J., Takatera, M., Inui, S., & Shimizu, Y. (2008). Measuring technology of the anisotropic tensile properties of woven fabrics. Textile Research Journal, 78(12), 1116-1123.

Zhong, Chun-xin, Zhang, Wei, and Wang, Shu-ren. "Experimental research on soil erosion of turf slope reinforced by 3D vegetation net." Journal of Hohai University (Natural Sciences) 3 (2007): 4.

Zhou, H., Xiao, X., Qian, K., & Ma, Q. (2020). Numerical simulation and experimental study of the bursting performance of triaxial woven fabric and its reinforced rubber composites. Textile Research Journal, 90(5-6), 561-571.

Zhou, Z. C., and Z. P. Shangguan. (2005). Soil anti-scouribility enhanced by plant roots. Journal of Integrative Plant Biology, 47(6), 676-682.

Zhu, D., Mobasher, B., & Rajan, S. D. (2011). Dynamic tensile testing of Kevlar 49 fabrics. Journal of materials in civil engineering, 23(3), 230-239.

Zouari, Rym, Sami Ben Amar, and Abdelwaheb Dogui. "Experimental Characterization of Anisotropic Mechanical Properties of Textile Woven Fabric." International Journal of Materials and Textile Engineering 10.2 (2016): 409-415.